Enhancing Data Extraction from Localized Surface Plasmon Resonance Biosensors

Ahmed Abumazwed

Department of Electrical and Computer Engineering

McGill University

Montreal, Québec, Canada

April 2017

A thesis submitted to McGill University in partial fulfillment of the requirements of the degree of Doctor of Philosophy

Abstract

Localized Surface Plasmon Resonance (LSPR) sensors have attracted substantial interest in various applications due to their plasmonic properties, low cost instrumentation, and small sample requirement. LSPR is a photon–driven oscillation of the conduction electrons in metallic nanostructures. It features a short electromagnetic (EM) decay length, increasing the specificity to the bound analytes and reducing artefacts due to the variations in bulk refractive index (RI). However, the short EM decay length degrades the signal to noise ratio (SNR) of LSPR sensors, thereby reducing the accuracy of the results. To improve the SNR and accuracy of LSPR sensors, this thesis introduces new signal processing methods, including the projection method, the linear maximum likelihood estimation (linear–MLE) and the nonlinear–MLE method. These methods are validated numerically and applied to label free sensing experiments.

A numerical study is undertaken in the first part of the thesis to investigate the plasmonic properties of various nanostructures. The cost–effective side–wall lithography method is adopted here to fabricate the nanostructures, yielding reproducible resonance curves with negligible deviations in their resonance wavelengths (2–5 %). The projection method is shown to improve the SNR for nanostructures with broad resonance curves. It provides a direct measurement of the refractive index, and improves the SNR by a factor of 10 when compared to the dip-finding method. Compared to other advanced signal processing methods, the projection method achieves the best combination of SNR and limit of detection.

The linear–MLE method is proposed to improve the established linear response model

used in self–referenced sensors. Based on streptavidin-biotin binding experiments, the linear–MLE method improves the accuracy and precision by a factor of 4 when compared to the linear response model. This method can serve as a powerful means to distinguish surface binding events from the bulk RI change.

Finally, the thesis presents the nonlinear–MLE method. This method employs the MLE technique alongside a nonlinear response model to obtain accurate quantitative results of binding events. Compared to the established linear response model, the nonlinear–MLE method improves the precision of the estimated adlayer thickness and bulk RI change by factors of 5 and 36, respectively.

Abrégé

Les capteurs à résonance plasmonique de surface localisée (LSPR) ont suscité un intérêt important pour diverses applications en raison de leurs propriétés plasmoniques, de leur instrumentation à faible coût et de leur besoin minime en volume d'échantillon. Le LSPR est une oscillation par impulsion photonique des électrons de conduction dans les nanostructures métalliques. Il comporte une courte longueur de décroissance électromagnétique, augmentant la spécificité aux analytes liés et réduisant les artéfacts en raison des variations de l'indice de réfraction du tampon. Cependant, la courte longueur de décroissance électromagnétique dégrade le ratio du bruit sur le signal (SNR) des capteurs LSPR, réduisant ainsi la précision des résultats. Pour améliorer le SNR et l'exactitude des capteurs LSPR, cette thèse présente de nouvelles méthodes de traitement du signal, comprenant la méthode de projection, la méthode d'estimation linéaire de vraisemblance maximum (linéaire–MLE) et la méthode non-linéaire–MLE. Ces méthodes sont validées numériquement et appliquées aux expériences de détection sans étiquettes.

Une étude numérique est entreprise dans la première partie de la thèse pour enquêter les propriétés plasmoniques de diverses nanostructures. La méthode de lithographie à paroi latérale rentable est adoptée ici pour fabriquer les nanostructures, ce qui donne des courbes de résonance reproductibles avec des écarts négligeables dans leurs longueurs d'onde de résonance (de 2 à 5 %). Il est démontré que la méthode de projection offre une mesure directe de l'indice de réfraction, et améliore le SNR d'un facteur de 10 comparé à la méthode de détection de minimum. Par rapport à d'autres méthodes de traitement de signaux avancées,

la méthode de projection atteint la meilleure combinaison de SNR et de limite de détection.

La méthode linéaire–MLE est proposée pour améliorer le modèle de réponse linéaire utilisé pour les capteurs d'autoréférence. Sur la base des expériences de liaison streptavidine-biotine, la méthode linéaire–MLE améliore l'exactitude et la précision d'un facteur de 4 lorsque comparé au modèle de réponse linéaire. La méthode peut servir d'un moyen puissant pour distinguer les événements de liaison de variations dues à l'indice de réfraction de la solution tampon.

Finalement, la thèse présente la méthode non-linéaire–MLE. Cette méthode utilise le technique MLE avec un modèle de réponse non-linéaire pour obtenir des résultats quantitatifs précis des événements de liaison. Par rapport au modèle de réponse linéaire établi , la méthode non-linéaire–MLE améliore la précision des estimations de l'épaisseur de la couche d'adsorbat d'un facteur de 5 et l'indice de réfraction de la solution tampon d'un facteur de 36.

Acknowledgements

I would like to thank my supervisor, Prof. Andrew G. Kirk, whose guidance, advice and encouraging have always been motivating me towards the completion of this thesis. I thank him for accepting me to work under his supervision and to discover the exquisite field of plasmonics and its application in biosensing. I appreciate his unceasing support that allowed me to attend many workshops and international conferences and to work in one of the leading research centers in Japan, the physical and chemical research institute (RIKEN).

I sincerely thank the members of my PhD. supervisory committee for the helpful advice and discussions. I thank Prof. Maryam Tabrizian for discussing biochemistry protocols and the nonspecific binding; and Prof. Bruce Lennox for discussing the electromagnetic field associated with nanoparticles, and providing access to the spectroscopy facility. I thank Prof. Thomas Szkopek, for his suggestions regarding the calculation of optical cross sections of metallic nanostructures.

I am grateful to Prof. Takuo Tanaka of RIKEN institute, and Prof. Wakana Kubo of Tokyo University of Agriculture and Technology, for their help and support during and after my visit to RIKEN. I thank Makoto Daigo for the support in the nanoimprint lithography fabrication method. I also thank Yaeko Yazaki, Ryoko, Atsushi, Katsususke Shimazaki, Shin Yaginuma, Sho Ikeda, and all the people I met at RIKEN who made my research experience memorable.

I would like to thank the McGill Nanotool staff who provided the required training to work on a diverse processes at the clean room: I am grateful to John, Lino and Sasa. I would

also like to thank Marie-Hélène, at Ecole Polytechnique de Montreal, for providing me with training sessions on electron beam lithography, and for facilitating access to the clean room.

Thank you Sandrine Filion Côté and Mohamed Najih for discussing the projection method, and helping with the French translation of the thesis abstract. To Minh Tran, Chen Shen and Margaret Burns, thank you for the great time we had working together on LSPR sensing and the arduino micro-controller during your undergraduate projects. I thank all my former and present colleagues at McGill: Amin, Amir, Andra, Graham, Imran, Matt, Mehrnoosh, Phil, Rania, Roy, Samira, Sara, Songzhe, and Venkat.

I would like to thank Professor David Juncker for discussing the integration of microfluidic channels with LSPR sensing bio-chips, and providing access to the fabrication facilities. I sincerely thank Ayo Olanrewaju for the help with the PDMS replica moulding method. I also thank Pammy, Grant, Milad and Phillipe for their help.

I also acknowledge CMC Microsystems for the provision of COMSOL Multiphysics and OptiFDTD design tools.

My deepest gratitude goes to my mother and my wife for their prayers and support throughout my PhD. studies.

Dedicated to the memory of my father,
to my mother, my wife and children
Ahmed Abumazwed

April 2017

Contents

List of Figures

List of Tables

Abbreviations

AFM Atomic Force Microscopy

COC Cyclic Olefin Copolymer

COP Cyclic Olefin Polymer

DDA Discrete Dipole Approximation

DI Deionized

EM Electromagnetic

EOT Extra-ordinary Transmission

FDTD Finite Difference Time Domain

FEM Finite Element Method

FoM Figure of Merit

FWHM Full Width at Half Maximum

GNRMP Gold Nanorod Molecular Probe

ITO Indium Tin Oxide

L-Mode Longitudinal Mode

LM Linear response Model

LoD Limit of Detection

LoQ Limit of Quantification or Quantitation

LSPR Localized surface plasmon Resonance

MLE Maximum Likelihood Estimation

NA Numerical Aperture

NDIR Normalized Difference Integrated Response

NIR Near Infrared

NSOM Near field Scanning Optical Microscope

OT Optical Theorem

PDF Probability Density Function

PDMS Polydimethylsilane

PML Perfect Matched Layer

RI Refractive Index

RIU Refractive Index Unit

SEM Scanning Electron Microscopy

SERS Surface-Enhanced Raman Scattering

SPR Surface Plasmon Resonance

SPRI Surface Plasmon Resonance Imaging

T-Mode Transverse Mode

TE Transverse Electric

TM Transverse Magnetic

TUC Target Unit Cell

UV Ultra-violet

VSWFs vector spherical wave functions

1

Introduction

1.1 Problem statement

Over the past three decades, researchers have developed many classes of sensors for different applications such as medical diagnosis, drug detection, and environmental monitoring. These biosensors can be classified into electrical impedance sensors , electrochemical sensors and optical sensors [1]. Optical sensors have several advantages including their high sensitivity and immunity to the electromagnetic interference. Optical biosensors also span a wide range of platforms including surface plasmon resonance (SPR), interferometers, and ring resonators [2]. SPR biosensors exploit the phenomenon of the osillation of conduction electrons at metal-dielectric interface when their momentum matches that of an incident polarized wave [3]. To meet this condition, SPR platforms require complex instrumentation, using diffractive optical elements (including prism and grating coupling techniques) If the lateral dimensions of the

metallic film are decreased to a sub-wavelength scale, the phenomenon of localized surface plasmon resonance is observed, and it can be excited without diffractive optical elements [4, 5]. Metal nanostructures support this LSPR mode, as the conduction electrons can be coherently excited by a normal incident plane wave. The simple excitation approach used in LSPR sensors has overcome the vibration and mechanical noise incurred in conventional SPR sensors based on scanning elements. Moreover, the electromagnetic field is localized close to the surface of nanoparticles, and the resonance is perturbed mostly by the change in refractive index (RI) close to the metal surface due to the short electromagnetic (EM) decay length. This implies that LSPR sensors are more sensitive to molecular binding than to changes in the refractive index of the buffer solution, mitigating artifacts due to bulk RI changes and temperature drift [6]. Conventional SPR sensors require at least $10\mu m \times 10\mu m$ surface area for sensing [7,8], whilst a single nanoparticle footprint can be achieved based on LSPR sensors [9, 10]. Although LSPR sensors feature a lower bulk RI sensitivity than that for SPR sensors, they provide similar surface sensitivity [11]. Due to the short EM decay length, metallic nanostructures are limited to small biological samples. However, the EM decay length can be increased by exciting other modes, such as the guided mode based on parallel nanorods excied by the Kretchman configuration, which achieved an improved limit of detection when compared to conventional SPR sensor (300 nM vs 30 μM) [12]. These characteristics have attracted a great interest in nanoparticles to detect small analytes (less than 500 Da), which is challenging in conventional SPR platforms [13]. In addition, the miniaturized dimension of the LSPR sensors makes them good candidates for point of care applications, as they can be easily integrated with other bio–nanotechnology applications [14, 15].

The low SNR of LSPR sensors has motivated tremendous effort towards improving the sensitivity of LSPR sensors. Engineering the shape of metallic nanostructures has occupied a considerable attention, including nanospheres and nanorods [16–23], nanodisks [24, 25], and nanoshells [26–30]. Less attention has been previously paid to the signal processing methods to improve the SNR and fully benefit from the plasmonic properties of metallic nanostructures.

This thesis is focused on signal processing methods to improve the signal to noise ratio of LSPR sensors. Moreover, the thesis provides an accurate method to extract quantitative information from the measured data, including the adlayer thickness and bulk refractive index change. The thesis also presents an improved method in self-referenced LSPR sensing.

1.2 Objectives and Contributions

The following describe the main objectives of this thesis:

- To improve signal to noise ratio (improved RI resolution and limit of detection) for LSPR sensors.
- To improve self-referenced LSPR sensing, and distinguish between the binding events and bulk RI changes in both bulk and surface binding sensing experiments.
- To estimate the adlayer thickness and bulk RI changes in molecular binding experiments.

Following are the main contributions to achieve the above objectives

- SNR improvement: including the following:
  - A simple and accurate method (the projection method) is developed to improve the signal to noise ratio, and hence improve the limit of detection of LSPR biosensors with broad resonance curve. The method is validated by FDTD simulated results and compared to established signal processing methods based on simulated and measured results.
- Improving the accuracy for self-referenced sensing, employing the following:
  - Developing a method to correct for the sensitivity matrix, used by the linear response model (LM), based on true values for the experimental bulk RI and adlayer thickness sensitivities.
  - Using multiple-resonance nanorod structures and applying the maximum likelihood estimation to improve accuracy and precision of the results.

- Extract the adlayer thickness and bulk RI changes: including the following
  - The maximum likelihood estimation method (MLE) and a nonlinear response model–for the refractive index profile along the nanostructures – is used to provide an accurate estimation to the adlayer and RI changes in surface binding sensing experiments.
  - The method was validated by employing the FEM and applied to experimental data. Gold nanocrescent structures were fabricated by the side-wall lithography and used as a LSPR sensor. Each resonance is considered in the bulk refractive index and surface binding experiments.

The following publications are related to the above objectives and contributions

- A. Abumazwed, W. Kubo, C. Shen, T. Tanaka, and A. G. Kirk, "Projection method for improving signal to noise ratio of localized surface plasmon resonance biosensors," Biomed. Opt. Express 8, 446-459 (2016).
- A. Abumazwed, W. Kubo, T. Tanaka, and A. G. Kirk, "Towards accurate LSPR biosensors based on the projection method: a direct measurement for refractive index," accepted for oral presentation, Photonics north (June 2017).
- A. Abumazwed, W. Kubo, T. Tanaka, and A. G. Kirk, "Improved self-referenced biosensing with emphasis on multiple-resonance nanorod sensors," submitted to Opt. Express (2016).
- A. Abumazwed, W. Kubo, T. Tanaka, and A. G. Kirk, "Combination of the Maximum likelihood estimation and nonlinear model for improved accuracy and precision of estimating adlayer thickness and bulk RI change," To be submitted to scientific reports (2017).
- A. Abumazwed, W. Kubo, T. Tanaka, A. G. Kirk, Numerical and experimental investigation of plasmonic properties of silver nanocrescent structures for sensing applications," Proc. SPIE, 9371, 937127–937127–7 (2015).

- A. Abumazwed and A. G. Kirk, "Plasmonic properties of suspended nanodisc structures for enhancement of the electric field distributions," Proc. SPIE, 9288, 92880Z–92880Z–7 (September 2014).

- A. Abumazwed, W. Kubo, T. Tanaka, A. G. Kirk, "Study and measurement of plasmonic properties of gold double nanotube structure arrayed on a polymer substrate, " Proc. IEEE Photonics Conference, 318–319 (2013).

- A. Abumazwed, W. Kubo, T. Tanaka, A. G. Kirk, "Simulation and experimental studies on plasmonic properties associated with gold nanofin array on a polymer film, " Proc. IEEE Photonics Conference, 324–325 (2013).

- A. Abumazwed and A. G. Kirk, "Study of Plasmonic Properties of Gold Nanoparticles of Different Shapes with emphasis on Gold Nanopyramids, " Proc. of SPIE, 8412, 84121D–84121D–7 (2012).

- A. Abumazwed, W. Kubo, T. Tanaka, A. G. Kirk, "Design and fabrication of plasmonic nanostructures for optical biosensing by nanoimprint lithography," Photonics north, Montreal, May 2014 (Invited presentation).

1.3 Collaboration and author contributions

The fabrication of metallic nanostructures was a result of a collaborative work with Professor Takauo Tanaka and Dr. Wakana Kubo, RIKEN (Institute for physical and chemical research), Japan. Following describe the aspects of this collaboration:

- Dr. Kubo provided the nanocrescent and multiple-resonance nanorod structures.

- Professor Tanaka supervised me during my work at RIKEN.

- Professor Tanaka and Dr. Kubo helped in editing the published and submitted conference and journal papers.

I have done the following, under the supervision of the thesis advisor, Prof. Andrew Kirk

- Modeling the nanostructures using COMSOL multiphysics, OptiFDTD, and validation of the results with Mie theory.
- The fabrication of single and double nanotube structures at RIKEN, Japan.
- Spectroscopy measurements including the biosensing experiments at McGill. Chen Shen helped with sensing experiments for the nanotube structures.
- Near field and surface characterization of the fabricated samples at McGill.
- The fabrication of the Polydimethylsiloxane (PDMS) fluidic channels at McGill.
- The single projection method including reference matrix generation using FDTD calculations, and its application to simulated and measured data.
- Developing a method based on the MLE and the nonlinear response model for LSPR sensor response, to estimate the adlayer and bulk RI change in surface binding experiments.
- Developing a self–referencing method based on the maximum likelihood estimation and generalized linear response model.
- Data analysis and paper writing.

1.4 Thesis organization

The remainder of the thesis is structured as follows:

Chapter 2: reviews background material and published work, related to the proposed methods in this dissertation. Theoretical and practical challenges of LSPR sensors and available data processing methods (mostly established for conventional SPR platform) are also highlighted in this chapter.

Chapter 3: presents numerical and experimental studies for metallic nanostructures that will be used in the forthcoming chapters. The simulated results are based on the finite difference time domain and finite element methods. The chapter also undertakes surface characterization of the nanostructures fabricated by the nanoimprint lithography

technique. As well, the chapter investigates the reproducibility of the measured extinction curves and resonance wavelength. Surface characterization of the fabricated structures, using scanning electron microscopy (SEM) and atomic force microscopy (AFM), and their near field distribution is investigated by near field scanning microscopy (NSOM).

Chapter 4: stresses the projection method and its application in improving the signal to noise ratio of noisy LSPR transmission curves. The method is validated numerically by the FDTD simulation, and compared to the most established signal processing methods. The proposed method is then applied to bulk and surface-binding (Streptavidin-Biotin) sensing experiments. Moreover, this chapter provides a method for fitting the Cauchy parameters for ethanol and DI water to obtain values for the mixture and use them along with the improved Cauchy formula to determine the refractive indices for mixtures of different ethanol concentrations. The measured results are then validated based on the fitted RI values.

Chapter 5: investigates the application of the MLE method to improve self-referencing LSPR sensors. The chapter employs the three-resonance characteristic of gold nanorods in estimating adlayer and bulk RI change. The method is compared to an established method based on the same simulated and measured data. The chapter provides a solution to the previously introduced approach which required repetitive simulation in order to generate the sensitivity matrix for the linear response model. The proposed method considers the measured sensing parameters rather than the simulated counterparts. This method provides a direct measure for adlayer thickness and bulk RI changes. Each resonance is used with the other resonances to estimate the adlayer and bulk RI change, obtaining three estimates for the adlayer thickness and bulk RI change. The maximum likelihood estimation is finally applied to the values estimated based on the three LM systems, maximizing the likelihood of obtaining accurate estimates.

Chapter 6: presents an accurate method for estimating the adlayer thickness and RI change based on the MLE and the nonlinear response model (the sensor response vs adlayer thickness). This chapter employs the multiple resonance characteristic, associated with the nanocrescent structures. The nanoimmprint lithography was used to fabricate the structures. The chapter underlines the theoretical details, the validation of the method, and a

comparison to the established linear response model.

Chapter 7: concludes the thesis by a general discussion and provides recommendations for future research directions.

2

Theoretical background and concepts

This chapter reviews conceptual background related to Localized Surface Plasmon Resonance (LSPR) sensors and metallic nanostructures. The chapter also presents a brief description of propagating Surface Plasmon Resonance (SPR) sensors, stressing the motivation for the adoption of metallic nanostructures as an alternative solution in some applications.

2.1 Comparison between propagating and localized surface plasmon resonances

Surface plasmon resonance is an optical phenomenon that occurs at a metal-dielectric interface where the metal free electrons oscillate with respect to an incident electromagnetic (EM) wave whose momentum matches that of the free electrons. Exciting the propagating SPR mode– for various SPR configurations– requires optical components to match the momentum of the incident wave to that associated with the plasmon wave, such as optical

waveguides [31], grating couplers [32], and prism coupling [33]. Prim coupling is commonly used with numerous sensing platforms, including SPR imaging (SPRI), angular or wavelength sensing platforms. Kretschmann [34] and Otto [35] configurations have been previously proposed as prism coupling for SPR sensors. Fig. 2–1 illustrates the Kretschmann configuration as the evanescent wave penetrates the biological layer and change in the refractive index of the ambient medium can be detected by measuring the reflectivity as shown in Fig. 2–1. The intensity of the reflected wave decreases as the angle of incidence approaches the resonance angle. When analytes interact with the binding ligands, the surface concentration increases, and the resonance angle increases. The refractive index sensitivity is defined as the shift in these measured quantitities (angle, wavelength, intensity) with respect to the change in refractive index. The evanescent wave propagates about 500 nm away from the metal surface and a few microns along the metal surface, providing a RI sensitivity of $100 - 300^{\circ} RIU^{-1}$ and $5500 - 7500\, nm\, RIU^{-1}$ for the angular and spectral SPR platforms, respectively [36,37].

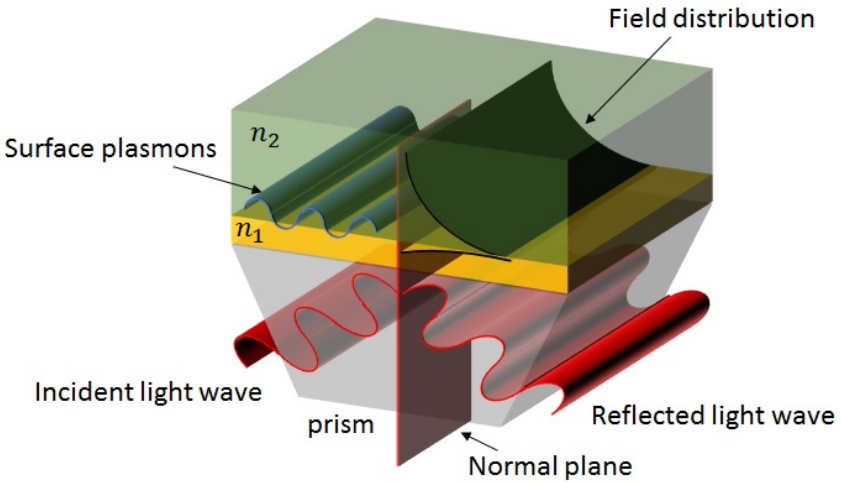

Figure 2–1: SPR biosensor layout, based on the Kretschmann configuration, illustrating the surface plasmon propagation along the surface, and the evanescent wave penetration into the ambient medium. The evanescent field has its maximum at the metal surface and decays exponentially into the ambient medium (biological layer).

In contrast to the situation in propagating SPR, when a light wave impinges a metal nanoparticle, it can excite its conduction electrons without prism or grating coupling, as shown in Fig. 2–2. Consequently, light is either scattered or absorbed by the metal nanopar-

ticle when the wavelength of the incident light wave matches the resonance wavelength of the metal nanoparticle. Table 2.1 compares the characteristics of SPR and LSPR as biosensors.

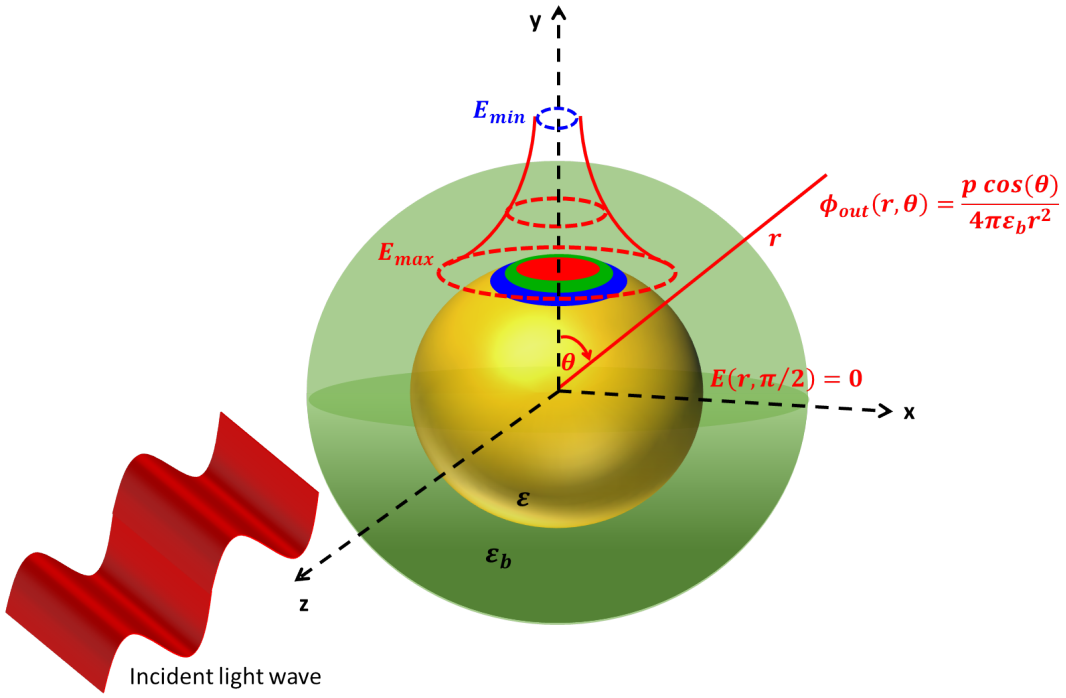

Figure 2–2: Schematic for a typical LSPR sensor based on a metal nanoparticle with dielectric permittivity ε, surrounded by a medium of a relative permittivity ε_b. LSPR mode can be excited with an unpolarized wave with an arbitrary incidence angle, but a polarized wave is considered here to illustrate the local EM field profile. The maximum electric field is induced at ($\theta = 0$), decaying along the particle surface, and approaching zero as $\theta = \pi/2$. The electric field also decays away from the surface of the nanoparticle into the ambient medium. The dipole potential $\mathbf{\Phi_{out}}$ due to dipole $\mathbf{p}$ at a distant point (r, θ) is also demonstrated.

Table 2.1: Comparison between LSPR and propagating SPR characteristics (Adapted from [6] with modification).

	SPR	LSPR
Label-free detection	Yes	Yes
Bulk sensitivity ($nm\,RIU^{-1}$)	$\approx 10^6$	$\approx 10^2$
Probe depth (nm)	≈ 1000	$10-30$
Temperature control	Yes	No[a]
Chemical identification	SPR Raman	LSPR-SERS[b]
Spatial resolution	$10\mu m \times 10\mu m$	Single nanoparticle
Small molecule sensitivity	Good	Better
Nonspecific binding	Minimal	Minimal
Multiplex capabilities	Yes	Yes

[a] LSPR features a short EM decay length and short probe depth, making it immune to interfering effect from change in RI of the buffer due to changes in temperature.
[b] SERS: Surface-Enhanced Raman Scattering.

For a nanosphere of a small radius when compared to the wavelength of the incident light wave ($a \ll \lambda$), the incident field can be assumed to be uniform, E_0, the EM field inside and outside the particle can be derived from scaler potentials, $\mathbf{\Phi_{in}}(\mathbf{r},\theta)$ and $\mathbf{\Phi_{out}}(\mathbf{r},\theta)$ as follows

$$\mathbf{E_{in}} = -\nabla\mathbf{\Phi_{in}},\ \mathbf{E_{out}} = -\nabla\mathbf{\Phi_{out}}$$

where $\nabla^2\mathbf{\Phi_{in}} = 0$ for $(r < a)$, and $\nabla^2\mathbf{\Phi_{out}} = 0$ for $r > a$. At the sphere–medium interface (r=a), the potentials must satisfy the following

$$\Phi_{in} = \Phi_{out},\ \varepsilon\frac{\partial\Phi_{in}}{\partial r} = \varepsilon_b\frac{\partial\Phi_{out}}{\partial r}$$

where ε_b is the bulk (medium) relative permittivity, and ε is the particle dielectric permittivity $\varepsilon(\omega) = \varepsilon_r(\omega) + i\,\varepsilon_i(\omega)$.

As well, at a large distance (r$\rightarrow\infty$), the electric field is the same as the unperturbed applied field

$$\lim_{r\to\infty}\Phi_{out} = -E_0\,r\,cos\,\theta = -E_0\,z$$

.

The scaler potentials can be obtained by solving the Laplace equation based on the above conditions

$$\mathbf{\Phi_{in}} = -\frac{3\,\varepsilon_b}{\varepsilon + 2\varepsilon_b} E_0\, r\, cos\,\theta$$
$$\mathbf{\Phi_{out}} = -E_0\, r\, cos\,\theta + \frac{\varepsilon - \varepsilon_b}{\varepsilon + 2\,\varepsilon_b}\, E_0\, a^3\, \frac{cos\,\theta}{r^2}$$

Under the quasistatic condition, the nanosphere can be represented by a dipole of two point charges separated by the diameter of the sphere, as shown in Fig. 2–3 (b). The moment ($\boldsymbol{p}$), exerted by the incident EM field on these charges, depends on the polarizability ($\boldsymbol{\alpha}$) as follows

$$\mathbf{p} = \varepsilon_b\, \boldsymbol{\alpha}\, E_0 \tag{2.1}$$
$$\boldsymbol{\alpha} = 4\pi a^3 \frac{\varepsilon - \varepsilon_b}{\varepsilon + 2\varepsilon_b} \tag{2.2}$$

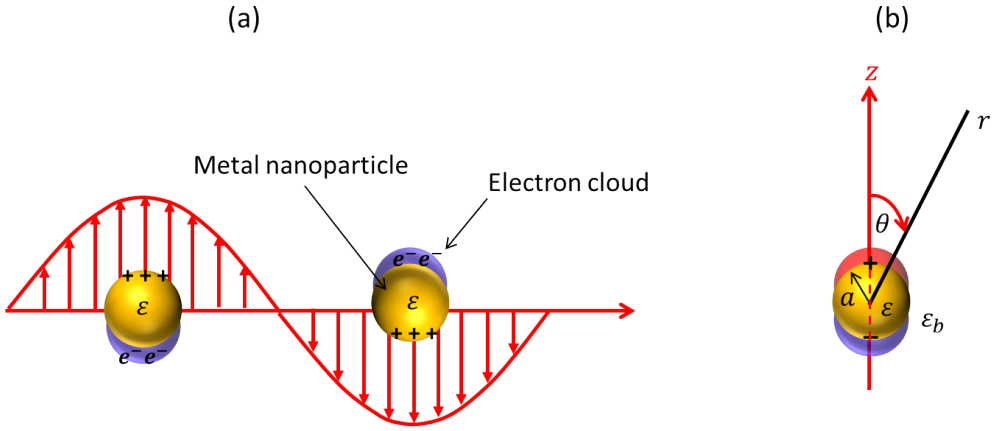

Figure 2–3: (a) Mechanism of LSPR, illustrating the oscillation of the electron cloud excited with a normal incident wave. (b) Equivalent electric dipole to a nanoparticle in a uniform static electric field.

The absorption and scattering cross sections are directly related to α as follows

$$\sigma_{ext} \approx \sigma_{abs} = k\, Im(\alpha) \tag{2.3}$$

$$\sigma_{scat} = \frac{k^4}{6\,\pi}|\alpha|^2 \tag{2.4}$$

where $k = 2\pi\sqrt{\varepsilon_b}/\lambda$ is the wave number outside the nanosphere. Eq. (2.4) represents Rayleigh scattering, as the scattering of light by nanospheres is inversely proportional to the fourth power of wavelength and increases with the square of the particle's volume. The absorption cross section contributes more than the scattering to the total extinction cross section, and it depends only on the volume of the nanoparticle. However, scattering becomes dominant for nanoparticles larger than 100 nm.

For nanoparticles of other shapes, the shape factor should be taken into account in calculatig the polarizability. For example, the surface of oblate or prolate spheroids is defined by $x^2/a^2 + y^2/b^2 + z^2/c^2 = 1$, where a, b, and c are the axes of the spheroid, and the polarizability α of the dipole associated with such particles is given by [38]

$$\alpha = \frac{4\pi a\,b\,c}{3}\frac{\varepsilon - \varepsilon_b}{\varepsilon_b + \rho\,(\varepsilon - \varepsilon_b)} \tag{2.5}$$

where ρ is the shape factor that can be calculated for for oblate spheroids ($a = b < c$) as follows [38]

$$\rho = \frac{g(e_c)}{2\,e_c^2}\left[\frac{\pi}{2}\,tan^{-1}g(e_c)\right] \tag{2.6}$$

$$g(e_c) = \left(\frac{1 - e_c^2}{e_c^2}\right)^{1/2},\ e_c^2 = 1 - \frac{c^2}{a^2} \tag{2.7}$$

where e_c is the eccentricity. For prolate spheroids ($a > b = c$), the shape factor is given by [38]

$$\rho = \frac{1 - e_c^2}{e_c^2}\left(\frac{1}{2\,e_c}\,ln\Big(\frac{1 + e_c}{1 - e_c}\Big) - 1\right), e_c^2 = 1 - \frac{b^2}{a^2} \tag{2.8}$$

Intuitively, the eccentricity e_c can be expressed in terms of the aspect ratio (AR) for nanorods (the ratio of major to minor axes) as $1 - AR^{-2}$, and by substituting in Eq. (2.8), the following equation is obtained for the shape factor for the nanorods

$$\rho = \frac{AR^{-2}}{1 - AR^{-2}} \left(\frac{1}{2\sqrt{1 - AR^{-2}}} ln\Big(\frac{1 + \sqrt{1 - AR^{-2}}}{1 - \sqrt{1 - AR^{-2}}} \Big) - 1 \right) \tag{2.9}$$

This is equivalent to the formula reported for the shape factor ρ with respect to the AR of the nanorods [39–41]

$$\rho = \frac{1}{AR^2 - 1} \left[\frac{AR}{2\sqrt{AR^2 - 1}} ln\Big(\frac{AR + \sqrt{AR^2 - 1}}{AR - \sqrt{AR^2 - 1}} \Big) - 1 \right] \tag{2.10}$$

which can be further simplified to $\rho \approx (1 + AR)^{-1.6}$ for $AR < 8$ [42]. For a spheroid, the shape factors along the principle axes satisfy $\rho_x + \rho_y + \rho_z = 1$, where the subscripts denote the x, y and z axes. This suggests a shape factor of $\sim 1/3$ for a sphere.

Eq. (2.5) can be employed to calculate the polarizability of nanorods along a specific axis (i=x, y or z) by considering their volume V as follows

$$\alpha_i = V \frac{\varepsilon - \varepsilon_b}{\varepsilon_b + \rho_i \left(\varepsilon - \varepsilon_b \right)} \tag{2.11}$$

This reduces to Eq. (2.2) for a nanosphere with a shape factor of 1/3. The average cross sections $\langle \sigma_{ext} \rangle$ and $\langle \sigma_{scat} \rangle$ for randomly oriented spheroids or nanorods (in the quasistatic regime) can also be determined as follows [38]

$$\langle \sigma_{ext} \rangle = k \, Im\{ \frac{1}{3}\alpha_x + \frac{1}{3}\alpha_y + \frac{1}{3}\alpha_z \}$$

$$\langle \sigma_{scat} \rangle = \frac{k^4}{6\,\pi} \{ \frac{1}{3}|\alpha_x|^2 + \frac{1}{3}|\alpha_y|^2 + \frac{1}{3}|\alpha_z|^2 \}$$

Now, assuming that the imaginary part of the dielectric function of a metal is small or its frequency dependence is negligible $\varepsilon_i(\omega) \approx 0$, the polarizability α has its maximum value when equating the denominator of Eq. (2.11) with zero, revealing the following

$$\varepsilon_r = \varepsilon_b \left(1 - 1/\rho \right) \tag{2.12}$$

Consequently, light interacts strongly with the nanoparticle, causing the conduction electrons to oscillate in resonance with the electric field of the incident light. This oscillation is

described as localized surface plasmon resonance. Some metals (gold, silver, copper) meet this condition at optical frequencies as the real part of their dielectric constant ε_r is negative. Their dielectric function can be expressed in terms of frequency ω by Drude free electron model as [38]

$$\varepsilon(\omega) = \varepsilon_\infty - \frac{\omega_p^2}{\omega^2 + j\gamma\omega} \tag{2.13}$$

where ε_∞ is the high frequency contribution to the dielectric function, $\gamma = v_F/l$ is the bulk electron collision frequency, or the bulk scattering rate, which is related to the Fermi level v_F and the electron mean free path l, ω_p is the metal plasma frequency given by [38]

$$\omega_p = \sqrt{\frac{N\,e^2}{\varepsilon_0\,m_e}} \tag{2.14}$$

where N is the electron density of the metal, ε_0 is the permittivity of vacuum, and m_e is the effective electron mass.

In light of the scattering rate, it has been hypothesized that the scattering is enhanced for small nanoparticles (relative to the electron mean free path l) [43], and the scattering rate becomes [43, 44]

$$\gamma_D = \gamma + A_{sc}\frac{v_F}{l'} \tag{2.15}$$

where l' is the reduced electron free path, which is related to the diameter of the spherical nanoparticles, and A_{sc} is an enhancement factor related to the particle surface scattering [45]

From equation (2.13) and neglecting the effect of γ in the visible region (i.e. $\gamma \ll \omega$)

$$\omega = \frac{\omega_p}{\sqrt{\varepsilon_\infty - \varepsilon}} \tag{2.16}$$

Now, if ε meets the resonance condition in Eq. (2.12), then $\varepsilon_i \approx 0$, $\varepsilon \approx \varepsilon_r = \varepsilon_b\,(1 - 1/\rho)$ and $\omega = \omega_r$. Substituting in Eq. (2.16), we obtain the resonance frequency ω_r as follows

$$\omega_r = \frac{\omega_p}{\sqrt{\varepsilon_\infty - \varepsilon_b(1 - \frac{1}{\rho})}} \tag{2.17}$$

The resonance wavelength can be obtained as follows

$$\lambda_r = \lambda_p \sqrt{\varepsilon_\infty - \varepsilon_b(1 - \frac{1}{\rho})} \tag{2.18}$$

This equation implies that the resonance is redshifted by increasing the ambient refractive index or reducing the shape factor (increasing AR). The application of an external electrostatic field can also decrease or increase the charge density, leading to redshift or blue shift of the resonance wavelength, respectively [46]. The dielectric function of metal has been electrochemically tuned, altering the charge density and surface damping. Indium Tin Oxide (ITO) substrates were employed as top and bottom electrodes with electrolyte for the capacitive electrochemical cell, and gold particles were immobilized on the bottom substrate (electrode). The top electrode was grounded and the bottom electrode was biased by a DC voltage source (swept from 0 to 2.25 V, and then -2.25 V to 0 V). This causes a redshift with the positive applied bias, and a blueshift and increased absorption with the negative applied bias [47]. Metallic nanorods support two principal plasmonic modes; transverse mode (T-Mode), due to light interaction along the short axis of the nanorod at the visible band (520 nm), and the longitudinal mode (L-Mode) which corresponds to light interaction of the long axis of a nanorod. The longitudinal mode can be tuned from visible to near infrared (NIR) region of the spectrum by controlling the aspect ratio of the nanorods. For a nanorod array on a substrate, both T-Mode and L-Mode LSPR can be excited, and a new guided mode is yielded, which has a strong and narrow resonance [12]. Therefore, the charge density and the resonance wavelength can be tuned by engineering the shape of metal nanostructures. This thesis will use nanostructures with different shapes to excite multiple resonances and exploits this characteristic in improving signal to noise ratio, quantitative analysis, and self-referencing for LSPR sensors. A thorough study for the dielectric properties of noble metals, emphasizing gold and silver, is presented below.

2.2 Permittivity of gold and silver

The dielectric properties for metal nanoparticles presented above considered the Drude model to determine their resonance wavelength. The model can also interpret the behaviour of noble metals in terms of their dielectric properties. Fig. 2–4 shows the characteristics of a metal interacting with a light wave of different frequencies. Some metals meet the plasmon condition at the visible and NIR range, because their plasma frequencies are located in the Ultra–violet (UV) band. However, gold and silver support sharper resonances than other metals such as Aluminum and Copper. Silver supports a sharper resonance than gold due to its lower electron collision frequency. This can be observed by comparing the imaginary part of gold and silver in [Fig. 2–5 (b) and (d)]. However, silver is not resistant to oxidation and may be toxic for some biological materials. The oxidation also alters the material properties of silver, degrading its plasmonic properties. Therefore, gold is the most practical metal used in biosensing due to its bio-compatibility and resistance to the oxidation effect.

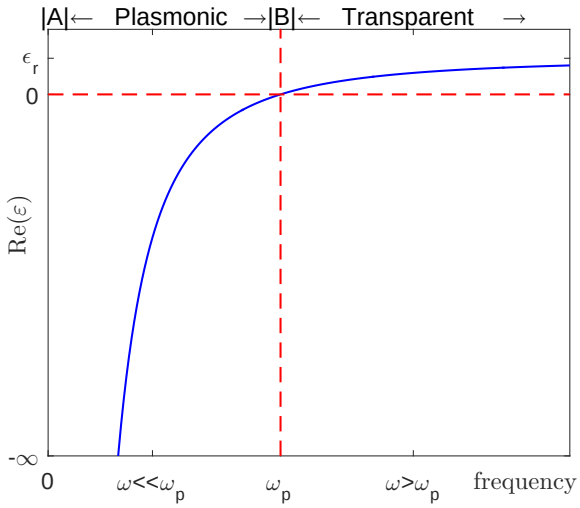

Figure 2–4: Behaviour of metal over a frequency range relative to plasma frequency. The point [A] represents a perfect conductor where the electric field cannot penetrate into the metal, and point [B] is where the frequency equals the plasma frequency and the E-field penetrates more in to the metal surface. The metal becomes plasmonic when $\omega << \omega_P$ and transparent for $\omega > \omega_p$.

Due to the fast response of the conduction electrons (the free electron or intraband transitions) compared to the frequency of an incident EM wave with a short wavelength

($\leqslant 600nm$), the EM wave cannot penetrate the metal ($\varepsilon_i \approx 0$) [49], and the Drude model can fit the experimental dielectric permittivity of gold as shown in Fig. 2–6. However, for shorter wavelngths ($\leqslant 600nm$), the EM wave can penetrate the metal due to the interband transitions, and the real part of the dielectric permittivity decreases and its imaginary part increases (accounting for the dissipated EM energy in the metal). In this case, the Drude model becomes inaccurate for fitting the experinetal dielectric permittivity for gold, because it does not take into account the interband transitions. Therefore, the dielectric function for gold deviates from the measured counterpart for wavelengths ($\leqslant 600nm$) as shown in Fig. 2–6. The multiple oscillator model (Drude-Lorentz model) was suggested to overcome the limitations of the Drude model by considering not only the intraband transitions, but also the interband transitions (bound electrons) [38]. This model adds one or several Lorentzian terms to Eq. (2.13). For simplicity, we use the improved dispersion law, based on the Drude Lorentz model, that was introduced to further improve fitting the permittivity of gold [50]. It was recommended to add only one Lorantzian term to the model to reduce the memory requirements (which increase linearly with the number of terms used in the dispersion model) [50]. Thereofore, the permittivity of gold can be expressed as follows [50]

$$\varepsilon(\omega) = \varepsilon_\infty - \frac{\omega_p^2}{\omega(\omega + i\gamma_D)} - \frac{\Delta_\varepsilon.\omega_L^2}{(\omega^2 - \omega_L^2) + i\gamma_L\,\omega} \tag{2.19}$$

where ω_L and Δ_ε are the strength and the spectral width of the Lorentz oscillators, respectively, and γ_L is a weighting factor. For gold, $\omega_L \sim 650$ THz, $\Delta_\varepsilon \sim 1.09$, and $\gamma_L \sim 104.86$ THz. Fig. 2–6 compares the Drude and Drude Lorentz models with the experimental values from Johnson and Christy [48]. The Drude Lorentz model based on a single lorentzian term provided an improved fit to the experimental values, but it did not correct for wavelengths below 420 nm. This can be improved by adding more lorentzian terms to account for more interband oscillations. Five Lorentzian terms were previously used to fit the permittivity of various metals for energies between 0.1 and 5 eV [51]. Adding more lorentzian terms can improve the precision, but it would also increase memory requirement for calculating permtivities. Nevertheless, the LSPR wavelength for gold nanostructures is located towards the red to NIR region, indicating that adding a single lorentzian term can be sufficient to model

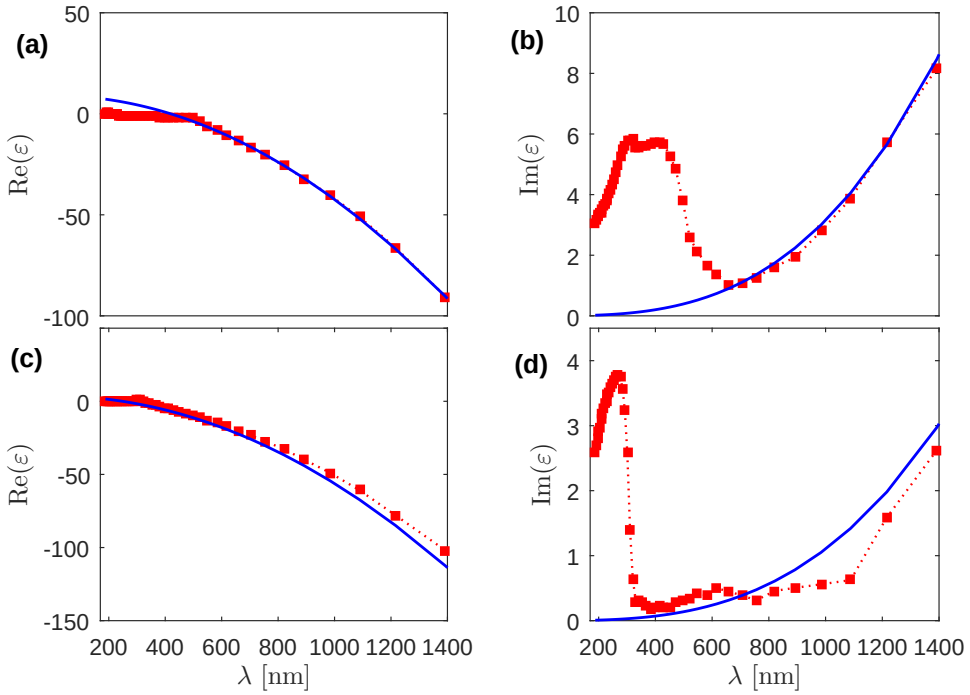

Figure 2–5: Real and imaginary part of the dielectric permittivity for (a,b) gold, and (c,d) silver. The blue line represents the calculated values using the Drude model, and the red line represents the measured data from Johnson and Christy [48]. The Drude model does not take into account the interband transition.

the permittivity. The FDTD results presented in this thesis are based on the Drude-Lorentz model, whereas the FEM considered the experimental values from Johnson and Christy [48].

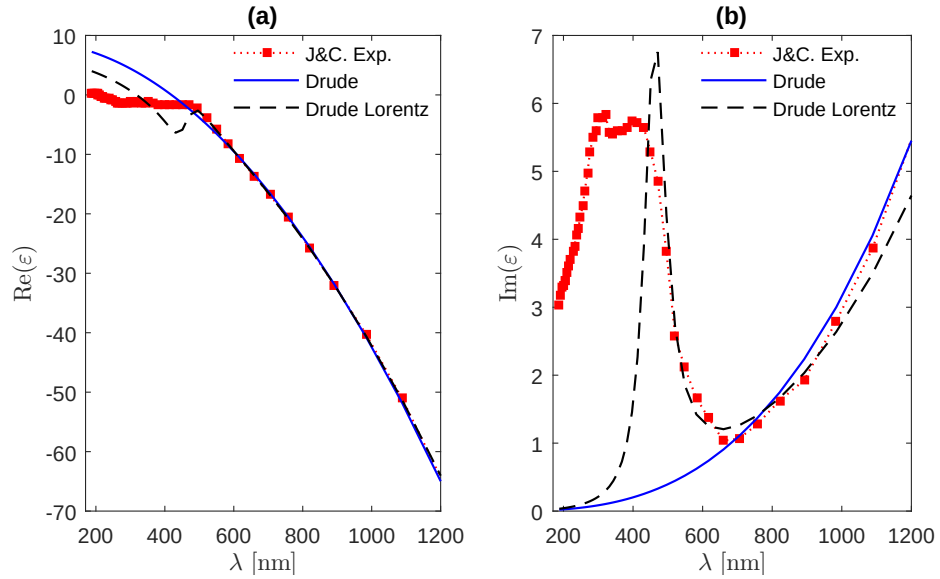

Figure 2–6: The corrected real and imaginary parts of the dielectric permittivity for gold, calculated using the Drude Lorentz model, and compared with the results obtained from the Drude model and the measured values by Johnson and Christy [48].

2.3 Methods for light scattering calculation

In order to study the optical properties of the fabricated nanostructures, a proper numerical method has to be used. This section presents a review of various analytical and computational techniques to model metal nanoparticles of various shapes.

2.3.1 Mie theory

In 1908, Gustav Mie solved Maxwell's equations for scattering of light by a homogeneous sphere [52]. The solution consists of a number of modes according to the size of the sphere relative to the wavelength [53]. Considering an incident plane wave on an isotropic spherical particle embedded in a nonabsorbing isotropic medium, Maxwell 's equations can be written as [54]

$$\nabla \times \mathbf{E}\,(r,t) = -\frac{\partial \mathbf{H}\,(r,t)}{\partial t} \tag{2.20}$$

$$\nabla \times \mathbf{H}\,(r,t) = \varepsilon(r)\,\frac{\partial\,\mathbf{E}\,(r,t)}{\partial\,t} \tag{2.21}$$

$$\nabla.\mathbf{E}\,(r,t) = 0 \tag{2.22}$$

$$\nabla.\mathbf{H}\,(r,t) = 0 \tag{2.23}$$

The time harmonic fields in an isotropic medium satisfy the wave (Helmholtz) equations

$$\nabla^2\,\mathbf{E} + k^2\,\mathbf{E} = 0 \tag{2.24}$$

$$\nabla^2\,\mathbf{H} + k^2\,\mathbf{H} = 0 \tag{2.25}$$

Where $k^2 = \omega^2\,\varepsilon\,\mu_0$. The scattered fields can be expanded in vector spherical harmonics because of the symmetry of the sphere. Therefore, the field vectors $\mathbf{E}$ and $\mathbf{H}$ can be replaced by M_L and N_L where the subscript, L, implies that the scattered field $\mathbf{E}_{sca}$ can be described by different spherical harmonics, L=1(dipole), 2(quadrapole).

$$E_{sca} = \sum_{L=1}^{\infty} E_L\,(i\,a_L\,N_{e1L} - b_L\,M_{o1L}) \tag{2.26}$$

$$H_{sca} = \frac{k}{\omega\,\mu}\sum_{L=1}^{\infty} E_L\,(i\,b_L\,N_{o1L} + a_L\,M_{e1L}) \tag{2.27}$$

$$E_L = i^n E_0\,\frac{2\,L+1}{L(L+1)} \tag{2.28}$$

where E_0 is the incident field, and N and M represent the first order Legendre and Bessel functions whereas the subscripts, o and e, represent the odd and even branches of the solution to the vector form of the Helmholtz equation. The relative amplitudes of the vector spherical harmonics of the scattered fields are determined by Mie coefficients, a_L and b_L that are given by

$$a_L = \frac{\bar{n}\psi_L(\bar{n}\,x)\psi'_L(x) - \psi_L(x)\,\psi'_L(\bar{n}x)}{\bar{n}\psi_L(\bar{n}\,x)\xi'_L(x) - \xi_L(x)\,\psi'_L(\bar{n}x)} \tag{2.29}$$

$$b_L = \frac{\psi_L(\bar{n}\,x)\psi'_L(x) - \bar{n}\,\psi_L(x)\,\psi'_L(\bar{n}x)}{\psi_L(\bar{n}\,x)\xi'_L(x) - \bar{n}\,\xi_L(x)\,\psi'_L(\bar{n}x)} \tag{2.30}$$

where $\bar{n} = n_p/n_B$, n_p and n_B are particle and medium refractive indices, respectively, $\mu = \mu_p/\mu_b$, $x = 2\pi n_p a/\lambda$, is the size parameter, a is the radius of the sphere, λ is the vaccum wavelength, and ψ_L and ξ_L are Riccati-Bessel functions of order L.

The coefficients a_L and b_L can be calculated by computer codes and the scattered fields can be calculated using equations (2.26) and (2.27). The scattering and extinction cross sections can also be calculated by

$$Q_{sca}^{(L)} = \frac{2}{x^2}(2L+1)(|a_L|^2 + |b_L|^2) \tag{2.31}$$

$$Q_{ext}^{(L)} = \frac{2}{x^2}(2L+1)Re(a_L + b_L) \tag{2.32}$$

2.3.2 Discrete Dipole Approximation (DDA)

Discrete dipole approximation is a volume integral equation method that is used to simulate light scattering by particles with sizes comparable with wavelength. DDA or the coupled dipole method was introduced by Purcell and Pennypacker in 1973 [55]. In this method, the particle is divided into a number of dipoles (d_N). A system of linear equations (N) can be written in N fields exciting the N dipoles and the solution is used to compute the total scattering. For particles of dimensions comparable to wavelength, the method requires 10 dipoles per wavelength inside the particle. This number increases with the refractive index of the particle (n_p), slowing down the convergence of the iterative solver. The validity criteria for the size of dipoles d_N becomes [56]

$$d_N = \frac{\lambda}{10|n_p|} \tag{2.33}$$

For smaller particles (compared to wavelength), the method requires at least 10 dipoles for the smallest dimension of the nanoparticle. The accuracy of the method is affected by increasing the refractive index rather than the dimension of the nanoparticle as long as the above criteria are met [56, 57]. The polarization of each dipole is affected by the incident plane wave and the electric fields induced by the other dipoles. The superposition of the fields of all dipoles is considered to be the far field. The method can be extended to deal with periodic structures of a target unit cell (TUC) consisting of a number of N polarizable points as shown in Fig. 2–7. Draine and Flatau developed a public program based on this

technique (DDSCAT 7.1) [58].

The DDA is applicable to arbitrary shape and orientations of particles. It can be applied in the case of inhomogeneous and anisotropic particles. In this case, it has a limited numerical accuracy. It converges slowly as the number of dipoles increase. Recalculation is required as the angle of incidence is changed.

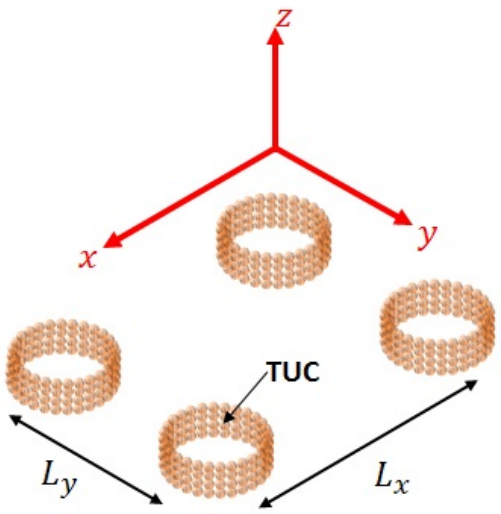

Figure 2–7: Modeling of periodic nanostructures by DDA

2.3.3 Finite Element (FEM) and Finite Difference Time Domain (FDTD) Methods

For nanostructures of complex shapes, the Mie theory and quasistatic approximation are not applicable. Alternatively, the solution of Helmholtz Maxwell equations is obtained by the Finite Element Method (FEM) or Finite difference Time Domain (FDTD) method.

The FEM is a differential equation method solving the vector Helmholtz equation where the scatterer and the domain are discritized into cells (elements) [59]. The values of unknown fields are specified at the elements' nodes and, by enforcing the boundary conditions, are solved by Gaussian elimination or conjugate gradient method. This technique is suitable to model arbitrary shaped and inhomogeneous particles. The main drawback of this method is that it is computationally expensive as the computations are spread over the entire discretized space (domain) not just the scatterer.

The FDTD method was first introduced by Yee [60]. It solves Maxwell's time varying curl equations. Space and time derivatives are approximated by a finite difference scheme (space and time discretizations). Particles are embedded in a computational domain and absorbing boundary conditions are forced to model the particle in open space. In the case of periodic structures, the periodic boundary conditions are enforced along the periodic planes. OptiFDTD is a commercial software that is based on this technique [61].

Other methods can be used for simple nanostructures. For example, the multiple multipole method is widely used in near field problems for spherical and axially symmetric particles [62]. The T-matrix method was introduced by Waterman in 1965 [63] for a single homogeneous particle. It was used to compute the scattering characteristics of arbitrary clusters of nonspherical particles by Peterson and Ström [64]. This method is based on the vector spherical wave functions (VSWFs) of the incident and scattered fields. The T-Matrix method depends on the particles size parameter, its shape, its refractive index, and on the particles orientation with respect to the coordinate system. Thus, the scattering by a rotated particle or orientation averaged scattering can be computed. The standard T-matrix method is restricted to particles with aspect ratio of about 1–4 [65].

Choosing a proper technique depends on the particle size, shape, the dielectric constant of the material, and if the particle is homogeneous or inhomogeneous. Since the FDTD and FEM are capable to model nanoparticles with arbitrary shapes without restrictions (such as DDA), these methods are adopted in this thesis to handle modeling the proposed metallic nanostructures. COMSOL multiphysics, based on the FEM, is used to study the plasmonic properties and the electromagnetic field distribution associated with the nanostructures [66]; and OptiFDTD, which is based on FDTD method [61], to calculate transmission curves (reference matrix) for the projection method. The results of both methods are first compared with those based on Mie calculations to validate the modeling accuracy, then the FDTD and FEM will be used in the forthcoming chapters.

2.4 Spectroscopy techniques for LSPR measurement

Unlike propagating SPR, simple methods can be used to excite the LSPR. The LSPR mode can be simply excited by illuminating the nanostructures with a light source, regardless of the incident angle. This does not require a complex instrumentation or scanning optics as those used with propagating SPR sensor. There are many platforms that are used in LSPR detection, including bright field microscopy, dark field microscopy and spectroscopy, and direct illumination of LSPR sensor, which is the simplest form. This section addresses these platforms in some detail.

2.4.1 Bright and Dark field Microscopy

Bright field microscopy provides a direct measurement of extinction (absorption and scattering) of nanostructures, as shown in Fig. 2–8 (a). It can probe an area that is orders of magnitude smaller than that probed in the spectrometer set-up. To reduce the effect of the scattered light from the substrate, an objective lens with low numerical aperture (NA) should be used. However, the unwanted scattered light may dominate if the density of the nanoparticles is extremely low (such as single particle detection). This can be improved by using a dark field microscope.

Dark field microscopy has been widely used in protein association [67]. The advantage of dark field microscopy is that it reduces the effect of background noise and it can measure the scattering from even a single nanoparticle. Intuitively, the absorption cross section dominates over the scattering cross section for small nanoparticles ($< 100nm$). Therefore, bright field microscopy is adopted instead of dark field microscopy for absorption measurements. Fig. 2–8 (b) demonstrates a basic dark field microscopy. A condenser lens shines a hollow light cone on the nanostructures, and only the scattered light is collected by the objective. The direct light rays are blocked by an opaque central screen. The NA of the dark field objective should be adequately high to collect enough photons. Oil immersion objectives can be used as they satisfy this condition (high NA). However, the NA of the objective should be smaller than that of the condenser to avoid collecting the direct light from the source (the light

cone). An aperture stop can also be used to reduce the working aperture in the case of high NA objectives. A recent study has reported advances of dark field microscopy in LSPR imaging [68].

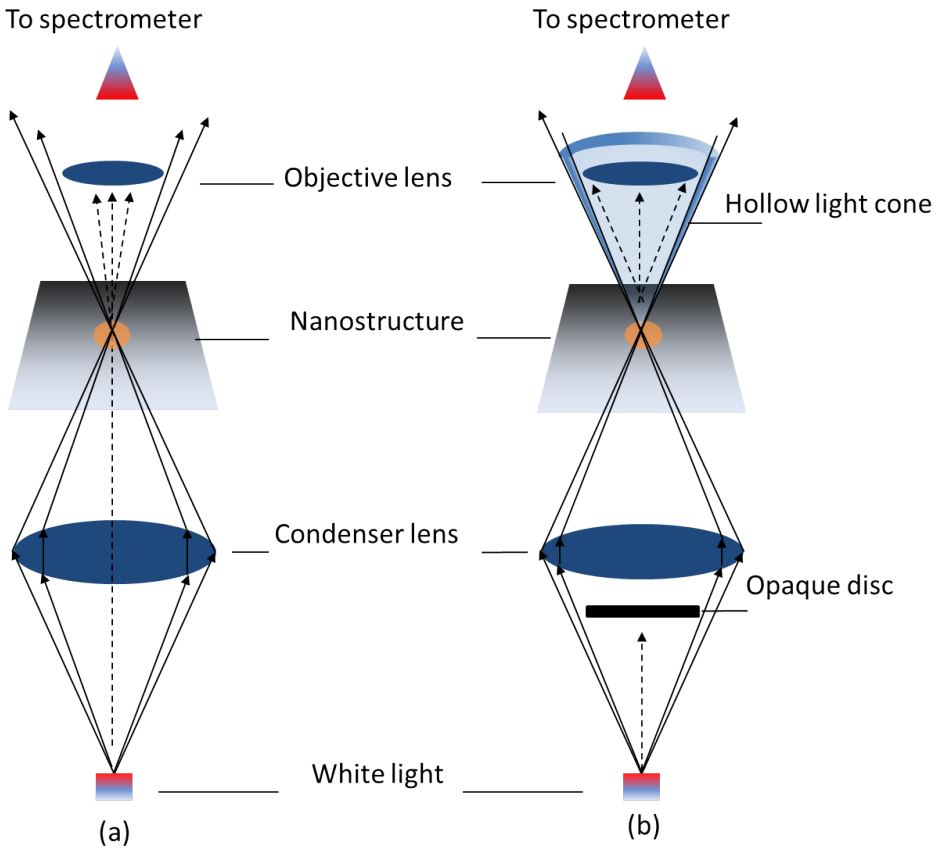

Figure 2–8: Schematic for Bright field (a) and Dark field (b) microscopy concepts.

2.4.2 Reflection measurement

Similar to dark field microscopy, measuring the reflection from the nanoparticles can be adopted when the scattering cross section dominates over the absorption cross section, and therefore contributes significantly to the total extinction efficiency of the nanoparticle. The reflection measurement can be performed by using a diffuse reflectance probe, where the central fiber optic carries the incident beam, and the scattered light is collected by fiber optics arranged around the circumference of the probe, and analyzed by a spectrometer, as shown in Fig. 2–9 (a). The reflection measurement can also employ an integration sphere, where the nanostructures are placed inside a reflecting sphere, facing the incident light beam, and the scattered light is collected through a probe placed at 90° from the main optical path to avoid collecting photons from the direct incident light. A schematic for this platform is shown in Fig. 2–9 (b).

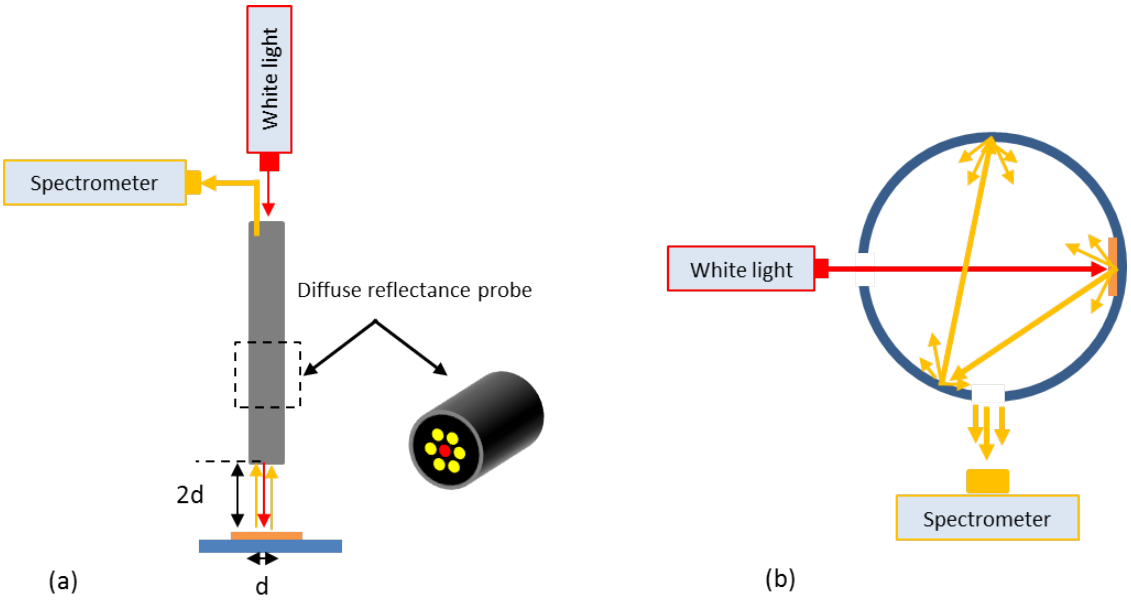

Figure 2–9: LSPR spectroscopy based on reflection measurements, employing (a) reflecting probe, and (b) integration sphere.

2.4.3 Direct transmission of light

This platform represents the simplest method to excite the LSPR mode, but it is impacted by noise. A schematic, illustrating this method, is shown in Fig. 2–10. The measured results presented in this thesis are based on this approach, as the nanostructures are directly excited by the light beam and the transmitted light is collected by a photodetector, within a monochromator-based spectrometer (Cary 5000 spectrometer). An aperture is used to limit the direct light from the source and hence reduce the noise.

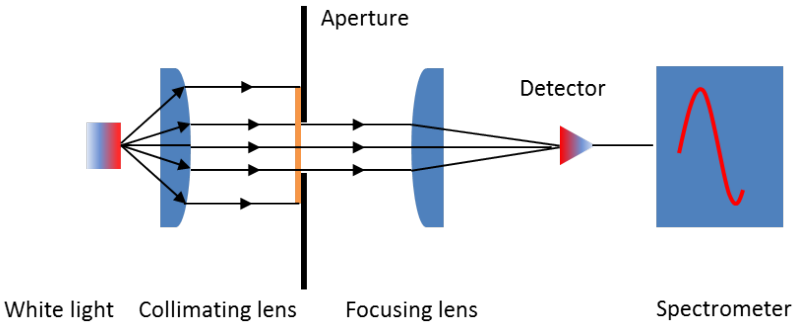

Figure 2–10: LSPR spectroscopy based on the direct measurement of transmitted light.

2.5 Sensor performance characteristics

This section defines sensor characteristics that are used in comparing different sensing platforms. These characteristics are related to the bulk RI sensitivity and adlayer sensitivity. As illustrated in Fig. 2–11 (a) the bulk RI sensitivity relates the sensor response to refractive index changes in the buffer, whilst the adlayer sensitivity is directly related to the adlayer thickness in surface binding experiments. The adlayer and bulk RI sensitivities are related to the EM decay length. Short EM decay length indicates a broad resonance curve and low bulk RI sensitivity due to the short sensing probe depth. However, the effect of EM decay length may be less pronounced in the case of sensitivity to adlayer thickness, especially for small analytes. Fig. 2–11 (b) illustrates this concept based on SPR and LSPR sensors. The EM decay length also affects other characteristics, such as the signal to noise ratio, RI resolution and limit of detection. The remainder of this section provides more details about

these characteristics.

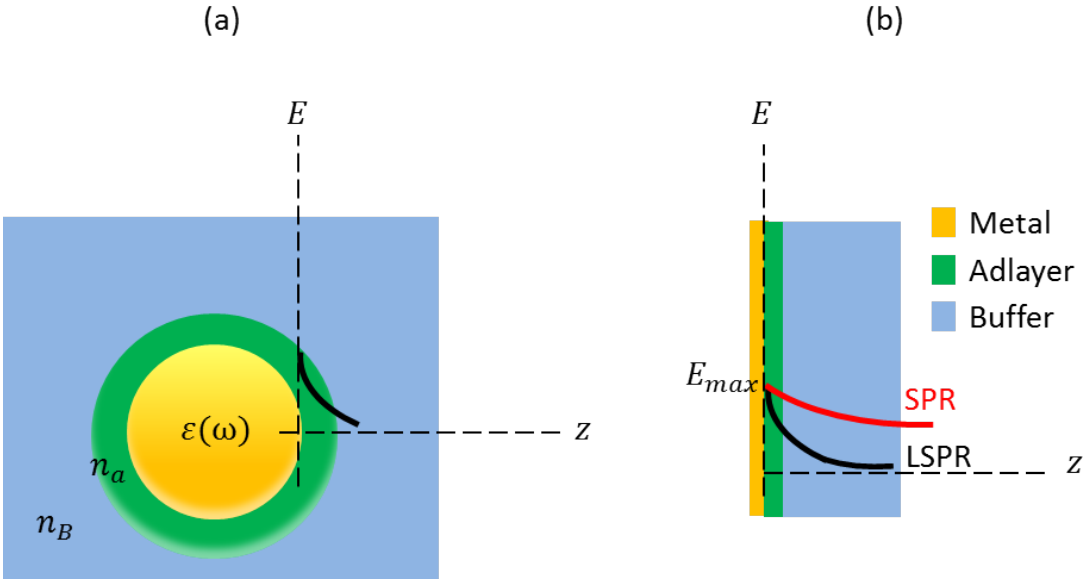

Figure 2–11: (a) Schematic for a metal nanoparticle surrounded by an adlayer of a refractive index (n_a) and buffer (n_B). The short EM decay length associated with metal nanoparticles increases specificity to the adlayer and reduces the effect of bulk RI change. (b) A comparison between LSPR with SPR sensor in terms of EM decay length.

2.5.1 Sensitivity

Sensitivity is the primary characteristic of a sensor. However, in some applications, we are mainly concerned with sensitivity to changes in bulk refractive index, whereas for others (in particular for biosensing) we are mainly concerned with sensitivity to binding of adlayer molecules to the surface. For bulk refractive index sensing we can express the bulk RI sensitivity as the rate of change in the sensor response to the changes in bulk refractive index (n_B), as shown in Fig. 2–12.

$$S_B = \frac{\partial R}{\partial n_B} \tag{2.34}$$

Based on the quasistatic approximation, the sensitivity for a metal nanosphere is given by [69]

$$S_B = \frac{-4}{\frac{d\varepsilon_r}{d\lambda}} n_B \tag{2.35}$$

Here, the sensitivity for a nanoparticle of an arbitrary shape and dielectric constant is to be

determined. The resonance occurs when $\varepsilon_r = (1-1/\rho)\,\varepsilon_b$ [Eq. (2.12)]. Substituting $\varepsilon_b = n_B^2$, this becomes

$$\varepsilon_r = (1 - 1/\rho)\, n_B^2$$

Differentiating both sides with respect to λ, we obtain

$$\frac{d\varepsilon_r}{d\lambda} = 2n_B(1 - 1/\rho)\,\frac{dn_B}{d\lambda} \tag{2.36}$$

where $S_B(\lambda) = d\lambda/dn_B$ is the bulk RI sensitivity. Substituting in Eq. 2.36

$$\frac{d\varepsilon_r}{d\lambda} = 2\frac{n_B}{S_B}(1 - 1/\rho)$$

This can be solved for S_B as follows

$$S_B(\lambda) = \frac{2\,n_B}{\frac{d\varepsilon_r}{d\lambda}}(1 - \frac{1}{\rho}) \tag{2.37}$$

The bulk RI sensitivity can also be derived from Eq. (2.18)

$$\frac{\lambda_r^2}{\lambda_p^2} = \varepsilon_\infty - \varepsilon_b(1 - 1/\rho) \equiv \varepsilon_\infty - n_B^2(1 - 1/\rho) \tag{2.38}$$

Differentiating both sides with respect to λ_r, we obtain

$$\frac{\lambda_r}{\lambda_p^2} = -n_B\frac{dn_B}{d\lambda_r}(1 - 1/\rho)$$

Substituting $S_B(\lambda_r) = d\lambda_r/dn_B$, we obtain

$$S_B(\lambda_r) = n_B(\frac{1}{\rho} - 1)\,\frac{\lambda_p^2}{\lambda_r} \tag{2.39}$$

This equation relates the RI sensitivity to the shape factor regardless of the dielectric properties of metal nanoparticles, explaining why nanorods exhibit higher sensitivity than that of nanospheres.

From Eq. (2.38), $(1-1/\rho) = (\lambda_r^2/\lambda_p^2 - n_\infty^2)/n_B^2$. Substituting in Eq. (2.39), the sensitivity

of metal nanoparticles–regardless of their shapes– can be obtained as follows [70]

$$S_B(\lambda_r) = \frac{\lambda_r}{n_B}(1 - \frac{\lambda_p^2}{\lambda_r^2} n_\infty^2) \tag{2.40}$$

where $\lambda_p \sim 136\, nm$ is the plasma wavelength for gold and silver, and $n_\infty \sim 1.9,\ 3.1$ for silver and gold respectively, is the background refractive index originating from the polarizability of the bound electrons in the d-band. Therefore, silver always provides a higher sensitivity than that of gold for nanoparticles of the same shape. The effect of the shape factor is included in the resonance wavelength, λ_r in Eq. (2.40) as reducing the shape factor (high AR) increases λ_r, and hence increases the sensitivity.

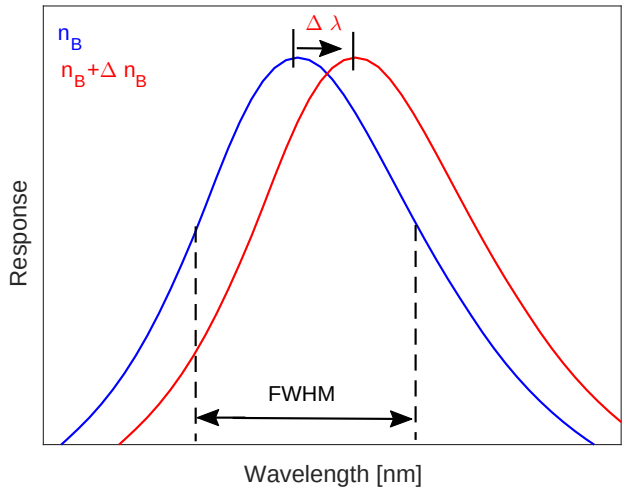

Figure 2–12: Typical Response of LSPR sensor (extinction in the figure, but it can be transmission). The red shift is due to change in the bulk refractive index.

The sensitivity to a biological adlayer thickness d; and the sensitivity to the adlayer refractive index n_a can be determined as follows

$$S_{n_a} = \frac{\partial R}{\partial n_a},\ \ S_d = \frac{\partial R}{\partial d} \tag{2.41}$$

In a sense, the thickness of a bimolecular adlayer causes a shift in the resonance wavelength, but its RI determines the amount of that shift, and hence it is important to take the adlayer RI into account when comparing different sensors based on the adlayer sensitivity.

The adlayer thickness, the adlayer refractive index n_a and bulk refractive index n_b contribute to the effective refractive index n_{eff}. Therefore, the adlayer sensitivity can be given by [71]

$$\frac{\partial R}{\partial d} = \frac{\partial R}{\partial n_{eff}} \frac{\partial n_{eff}}{\partial d}$$

This equation suggests that the adlayer sensitivity is determined by the bulk RI sensitivity and at what rate the adlayer thickness contributes to the effective refractive index n_{eff}. The above equation can be rearranged as follows

$$\frac{\partial n_{eff}}{\partial d} = \frac{S_d}{S_B} \tag{2.42}$$

where $S_d = \partial R/\partial d$, and $S_B = \partial R/\partial n_{eff}$ This equation will be used in Chapter 5 to compare the LSPR modes associated with gold nanocrescent structures.

2.5.2 Figure of Merit (FoM)

Figure of merit provides the ratio of a sensor's sensitivity to the line width: the full width at half maximum (FWHM) of resonance curve. Therefore, FoM can be used to compare different sensors as higher FoM is desirable. Referring to Fig. 2–12, the spectral full width at half maximum response (FWHM) is used to calculate the sensor FOM as follows [72]

$$FoM = \frac{S_B}{FWHM}(RIU^{-1}) \tag{2.43}$$

The FWHM has been previously determined based on the quasistatic approximation [69]

$$FWHM = \left| \frac{2\,\varepsilon_i(\lambda_r)}{\frac{d\varepsilon_r}{d\lambda}\Big|_{\lambda=\lambda_r}} \right|$$

The denominator can be substituted with the differentiation of Eq. (2.13)

$$FWHM = \left| -\varepsilon_i(\lambda_r)\frac{\lambda_p^2}{\lambda_r} \right| \tag{2.44}$$

The FoM for metal nanoparticles can be determined as

$$FoM = \Big|\frac{S_B}{FWHM}\Big| \equiv \begin{cases} \frac{2n_B}{\varepsilon_i(\lambda_p)}, & \text{nanosphere} \\ \frac{n_B}{\varepsilon_i(\lambda_r)}(\frac{1}{\rho} - 1), & \text{spheroid or nanorod.} \end{cases} \tag{2.45}$$

Therefore, the FoM is directly related to the material properties of the metal used to synthesize the nanoparticles, as metals with high losses (large imaginary dielectric constant) yield broad resonance curves and degrade the FoM. Silver nanoparticles support a sharper resonance curve than that associated with gold nanoparticles, due to the lower imaginary dielectric constant and higher bulk RI sensitivity. Nanorods and spheroids possess a higher FoM than that of nanospheres, due to their increased bulk RI sensitivity and size (shape factor). However, as the dimension increases, radiation damping arises, broadening the resonance curve.

2.5.3 Signal to Noise ratio

Signal to noise ratio is defined as the average measured response ($\overline{R}$) to its standard deviation (σ_R). The measured sensor response can be the resonance shift, the change in measured intensity, or the change in estimated refractive index (which is the case in the projection method, undertaken in this thesis). Mathematically,

$$SNR = \frac{\overline{R}}{\sigma_R} \tag{2.46}$$

2.5.4 Refractive index resolution and Limit of Detection(LoD)

Sensing platforms yield different quantities (wavelength, intensity, angle) as a response to changes in refractive index or biding events. It is proper to characterize these sensors based on the minimum detectable change in refractive index (indicating the RI resolution) if the sensor is intended for bulk RI sensing experiments, or the minmum detectable concentration of a target analyte (LoD) for surface binding sensing applications. The RI resolution can then be predicted as the RI change that corresponds to a sensor response equivalent to the

standard deviation of the sensor response to the base sample. This can be expressed as [73]

$$\sigma_{RI} = \frac{\sigma_R}{S_B} \tag{2.47}$$

Here the sensitivity is used to translate the sensor response (intensity difference, wavelength shift, or angle shift) into bulk refractive index resolution (in RIU). Similarly, the LoD can be predicted as the minimum concentration of analyte that produces a sensor response equal to 3 times the standard deviation of a response to a blank sample (buffer) [73]. Mathematically, this can be expressed as follows

$$R_{LoD} = 3\ \sigma_R \tag{2.48}$$

The LoD can be predicted in real time sensing experiments based on low concentrations of analyte and determining their standard deviation σ_R. It can also be determined based on the slope of a sensor response against various concentrations of the analyte, as shown in Fig. 2–13 (c)

$$LoD = \frac{3\ \sigma_R}{S_A} \tag{2.49}$$

where $S_A = dR/dA$ is the sensitivity with respect to the analyte concentration, which is proportional to the adlayer sensitivity S_d defined in Eq. (2.41). This suggests that the limit of detection can be improved by increasing the sensitivity and the RI resolution σ_{RI} of a sensor.

In terms of SNR, the RI resolution and limit of detection are determined when $SNR_{\sigma_R} = 1$, and $SNR_{LoD} = 3$, respectively. This suggests that a higher SNR is used to determine the LoD to tolerate the uncertainties due to different sensing experimental conditions, such as surface chemistry (ligand immobilization) and ligand–analyte binding. A lower SNR is used in determining RI resolution as it is extracted from bulk RI sensing experiments, which are not impacted by the aforementioned effects (surface chemistry and binding events). Fig. 2–13 (e) shows the PDF distribution of the sensor response with and without the presence of analyte when using σ_R as a reference. The probability of obtaining false negative or positive results is 30%, whereas this uncertainty can be reduced to $\sim$ 5% when the LoD

(corresponding to $3\,\sigma_R$) is used as a reference, as shown in Fig. 2–13 (e). Therefore, the limit of detection is chosen in characterizing a biosensor to increase the precision. To obtain even a higher precision, the limit of quantitation or quantification LoQ can be used, as it corresponds to a sensor response of $10\,\sigma_R/S_A$.

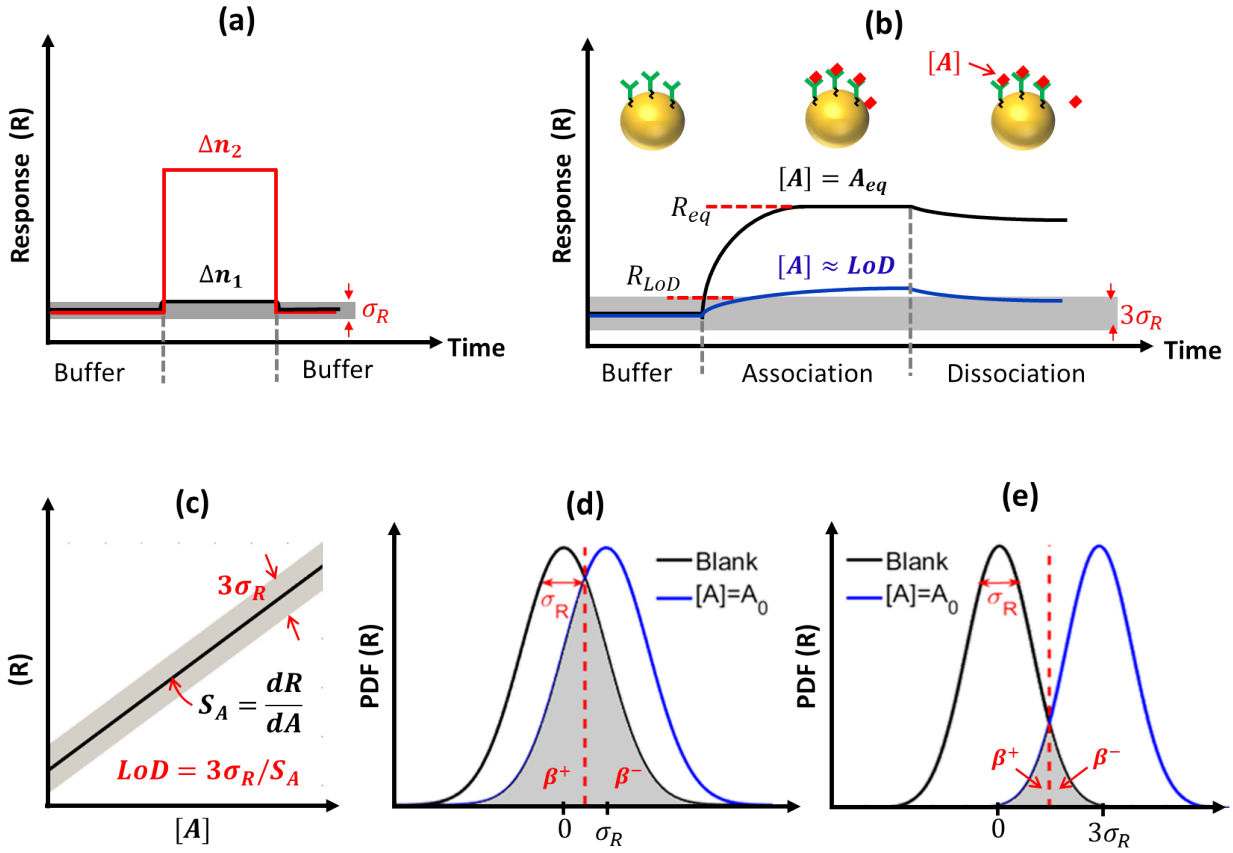

Figure 2–13: (a) Real time LSPR sensing of bulk RI change.(b) A sensogram for LSPR sensor kinetics. R_{eq} is the equilibrium response when the association and dissociation become equal, corresponding to an analyte concentration A_{eq}. (c) Determining the LoD based on $3\sigma_R$ and the slope S_A of the sensor response to various sample concentrations, which is proportional to the adlayer sensitivity $\sim S_A \propto S_d$. (d) PDF of sensor response to a blank sample (no analyte is present) with zero mean and standard deviation σ_R. A sensor response with σ_R is obtained with analyte concentration $[A] = A_0$, exhibiting 30% error representing either false negative β^- or false positive β^+ results (the shaded area under the overlapped normal distributions). (e) PDF of sensor response without analyte (blank) and with analyte of a concentration $[A] \approx LoD$, causing a response $\sim 3\,\sigma_R$. Here, the probability of obtaining false negative β^- or false positive β^+ results decreases to 5%, justifying the adoption of the LoD in characterizing different sensors. In some cases, a concentration of the LoQ is used based on $10\,\sigma_R$ response to increase the accuracy of the results.

2.6 Previously demonstrated nanostructures and LSPR sensors

The plasmonic properties of metal nanoparticles have driven considerable advances in a wide range of fields including biosensing. This section reviews the progress in LSPR sensing.

Although the phenomenon of light interaction with nanoparticles was discovered by Michael Faraday in 1857 [74], and a physical understanding was provided by Mie in 1908 [52], the first sensor, exploiting the plasmonic properties of metal colloids, was reported in 1998 by Englebienne [75]. Since 2000, the field has witnessed an explosive growth, starting from the synthesis of gold nanorods, improving the sensitivity and tunability of LSPR resonance [76–81], as metal nanoparticles and nanorods have represented the first sensing platforms for a wide range of sensing applications.

Due to the progress in nanofabrication and engineering metal nanostructures, metal nanostructures have exhibited attractive optical phenomena, such as the extra–ordinary transmission of light (EOT). When a light wave strikes a periodic structure of subwavelength aprtures in a metal film, the transmitted light can be orders of magnitude larger than that expected by standard aperture theory [83–86]. This phenomenon has fueled an explosion of interest in biosensing applications [87–89], a hybrid biosensing platform molding the flow of light and fluidics was demonstrated in [89], where suspended plasmonic nanohole arrays were used as plasmonic sensors and nanofluidic channels, connecting both sides of the metal film to transport biological samples, as shown in Fig. 2–14. This sensor features 630 nm/RIU bulk RI sensitivity, and its main advantage is the analyte transport through the nanoholes, maximizing the ligand–analyte binding events.

Other platforms based on metallic nanostructures have emerged to improve the FoM and bulk RI sensitivity. A nanorod metamaterial has improved the sensitivity based on the guided mode, stemming from the excitation of the transverse and longitudinal modes together. Similar to propagating SPR, the guided mode excitation requires a controlled angle of incidence and maintaining p-polarization of the incident light wave [12]. Gold nanoshells were previously used to excite a hypridized mode, featuring increased sensitivity to bulk refractive index [29].

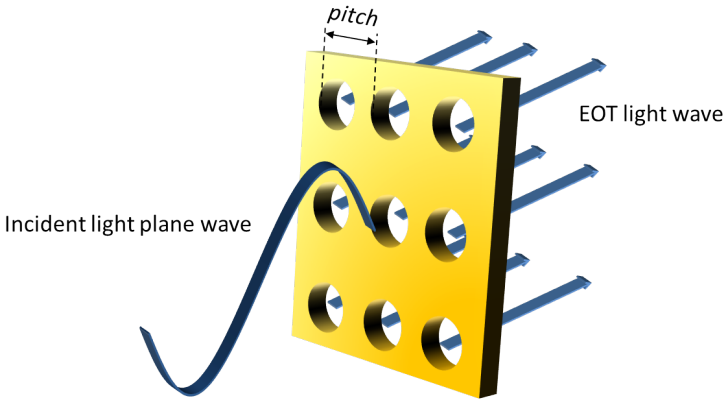

Figure 2–14: Periodic nanohole structures in a thick metal film, illustrating the extraordinary transmission of light. The resonance peak can be controlled by the diameter and the pitch of the nanoholes.

The advantage of tunable resonance of metallic nanostructures has paved the road towards more applications, such as multiplexing and self-referencing. Spectral multiplexing is challenging in the case of propagating SPR. A wavelength division multiplexed SPR sesnor was established by locating a dielectric layer over a part of the SPR surface or using a special prism as shown in Fig. 2–15, exciting two resonances [90]. Such system is complex and provides a limited number of sensing channels (only two channels).

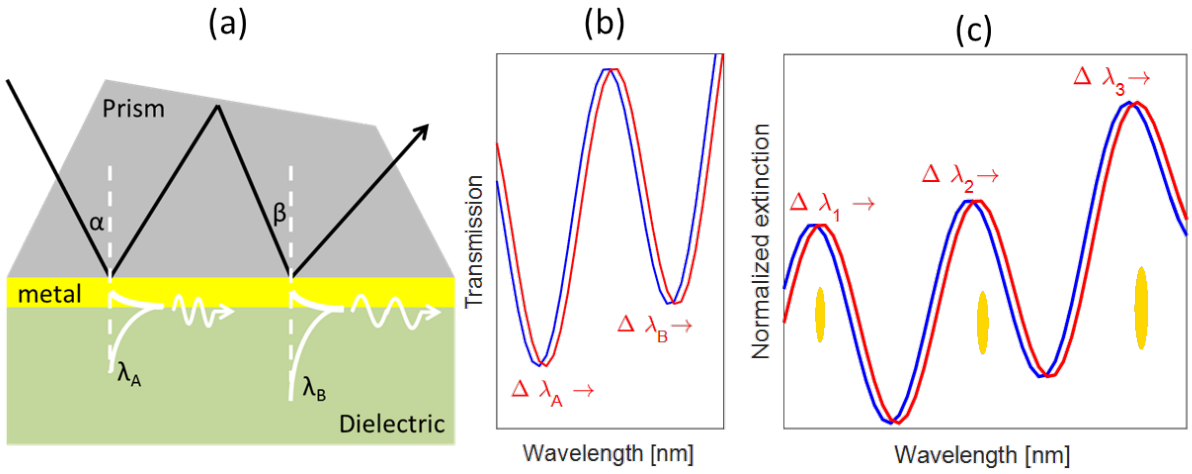

Figure 2–15: (a) A multiplexed SPR platform based on multiple resonant angles associated with a special prism, yielding (b) a multiple resonance curve. (c) A multiple resonance curve based on a LSPR sensor, employing metal nanorod structures.

Unlike the wavelength division mutiplexed SPR sensor, gold nanorods can yield more sensing channels with simpler instrumentation by tuning their aspect ratio [91–93]. The nanorods were fabricated by the seed-mediated growth [77], and then surface activated by alkanethiols to attach the antibodies to produce gold nanorod molecular probes (GNRMP). The nanorods had aspect ratios 2.1, 4.5, and 6.5, and each was functionalized to a different target analyte, as illustrated in Fig. 2–15 (b). Aggregation and cross talk are the main disadvantage of such multiplexed sensor as the rods are not stable in the solution.

A recent work has overcome the aggregation of nanorods, where antibodies were thiolated and used to functionalize nanorods of different aspect ratio [93]. The functionalized nanorods were then bound to different locations on a glass substrate. The antigens were then injected to the sensing chip, binding with their capturing antibodies. The number of channels can be increased by using the micro-channel spectroscopy system. The multiple nanorods presented in this thesis can be used for multiplexed sensing with improved isolation and reduced surface chemistry procedure (used in [93]) as the nanorods are imprinted directly on a substrate using the side wall lithography method. However, this thesis will use the multiple resonance nanostructures in self-referenced LSPR sensing and leave the multiplexing for future work. Table 2.2 summarizes the characteristics of reported LSPR sensors based on synthesized and patterned nanostructures.

Table 2.2: Characterisitics of reported LSPR sensors

structure	Dimension [nm]	λ_{LSPR} [nm]	characteristic	S_B $[nm/RIU]$	Ref.
Au spheres	15 – 50	450 – 600	shape dependent	44 – 76	[26]
Ag spheres	35	450 – 700	shape dependent	161	[9]
Ag triangles	35	450 – 700	shape dependent	197	[9]
Nanostars	core:30 – 50 cone tip:10 – 60	550 – 750	multiple-resonance	218	[94]
Nanodisks	pitch:162,340	500 – 1000	Anisotropic property	170,174	[95]
Nanorods	L:40 – 74, w:17	653 – 846	longitudinal mode	195 – 288	[26]
Hollow Au nanoshell	Diameter:3.5 wall thick:4.5	550 – 750	shape dependent	408	[26]
Nanocubes	100, 40	350 – 650, 538	sharp– quadrupole mode	165, 83	[96] [20]
Au pyramids	27 – 189,	645 – 1096,	shape dependent	150 – 540	[20]
Ag nanoprism coated Au	21 – 22	940	shape dependent	470	[97]
Au nanorings	75 – 150	1058 – 1545	shape dependent	880	[98]
Au nanorice hematite core	9.8 – 27.5	1160	hybridized-mode	800	[28]

2.7 Established data extraction methods

Metallic nanostructure-based sensors can operate either in wavelength or intensity interrogation modes; in the wavelength interrogation mode, the sensor is excited by a broadband light beam and the spectrum is collected in real time; for the intensity interrogation mode, a monochromatic laser beam excites the nanostructures, and the transmitted beam is focused on a photodetector that measures the change in the intensity with respect to changes in bulk refractive index or surface binding events. The latter is more impacted by noise due to the intensity fluctuations of the light source, and hence the detection error is more pronounced in this case. The dip-finding method can be used to process the sensor data where the dip of the resonance curve is tracked simultaneously and a sensorgram can be generated for binding events in real time [99]. Several data processing methods have tar-

geted SNR improvement of conventional SPR sensors: the centroid and full-width-at-half-maximum tracking method [100, 101], principle component and locally weighted parametric regression [102], optimal linear data analysis [103], polynomial curve-fitting of the measured curve [104], statistical hypothesis testing [105], and a double projection method [106]. The integration method was applied to nanohole-structure sensors [88] — based on the extraordinary transmission of light arising from the propagating surface plasmon resonance [83–86], and the normalized-difference integrated-response method was used to improve the sensitivity of multispectral thin film biosensing imaged with 3-D photonic crystals [107].

The dynamic-baseline centroid method [101] uses a threshold value (usually the FWHM) to estimate the resonance wavelength (λ_r) as follows

$$\lambda_r = \frac{\sum_j j\,(R_{thresh} - R_j)}{\sum_j (R_{thresh} - R_j)} \tag{2.50}$$

where R_j are the transmission values below the threshold value (R_{thresh}), and (j) correspond to the wavelength data points. The fixed boundary method uses the same wavelength range over which the centroid calculations– for all the measured spectra–are performed. This simplifies the calculations as follows [108]

$$\lambda_r = \frac{\sum_j j\,R_j}{\sum_j (R_j)} \tag{2.51}$$

where R_j spans the response (transmission) values over the wavelength range. The integrated response method was introduced in order to improve the performance of a nanohole SPR sensor and has previously been compared to the peak shift method (dip-finding method) and normalized difference integrated response [88]. The integrated response method is based on intensity difference calculations, I_{int}, using the following equation [88]

$$I_{int} = \left(\int_{\lambda_1}^{\lambda_2} \left| D^2(\lambda) - \overline{D^2(\lambda)} \right| d\lambda \right)^{1/2} \tag{2.52}$$

where $D(\lambda) = R_{ref}(\lambda) - R(\lambda)$ is the difference between the reference and measured signals, and $\overline{D^2(\lambda)}$ is the mean of the total squared differences. The normalized difference integrated

response (NDIR) technique uses data within a wavelength range ($\lambda_1 - \lambda 2$) by applying the following equation [107]

$$NDIR = \int_{\lambda_1}^{\lambda_2} \left| \frac{R_{ref}(\lambda) - R(\lambda)}{R_{ref}(\lambda)} \right| d\lambda \tag{2.53}$$

where $R_{ref}(\lambda)$ and $R(\lambda)$ are the reference and measured signals, respectively.

In chapter 4 I will introduce the projection method to extract the refractive index directly from measured data with increased accuracy and precision, and compare it to the methods described above.

2.8 Self–referenced SPR and LSPR sensing

This section explores methods used in implementing self-referenced sensors. In propagating SPR sensors, a reference channel is required to compensate for artifacts due to temperature drift and bulk RI change [109]. However, the reference sensing channels are not identical (for example: different metal thickness) due to fabrication imperfections, the difference in analyte transport in both channels [110], and the uncorrelated effects in each channel during the binding events (presence of air bubbles and changes in speed of fluid flow in either channel [111]). These artifacts have motivated many researchers to seek for alternative methods where the reference channel can be abandoned to avoid any external or intrinsic effects in the two-channel sensing platforms. A self referenced SPR sensor has previously employed the excitation of a dual mode SPR (with different penetration depths) using two laser sources [112]. This can be challenging as it further increases the complexity of the instrumentation. A dual-mode SPR platform was used as reference/sensing channels, but each mode was excited at a different location on the metal surface, degrading the accuracy of the system [113]. Alternative approaches exploited the excitation of the long range and short range surface plasmons on the same location of the SPR surface [114] [115] based on the linear resonse model. Similarly, the linear response model was applied to gold nanorod structures, U-shaped structures and propagating plasmon waveguide resonance biosensor to achieve self-referenced sensing [116–118]. Although various approaches have been introduced

for self-referencing SPR platforms, less effort has been previously paid to self-referenced LSPR sensors. This section highlights the established progress in LSPR self-referencing and presents the linear response model, that will be revisited in the remainder of the thesis.

2.8.1 Nanorod structures

Gold nanorods have been used in distinguishing surface binding interactions from interfering bulk interactions by utilizing the longitudinal and transverse modes [116]. Assuming that the longitudinal and transverse surface plasmon resonances are linearly dependant on the changes in the solution refractive index and to the surface coverage of bound analyte. The response at each resonance can be expressed as follows

$$\Delta\lambda_L = S_{\lambda L}\Delta n_B + S_{sL}\Delta C_s \tag{2.54}$$

$$\Delta\lambda_T = S_{\lambda T}\Delta n_B + S_{sT}\Delta C_s \tag{2.55}$$

where $S_{\lambda L}$ and $S_{\lambda T}$ represent the sensitivity of each mode to the bulk refractive index, Δn_B; and S_{sL} and S_{sT} represent the sensitivity to surface binding, ΔC_s, of the longitudinal and transverse plasmon modes respectively. Provided that the bulk and surface sensitivities and transverse and longitudinal resonance wavelength shifts are known, the surface coverage and bulk index changes can be calculated directly from the above equations.

2.8.2 U-shaped nanostructures

Similar to nanorod structures, U-shaped structures support three plasmon resonances that can distinguish the nonspecific and specific interactions from the bulk interations [117]. Assuming a linear relationship between each LSPR wavelength shift $\sim \Delta\lambda_i$ and surface coverage of specific , nonspecific binding, and the bulk refractive index of the solution [117].

$$\Delta\lambda_i = S_{B,i}\,\Delta n_B + S_{S,i}\,\Delta C_S + S_{NS,i}\,\Delta C_{NS}$$

The bulk RI change (Δn_B), the specific surface coverage (ΔC_S) and non-specific surface coverage ΔC_{NS} can be directly calculated from three equations (i=3), corresponding to the three resonance shifts employing the bulk sensitivity ($S_{B,i}$), and specific and non-specific surface binding sensitivities, $S_{S,i}$ and $S_{NS,i}$. This model assumes that the nonspecific binding occurs on the substrate of the sensing substrate and the specific binding corresponds to the binding events on the functionalized metal surface and the nonspecific binding at a distant location from the metal surface (on the substrate). However, this assumption ignores any nonspecific binding that may occur at the metal surface with interfering biomolecules. In addition, the fabrication of such structures has required an expensive and time-consuming fabrication methods; electron beam lithography was used in [117].

2.8.3 Self-referenced sensor based on plasmon waveguide resonance biosensor

A plasmon waveguide resonance biosensor was introduced as a self-referenced SPR sensor [118]. Its configuration consists of a conventional SPR sensor loaded with a dielectric layer. This dielectric layer guides transverse electric (TE) along with transverse magnetic (TM) modes supported by the conventional SPR. The dual–mode platform was used as a self-referenced sensor, assuming a linear dependence of the angular shift (at each polarization) on the adlayer and bulk RI change. Similar to the system of equations developed for the gold nanorods (section 2.8.1), the adlayer and bulk RI change can be estimated.

In chapters 5 and 6, novel methods, based on the maximum likelihood estimation, will be introduced to improve self–referencing and enhance the precision and accuracy of the estimated adlayer and bulk RI change.

2.9 Kinetics analysis for binding events

This section presents a brief overview of the principles of kinetics in real time biosensing. The response of an affinity biosensor can be represented by three phases: (1) the association phase, when the analyte binds with the biorecognition element (Ligand); (2) equilibrium phase, or the steady state of the sensor response; and (3) the dissociation phase, when the concentration of the analyte in the flow cell becomes zero, and the sensor response starts to

decay exponentially with time.

Mathematically, the sensor response as a function of time for a given analyte concentration [A] can be expressed by the following relationship [119]

$$R(t) = \begin{cases} \frac{R_{max}[A]}{K_D+[A]}\left[1 - exp(-k_{on}\,[A] + k_{off})\,t\right] & \text{association} \\ R_0\, exp(-k_{off}\,(t - t_0)) & \text{dissociation} \end{cases} \tag{2.56}$$

where k_{on} and k_{off} are the association and dissociation constants. R_{max} denotes the maximum sensor response, which is reached when all the immobilized ligands bind with the target analyte, and t_0 and R_0 represent the initial time and sensor response when the analyte is washed out of the flow cell. K_D is the affinity constant, $K_D = k_{off}/k_{on}$. This can be used to reproduce sensograms published by Biacore [120], illustrating the effect of the binding coefficients k_{on} and k_{off}, and different concentrations on the the sensing kinetics, as shown in Fig. 2–16.

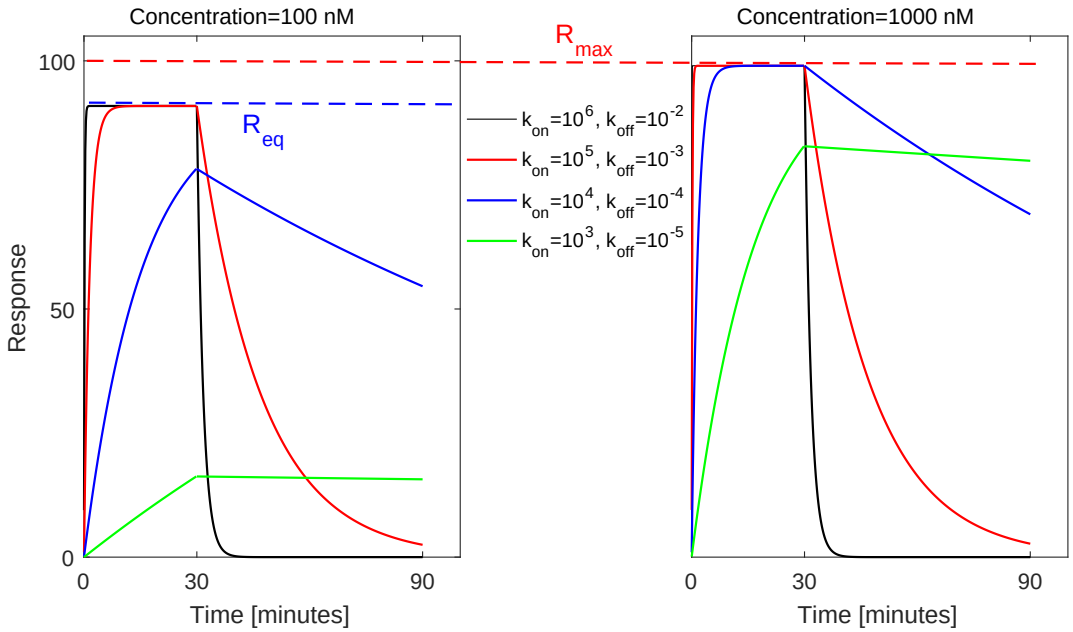

Figure 2–16: Typical sensograms for sensing kinetics of different values for the association and dissociation constants and analyte concentration.

2.10 Summary

This chapter navigated through the basic concepts related to the plasmonic properties of metallic nanoparticles, and highlighted the advantages of adopting metal nanostructures for numerous sensing applications. The chapter reviewed the analytical and numerical methods used to calculate the optical cross sections of nanoparticles and other complex nanostructures. The results indicate that metallic nanostructures and nanoparticles possess remarkable plasmonic properties, such as the tunable resonance wavelength and multiple resonance excitation. Their advantages as biosensors include cost–effectiveness, simple instrumentation, and the miniaturized dimension (requiring reduced sample volume and motivating towards a Lab on Chip or point of care sensing applications). The chapter manifested a diverse range of sensing applications based on metallic nanostructures. Lastly, the chapter provided brief definitions for sensor parameters that will be employed throughout the remainder of the thesis.

3

Numerical and experimental study of the fabricated structures

This chapter presents a complete study of the fabricated nanostructures, including the simulated and measured extinction cross sections, and their surface characterization using Scanning Electron Microscope (SEM). The fabricated nanostructures are also characterized by Near Field Scanning Optical Microscope (NSOM) that also provides Atomic Force Microscope (AFM) imaging. This chapter first validates the numerical methods by comparing the results to the calculated Mie solution for a sphere. COMSOL-Multiphysics v5.2, a commercial package based on the Finite Element Method (FEM), is used to calculate the absorption, scattering and extinction cross sections, as well as the local electric field distributions supported by the nanostructures. The Finite Difference Time Domain (FDTD) modeling is

based on the Drude Lorentz model for the dielectric properties of gold, whereas the FEM is based on the reported refractive index (RI) values by Johnson and Christy [48].

3.1 Validation of FEM and FDTD models based on Mie theory

This section describes the modeling of the nanostructures based on the FEM and FDTD methods, and compares the results with reference data. The extinction, scattering, and absorption cross sections for gold nanoparticles calculated using Mie theory and the quasi-static model are used as a reference.

The FEM simulation used a far field sphere surrounding the nanoparticle, and five perfectly matched layers to model free space (eliminating the reflections from the boundary). The dielectric permittivity for gold is obtained by interpolating the reported values by Johnson and Christy [48]. The magnetic field is related to the incident electric field by

$$\mathbf{H_{inc}} = \frac{1}{\eta}\hat{\mathbf{k}} \times \mathbf{E_{inc}} \tag{3.1}$$

where $\hat{\mathbf{k}}$ is the propagation direction of the incident plane wave, and $\eta \sim \sqrt{\mu/\varepsilon}$ is the medium characteristic impedance, ε and μ are the electric permittivity and magnetic permeability of the medium. The Poynting vector provides the incident energy flux density for time harmonic EM field

$$\mathscr{P}_{inc} = \frac{1}{2} Re\{\mathbf{E_{inc}} \times \mathbf{H^*_{inc}}\} \equiv \frac{1}{2\eta}|\mathbf{E_{inc}}|^2\hat{\mathbf{k}},\ (W/m^2) \tag{3.2}$$

The total energy losses by the particle includes the conduction, polarization and magnetic losses, and is expressed as follows

$$Q_{loss} = \frac{1}{2}\, Re\{\mathbf{J_t}.\,\mathbf{E}^* + j\omega\mathbf{B}.\mathbf{H}^*\},\ (W/m^3) \tag{3.3}$$

where the total current density $\mathbf{J_t}$ includes the conduction and displacement currents, $\mathbf{J_t} = \sigma\mathbf{E} + j\omega\mathbf{D}$, and σ denotes the conductivity. The absorption rate can be calculated by

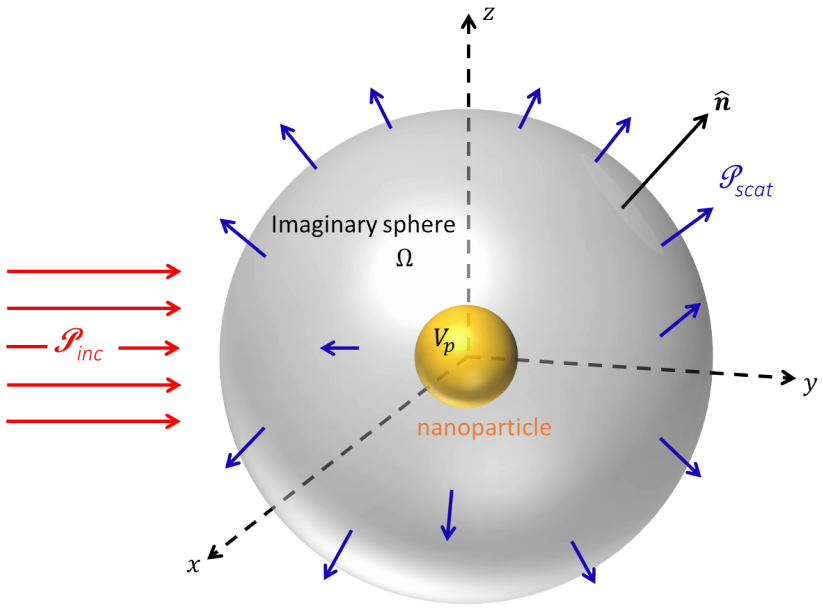

Figure 3–1: Energy flux $\mathscr{P}_{inc}$ of an incident EM field on a metal nanoparticle with volume V_p. The rate by which the incident field is scattered is obtained by integrating the energy flux of the scattered field $\mathscr{P}_{scat}$ over the surface of the imaginary sphere Ω. The vector $\hat{n}$ normal to the imaginary sphere is also shown.

integrating the energy losses over the nanoparticle as follows

$$W_{abs} = \iiint_{V_p} Q_{loss}\, dV,\ (W) \tag{3.4}$$

The scattering rate is calculated by integrating the Poynting vector for the scattered field $\mathscr{P}_{scat}$ over the surface of an imaginary sphere around the particle Ω, as shown in Fig. 3–1

$$W_{scat} = \oiint_{\Omega} \mathscr{P}_{scat} \cdot \hat{\mathbf{n}}\, d\Omega \tag{3.5}$$

$$= \frac{1}{2} \oiint_{\Omega} Re\{\mathbf{E_{scat}} \times \mathbf{H^*_{scat}}\} \cdot \hat{\mathbf{n}}\, d\Omega,\ (W) \tag{3.6}$$

where $\mathbf{E_{scat}}$ and $\mathbf{H_{scat}}$ are the scattered electric and magnetic fields, respectively, and $\hat{\mathbf{n}}$ is a unit vector normal to the imaginary sphere. The scattering and absorption cross sections can be calculated as the ratio of scattering and absorption rates by the incident energy flux

as follows

$$C_{scat} = \frac{W_{scat}}{\mathscr{P}_{inc}},\ C_{abs} = \frac{W_{abs}}{\mathscr{P}_{inc}} \tag{3.7}$$

where W_{scat} and W_{abs} are the rates at which the energy is scattered and absorbed by the nanoparticle, respectively, and $\mathscr{P}_{inc}$ is the irradiance of the incident intensity flux (W/m^2).

The extinction cross section was also calculated based on the optical theorem (OT), by using a reference point along the forward direction of the incident plane wave ($E_{inc}\, e^{-kz}$). The wave amplitude in the far field region is related to both incident and scattered waves as $\sim [e^{-kz} + f(\theta)e^{-jkr}/r]$, where $f(\theta)$ is the scattering amplitude at a certain scattering angle (θ). The optical theorem calculates the extinction cross section based on the scattering in the forward direction ($\theta = 0$) as follows

$$C_{ext} = \frac{4\pi}{k}\frac{Im\{f(0)\}}{E_{inc}} \tag{3.8}$$

Fig. 3–2 compares the results obtained by COMSOL Multiphysics and Mie theory. The results match each other, confirming the damping effect associated with nanoparticles larger than 100 nm as scattering becomes dominant. Absorption cross section contributes more than the scattering cross section to the extinction cross section in the case of the small particle, 80 nm diameter sphere, as expected by the quasistatic approximation.

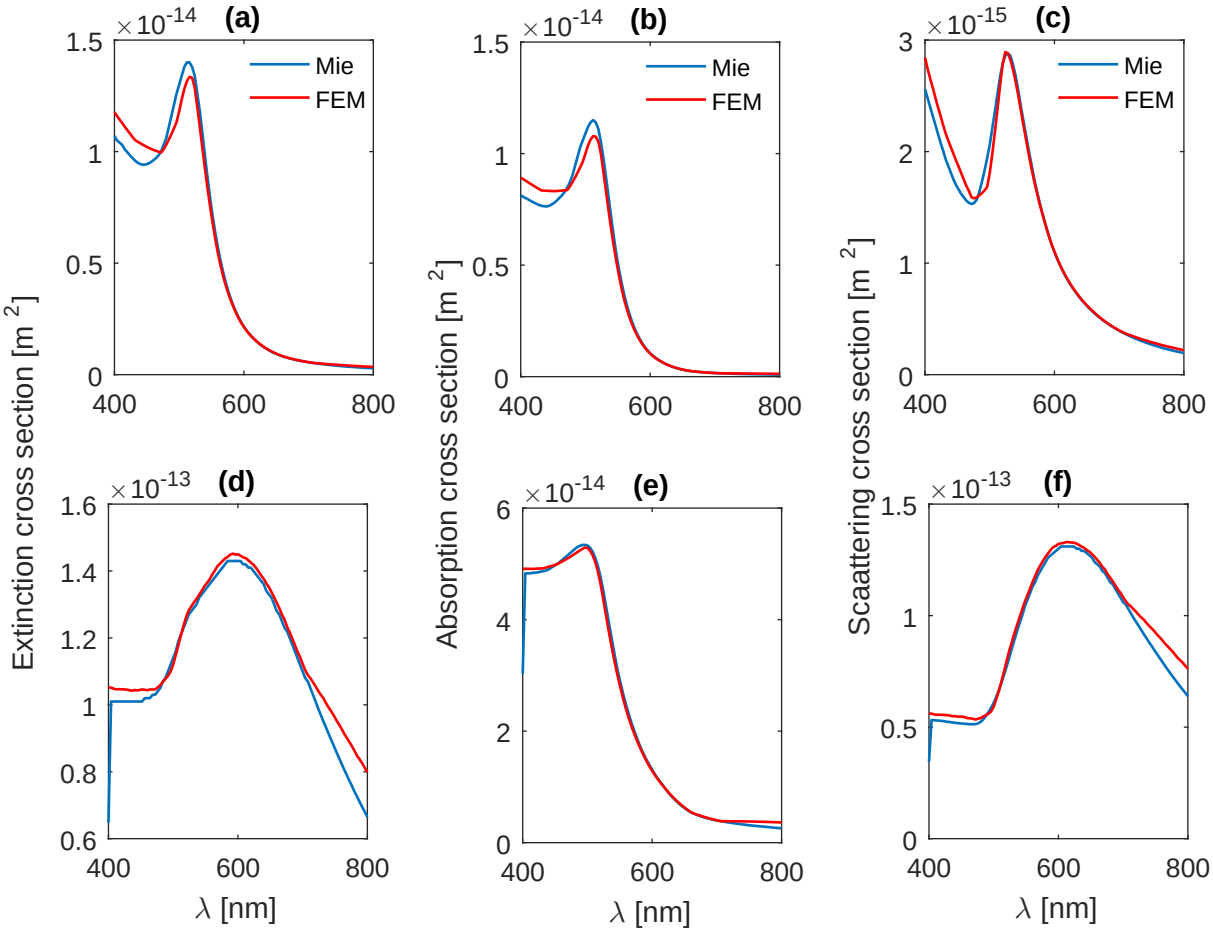

Figure 3–2: FEM results and Mie calculations of (a) extinction, (b) absorption and (c) scattering cross sections for a gold sphere with a diameter of 80 nm. (d, e, f) Repeated calculations for a sphere with 120 nm diameter.

The OptiFDTD was also used to estimate the absorption, scattering and extinction efficiencies associated with the gold sphere, as OptiFDTD can calculate only transmission and reflection efficiencies. Fig. 3–3 shows a schematic for the simulation domain used in OptiFDTD to model periodic nanospheres, as a single nanosphere is placed in the simulation domain (a cube in this case), and periodic boundary conditions were enforced along the boundaries in x and y directions. To minimize reflections from the simulation domain, Perfect Matched Layer (PML) boundary conditions were enforced along the boundaries in z direction (behind the input and output observation areas). The observation areas (rectangles) are placed behind and in front of the nanoparticle to collect the reflected and

transmitted power, respectively.

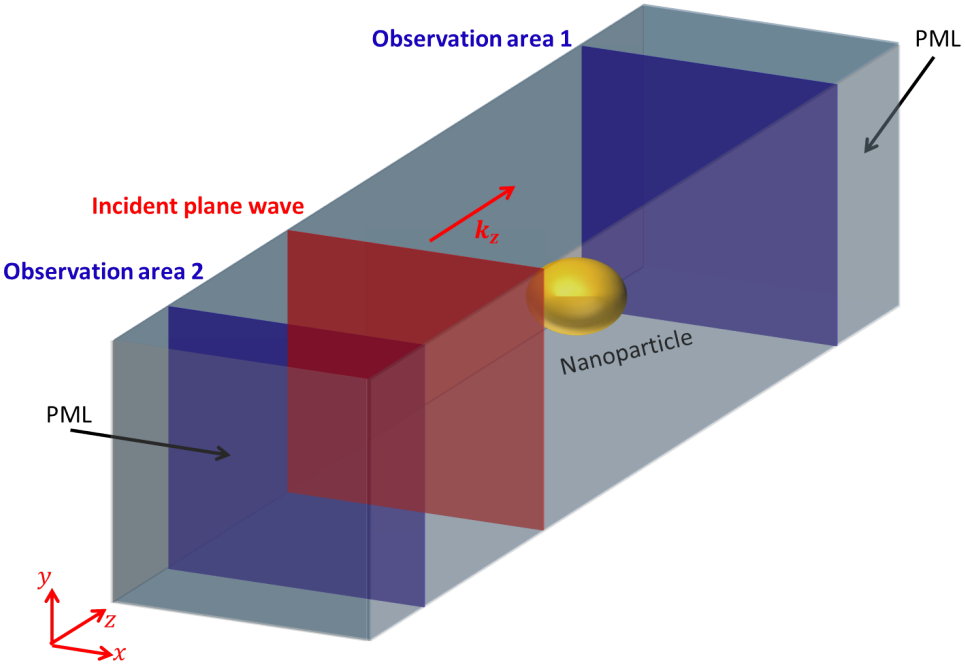

Figure 3–3: Schematic for the simulation domain used in OptiFDTD to calculate reflection and transmission efficiencies of periodic gold nanoparticles. Periodic boundary conditions were enforced along the x and y direction boundaries of the simulation domain, whereas PML boundary conditions were enforced along the boundaries in z direction.

The extinction efficiency is estimated as $Q_{ext} \sim (1-T)/max(1-T)$, where T is the calculated transmission efficiency, $T = (P_{trans}/P_{inc}$, where P_{trans} and P_{inc} are the transmitted and incident power, respectively. The scattering efficiency Q_{scat} was then calculated as $Q_{scat} \sim R/max(1-T)$, where R is the reflection efficiency, calculated at the reflection port in optiFDTD as $R = P_{ref}/P_{inc}$, where P_{ref} is the reflected power, received at the reflection port, which is placed in the far field region. The absorption efficiency Q_{abs} can then be estimated as $Q_{abs} = Q_{ext} - Q_{scat}$. Fig. 3–4 compares the FDTD results to those obtained from the FEM, Mie, and optical theorem. The FDTD revealed wide resonance curves at the same resonance wavelength location obtained by the other methods. The cubic mesh used in FDTD method is responsible for broadening the curves (staircase effect along the curved structures). The tetrahedral mesh, employed in the FEM, mitigates for this effect and improves the results as shown in Fig.3–4. However, the fabricated structures themselves yield broad resonance curves due to their surface roughness (effect of fabrication imperfections).

Mie theory is used here mainly to validate the FEM and FDTD modeling. The FDTD and FEM methods are advantageous in modeling more complex nanostructures, and they will be used in the remainder of the thesis.

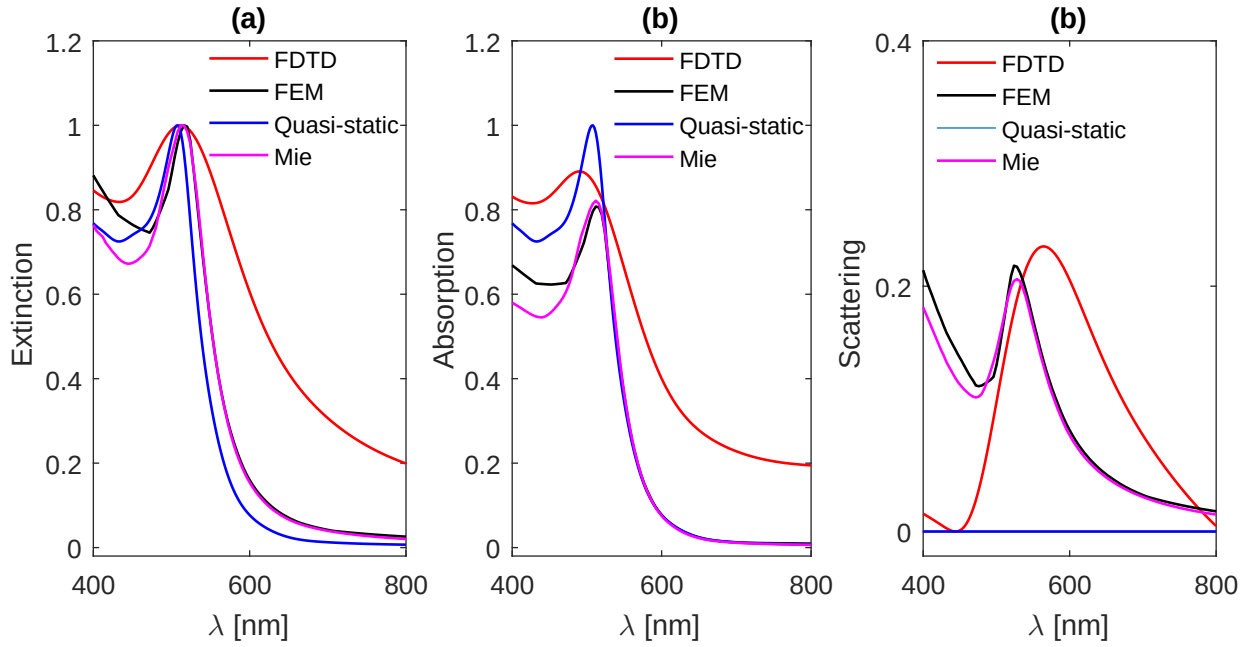

Figure 3–4: (a) Extinction, (b) absorption and (c) scattering efficiencies, associated with a 60 nm–radius gold sphere, calculated by different methods in order to validate their accuracy based on Mie theory.

3.2 Gold nanotube structures

Nanotube structures support a tunable LSPR mode, and exhibit a high sensitivity (580 nm/RIU). This section investigates their plasmonic properties based on numerical and experimental to the fabricated nanotube structures, investigating the reproducibility of their measured extinction spectra and their close agreement with the simulated counterparts. The structures were fabricated using the side-wall lithography method [121], characterized by the SEM and NSOM microscopy, and measured using the Cary 5000 spectrometer. The sensing results will be discussed in chapter 4, where the projection method is introduced to improve the signal to noise ratio.

The side-wall lithography method was used to imprint a uniform array of gold nanotubes

over a large–scale Cyclic Olefin Polymer (COP) substrate (1 cm^2), as shown in Fig. 3–5. Appendix (B) provides details about the fabrication process.

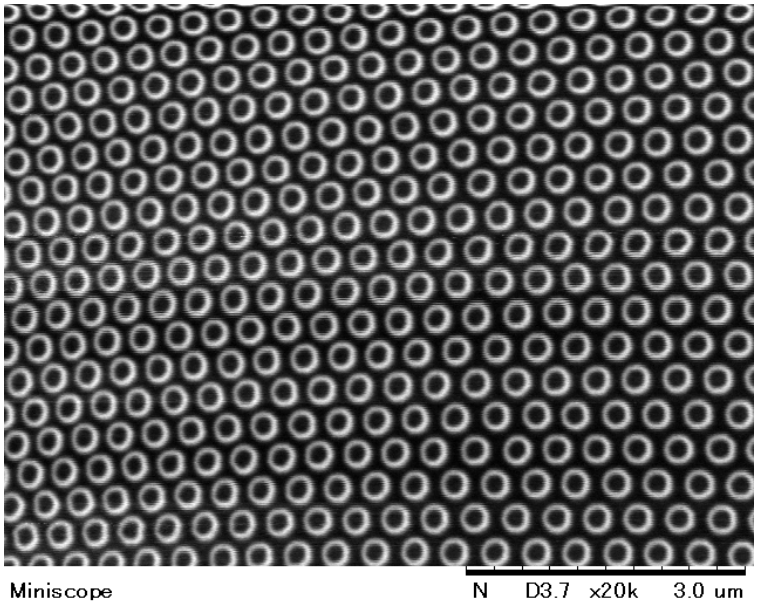

Figure 3–5: SEM image of the fabricated nanotubes. The inner diameter, height and the pitch are 200 nm, 90 nm, and 400 nm, respectively.

The topography and NSOM images were obtained using alpha300 imaging system from WITec. Transmission mode was chosen with a green laser source, and a NSOM probe with an aprture of 80 nm in diameter. The distance between the NSOM probe and the sample is controlled by a feedback based on the resonance frequency of the NSOM probe (cantilever resonance frequency), at which it oscillates. Since the resonant frequency oscillates with the largest signal amplitude, changed distance (between the probe and the surface of the sample) decrease the amplitude, and consequently shift the frequency. The reduced signal amplitude is used with a feedback system to adjust the distance between the NSOM probe and the surface of the sample. Simultaneously, the changes in the amplitude signal is employed to obtain the topography of the sample in a similar manner as the AFM [122]. The NSOM results, displaying both the surface topography and the near field characteristics, are shown in Fig. 3–6. Despite the mismatch between the LSPR and the operating wavelength of the laser source (570 nm), The NSOM results show regions of high EM fields (dark spots). This can be due to the wide extinction curve, associated with the nanotubes. However, the

wide curve degrades the FoM of the nanotubes as sensors. This is considered as the main disadvantage of the nanotube structures. Chapter 4 will present the projection method to improve the SNR for these structures.

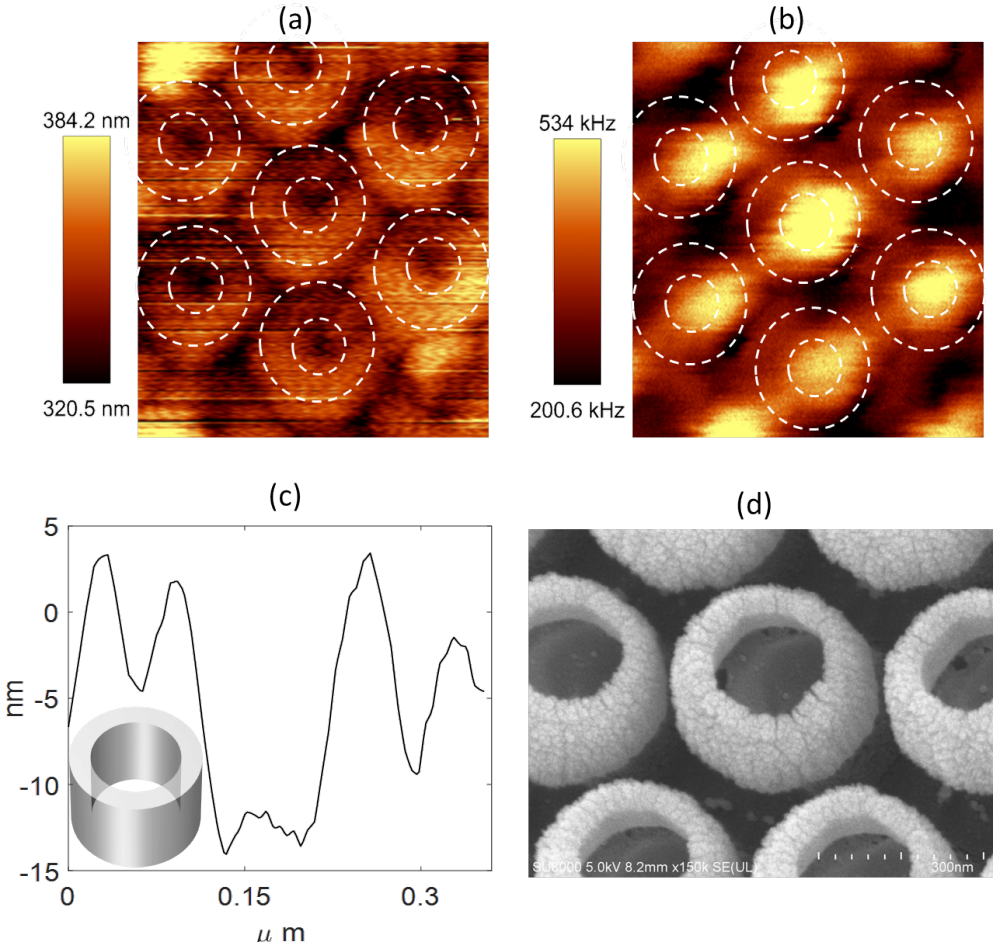

Figure 3–6: (a) Topography of the fabricated nanotube structures. (b) NSOM image, showing the near field behaviour of the fabricated nanotube structures. The image is obtained based on the cantilever resonance frequency of the NSOM probe, indicating the transmitted intensity through its aperture and collected by the objective lens beneath the sample. The NSOM detector provides a feedback to tune the resonance frequency with respect to the transmitted light. The nanotubes support LSPR at 1100 nm, hence the EM field is not high at the operating wavelength of the laser source, 570 nm. The bright spots denote the light transmission through the sample, whereas the dark spots indicate the absorption and scattering of the light beam by the nanotubes. (c) A diagonal line scan from the topographic image in (a), showing the walls of a nanotube and the pitch between them. (d) SEM image of the fabricated structures.

The nanotubes support a dipole–like resonance as shown in Fig. 3–7, and yield a resonance wavelength at 1250 nm, resulting in a higher sensitivity, when compared to nanostructures in the visible region. However, the FoM associated with the structures remains low. This is attributed to the lossy nature of gold, as discussed in Chapter 2. The measured extinction curve agrees well with the simulated counterpart, as shown in Fig. 3–7.

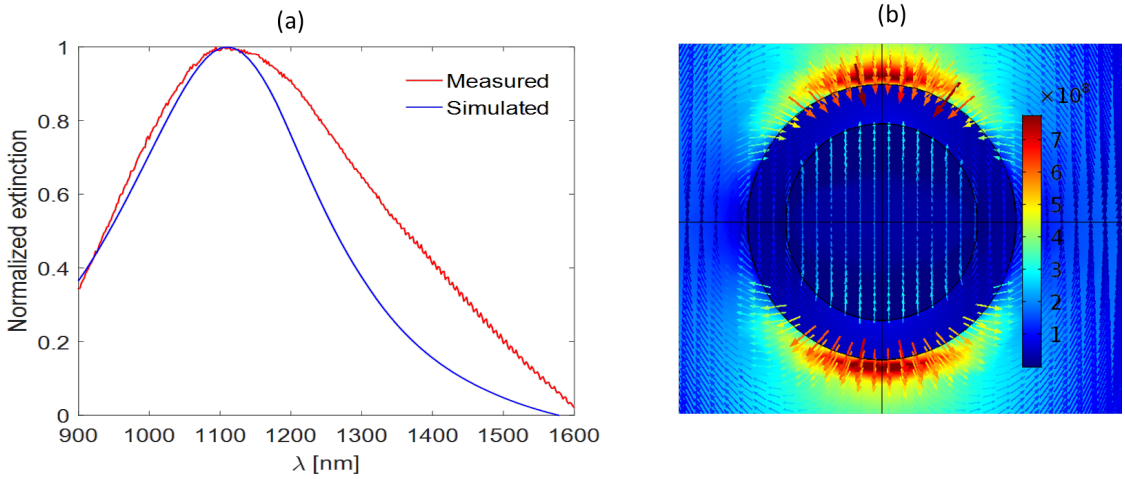

Figure 3–7: (a) Measured versus simulated normalized extinction efficiency for nanotube structures. (b) A dipole-like EM field pattern driven by a linearly polarized incident plane wave at the resonant wavelength (1100 nm). COMSOL Multiphysics was used to obtain the local electric field distribution.

Comparing the measured and simulated transmission efficiency curves reveals that the side-wall lithography method provides not only cost-effective means in fabricating nanostructures, but also precise and high throughput capabilities.

3.3 Multiple-resonance nanostructures

This section presents a comprehensive study to the multiple-resonance nanostructures fabricated by the side-wall lithography method. The FEM was used to understand the origin of the modes, and to calculate the optical cross sections. The section also provides the experimental results for the fabricated nanostructures and compares them with the simulated counterparts.

3.3.1 Nanocrescent structures

Due to their shape anisotropy, metallic nanocrescent structures can yeild multiple resonances, and the number of modes is dependent on the polarization of the incident plane wave [123]. Herein, the extinction curves were measured for both TE and TM polarizations. The experiments were repeated for 5 samples to investigate the reproducibility of the results.

This thesis will employ the multiple resonance characteristc in estimating the adlayer thickness and bulk RI changes [Chapter 6]. The advantage of such sensing platform is that the EM decay length depends on the resonance wavelength, as the sensor probe depth is different for each mode. This can be used in distinguishing the effects of adsorbed analyte from those due to bulk RI change. U-shaped nanostructures reported low sensitivities [117], and the fabrication of such structures typically requires expensive and time consuming electron beam lithography. Here, the side-wall lithography method is used to fabricate the nanostructures on a large-scale substrate (1 cm^2). The FEM was used to calculate the optical cross sections and the EM field distributions associated with each resonance. The extinction cross section was also calculated using the optical theorem and compared to the FEM results, as shown in Fig. 3–8, demonstrating that the extinction cross sections for the three resonances are dominated by scattering rather than absorption.

Fig. 3–8 (a) shows a single LSPR mode associated with nanocrescents at 1100 nm, when excited by a plane wave polarized along x-axis (the axis of the shape symmetry of the nanocrescent). However, a dual-resonance mode is supported when the structure is excited by a plane wave polarized along y-axis, as shown in Fig. 3–8 (b). This mode is originated from the shape asymmetry of the nanocrescent along the y-axis and the resonance wavelengths are located at 800 nm and 1450 nm.

To investigate the effect of the wedge angle of the crescents and the etching depth during the fabrication process, FEM modeling was performed considering a hexagonal lattice and periodic boundary conditions. Fig. 3–9 shows a schematic for the simulation domain, illustrating the tilt angle and etching depth, the first two resonances can be excited with a plane wave polarized along x-axis and the third resonance can be excited with a plane wave polarized along y-axis. The results for the first and second resonances (800 nm and 1450

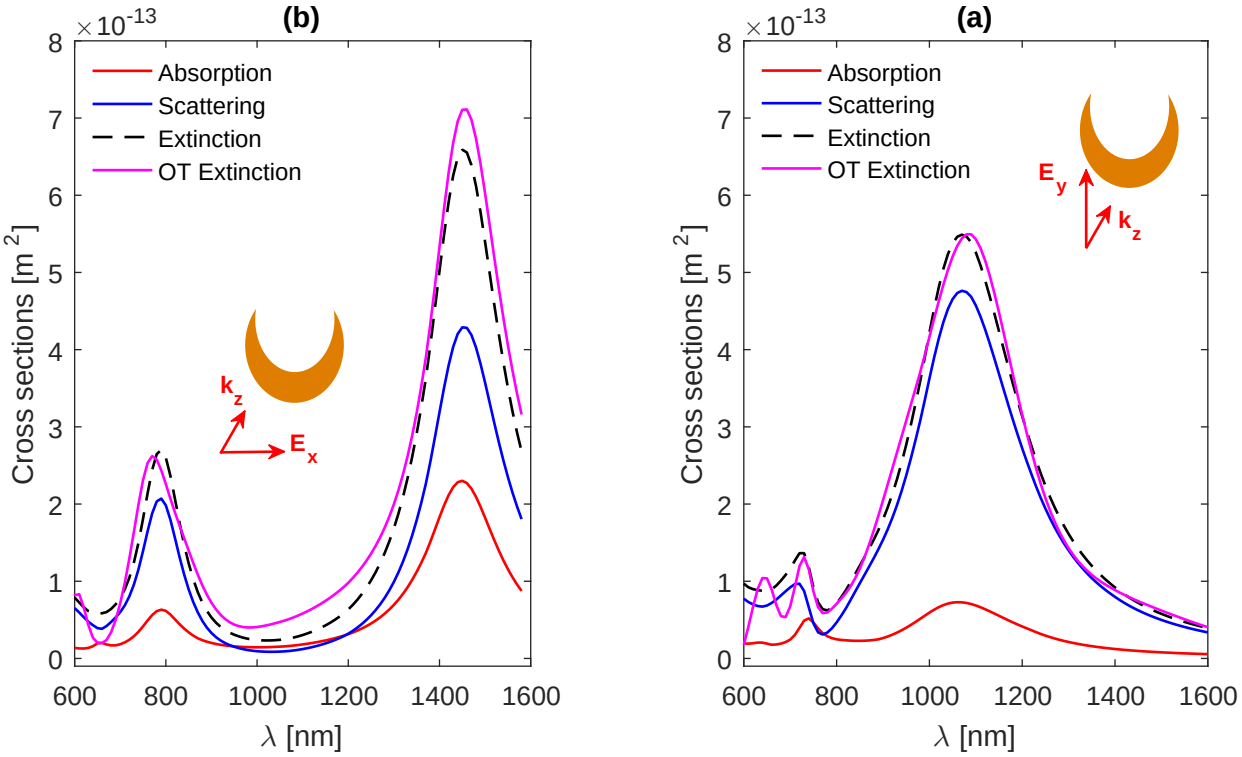

Figure 3–8: Calculated absorption, scattering and extinction cross sections for a single nanocrescent, excited by a normal incident plane wave polarized (a) along the x-axis, and (b) along the y-axis. The FEM simulation domain is surrounded by a PML of 5 absorbing layers. The results are compared to those based on the optical theorem (OT) are also shown.

nm) demonstrate that increasing the tilt angle or the etching depth increases the resonance wavelengths, as shown in Fig. 3–10 (a) and (b). In the case of the y-polarized plane wave, a single resonance is obtained due to the symmetry of the structure along the y-axis. However, as the wedge angle and etching depth increase, another mode can be excited in the lower part of the spectrum (800 nm), as shown in Fig. 3–10 (c) and (d). However, this mode features a broad extinction curve and weak efficiency, and hence it can be ignored when compared to the main mode at (1100 nm). A dipole-like mode is excited if the polarization is along y-axis due to the shape symmetry, as shown in Fig. 3–11 (c). On the other hand, an incident wave polarized along x-axis can excite a dual-resonance mode with a distinct field profile at each resonance wavelength. This suggests that the bulk RI and adlayer sensitivities can be spatially distinguished as the EM decay length is dependent on the resonance wavelength.

The side-wall lithography method was used to fabricate the nanocrescents [Appendix C],

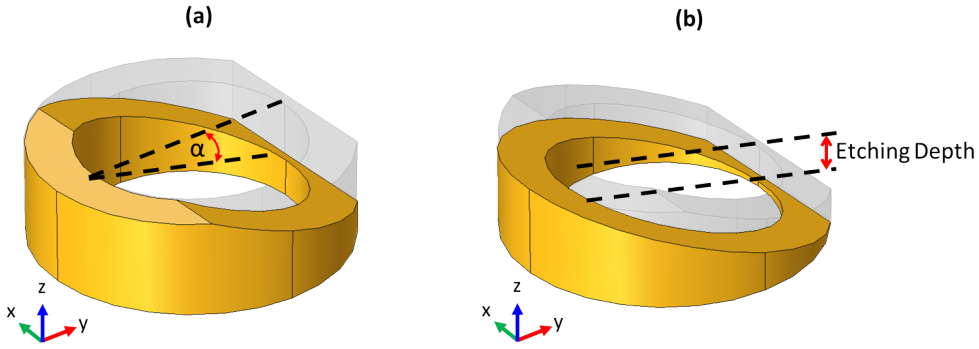

Figure 3–9: Illustration of (a) the wedge angle, and (b) etching depth that were used in the FEM model to study their effect on the extinction curves.

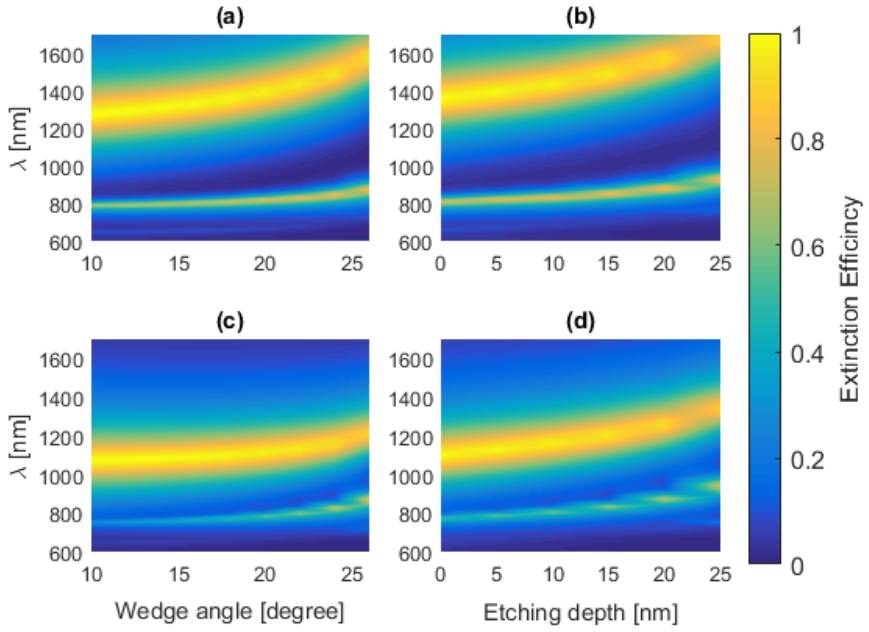

Figure 3–10: Effect of wedge angle and etching depth on (a, b) the first and second resonance wavelengths (800 nm, and 1450 nm), (c, d) the third resonance (1100 nm).

and the absorption spectra were measured by the Cary 5000 spectrometer. The fabricated nanocrescent structures were characterized by NSOM imaging to investigate their surface topography and near field profile, as shown in Fig. 3–12. The surface topography image reveals an average height of 90 nm for the nanocrescents. However, due to the wedges, the thickness of the crescent is not uniform. This was taken into account in the FEM calculation. Fig. 3–12 (b) shows the near field profile as the transmitted light was captured by a NSOM beneath the substrate. The bright spots indicate no interaction between the light and the

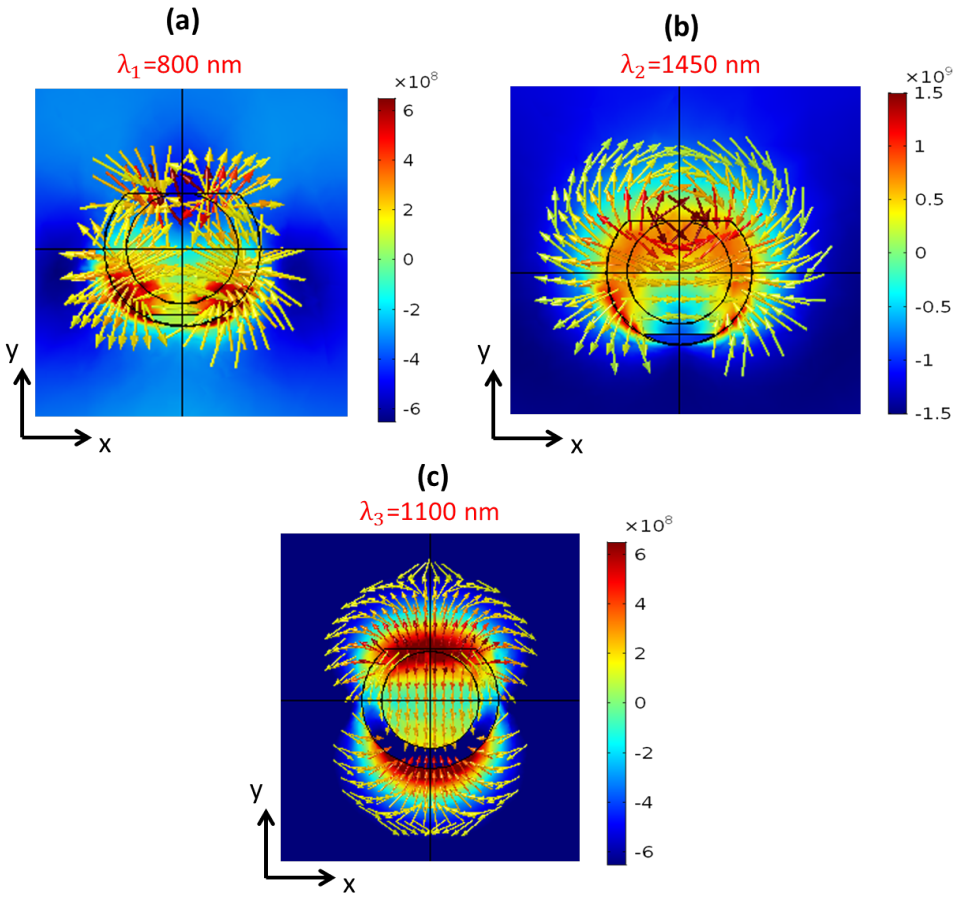

Figure 3–11: Local electric field distributions (V/m), associated with the nanocrescent structure, driven by an incident plane wave polarized in (a, b) x–axis and (c) y–axis.

nanotubes, whereas the dark spots represent the location of the field associated with the nanostructures. The near field shown in the graph is associated with the lowest mode, since its resonance wavelength is closer to the operating wavelength of the laser source used with NSOM. Fig. 3–12 (c) overlaps the NSOM and topography images in a 3-D plot, indicating the correlation between them.

More details about the structures were obtained by SEM, as shown in Fig. 3–13. The wedge is due to the angled etching employed by the side-wall lithography method. This required more investigation about the results reproducibility for the extinction curves. Five sample were measured using the Cary 5000 spectrometer, and the average of each resonance location and its standard deviation were calculated to provide an estimate of the error due

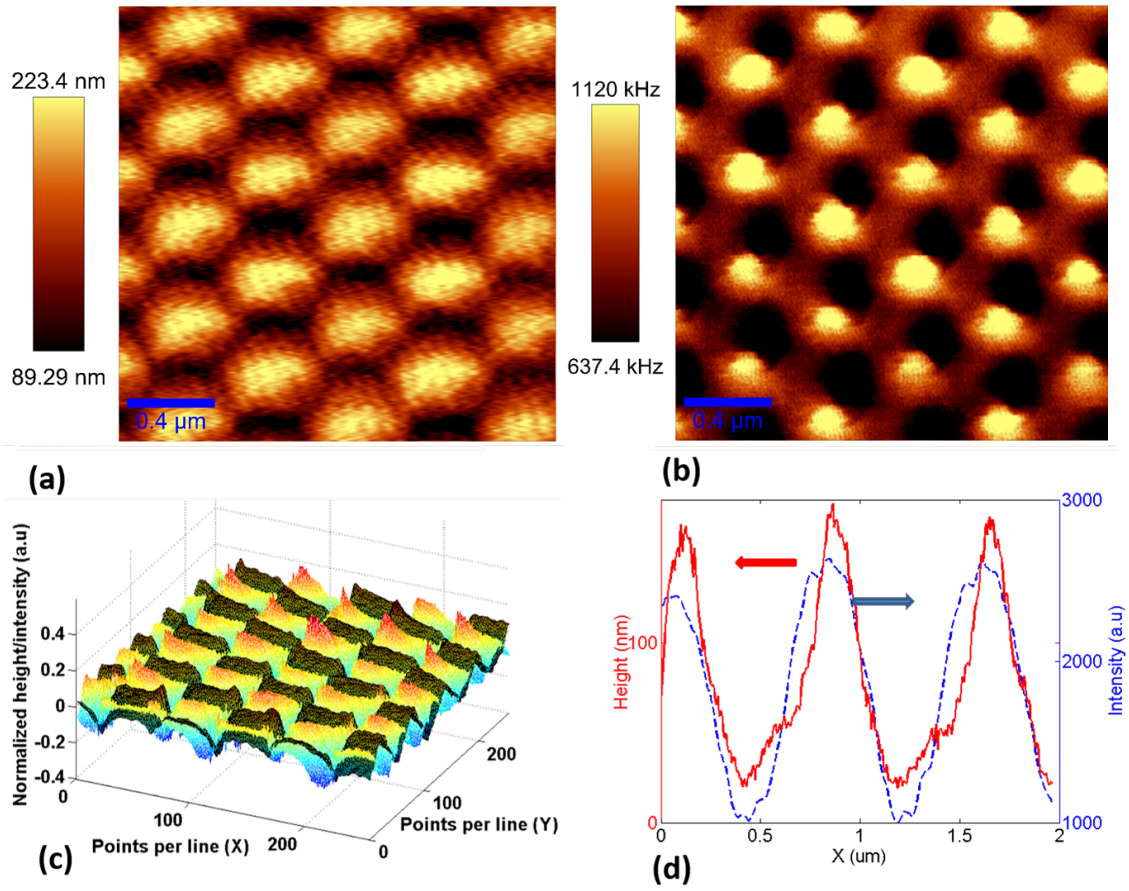

Figure 3–12: (a) Topography and (b) NSOM images for the fabricated nanocrescent structures on a COP substrate. The intensity is modulated in terms of the cantilever resonance frequency (KHz), which is changed relative to the collected signal amplitude, and thus the dimensions are normalized to their maximum values to obtain (c) a 3D visualization for the AFM and NSOM data (Matlab was used to overlap both images), the bright (red) spots represent the maximum transmitted light, and the blue part indicates a decreased intensity due to absorption or scattering of light by the nanocrescent structures. (d) Surface topography and transmitted light, scanned a long a line crossing the nanocrescents.

to the fabrication imperfections. For clarity, only two measured extinction curves are shown in Fig. 3–14 (a) and (b), but the standard deviation was based on five measured curves for each resonance.

It can be observed that the peak at the second and third resonances (1100 nm and 1450 nm) are broadened and weakened while the resonance locations are unchanged when compared to the simulated results. This could be due to the thin metal part, connecting the tips of the crescents, where the electrons are excited by these modes, as shown in Fig. 3–11

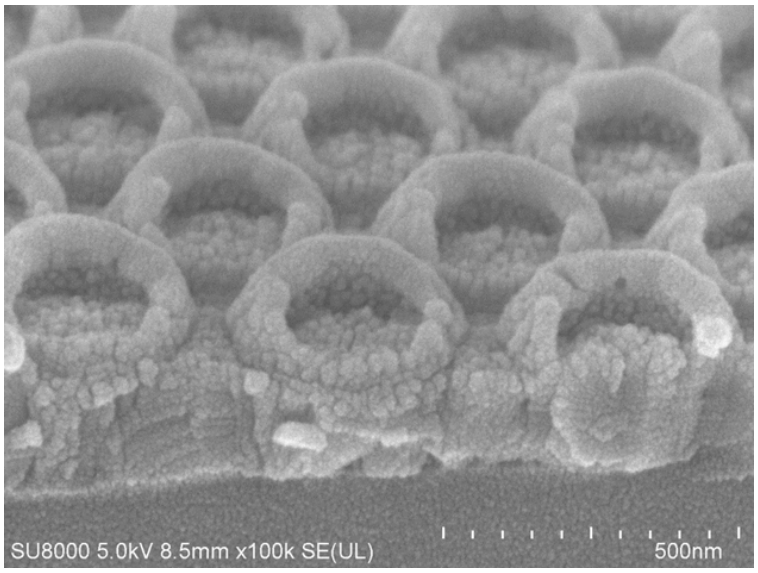

Figure 3–13: SEM image of nanocrescent structures on a COP substrate, fabricated by sidewall lithography method. The overall structure is arrayed on a COP substrate of 1 cm^2 surface area and 150 μm thickness.

(b) and (c). This effect can alter the dielectric function of gold due to size dependent electron scattering [124]. It is more pronounced when the metal size is small relative to the electron mean free path, as explained in Chapter 2 [Eq. (2.15)]. A similar trend has been previously observed for gold nanocups [125]. The broadening in the resonance curve can reduce the accuracy of the dynamic-baseline centroid method, as the resonance wavelength is exracted from a wide wavelength interval. The peak tracking method [99] and the dynamic-baseline centroid method [101] are employed here to extract the resonance wavelength. The calculated mean and the standard deviations of the resonance wavelengths are represented by the PDF distributions, shown in Fig. 3–14 (c), (d) and (e). The dual-resonance mode is less affected by fabrication imperfections as shown in Fig. 3–14 (c) and (d), because their extinction curves are stable over the five tested samples. Due to the broad extinction curves associated with the third mode (1100 nm), the dynamic-baseline centroid method yielded inaccurate resonance wavelength as shown in Fig. 3–14 (e). However, this can be improved by using a narrower wavelength range in determining the resonance wavelength, but the precision will be reduced (approaching the results obtained by the peak-tracking method).

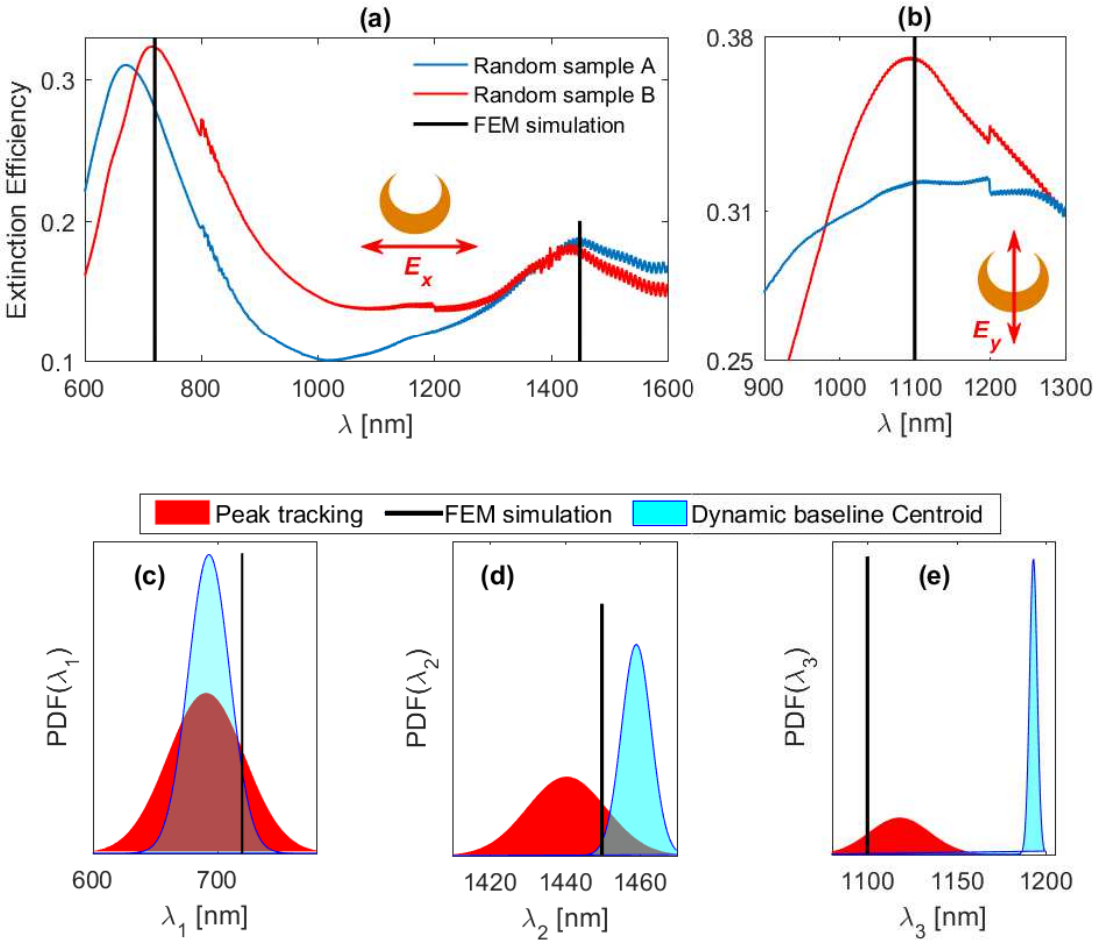

Figure 3–14: Measured extinction efficiency for two samples of the fabricated nanocrescents excited by a normal incident EM wave polarized (a) horizontally, and (b) vertically. The PDF distribution of (c) $PDF(\lambda_1)$ (d) $PDF(\lambda_2)$ and (e) $PDF(\lambda_3)$ based on the dip finding and dynamic baseline centroid methods, showing the uncertainty in each resonance wavelength over multiple measurements for five randomly selected fabricated samples. The simulated resonance wavelengths are plotted to evaluate the accuracy of the dip-finding and dynamic baseline centroid methods.

3.3.2 Nanorods

Gold nanorods possess attractive plasmonic characteristics, making them good candidates for sensing applications. They support transverse and longitudinal modes. The longitudinal mode can be tuned over a wide wavelength range. This characterisitc has been useful multiplexed sensing applications [91–93], and self-referencing LSPR sensing application, where the longitudinal and transverse modes were utilized in differentiating between bulk and surface effects in during sensing experiments [116]. In this work a three-resonance nanorod structures will be adopted to estimate the adlayer and RI changes in surface-binding sensing experiments.

This section highlights the plasmonic properties of gold nanorods, including the absorption, scattering and extinction cross sections, and the electromagnetic field distributions supported by the transverse and longitudinal modes. COMSOL Multiphysics (FEM based package) is used here in the calculations.

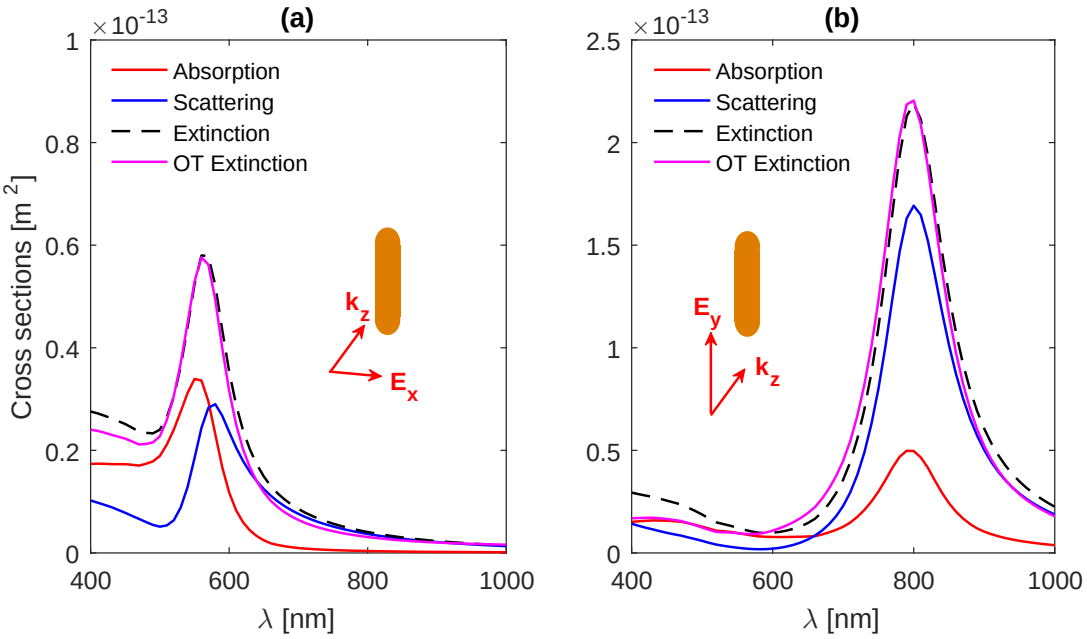

Figure 3–15: Optical cross sections of gold nanorod structures in the case of (a) the transverse mode, and (b) longitudinal mode. The nanorod major and minor axes (in x-y plane, see the inset) are 150 nm and 70 nm, respectively, the thickness is 30 nm (along z-axis in the inset).

The transverse mode can be excited by an incident light wave polarized along the short

axis of the nanorods. This resonance is located in the blue part of the visible spectrum, and absorption contributes more than scattering to the extinction cross section. The longitudinal mode results from the excitation of the electrons along the major axis of the nanorods by a vertically-polarized incident light wave. In this case, the resonance wavelength is red-shifted and scattering becomes the main contributor to the total extinction cross section. The resonance wavelengths and the optical cross sections associated with them are shown in Fig. 3–15 (a) and (b). The EM field distributions associated with the transverse and longitudinal modes are shown in Fig. 3–16.

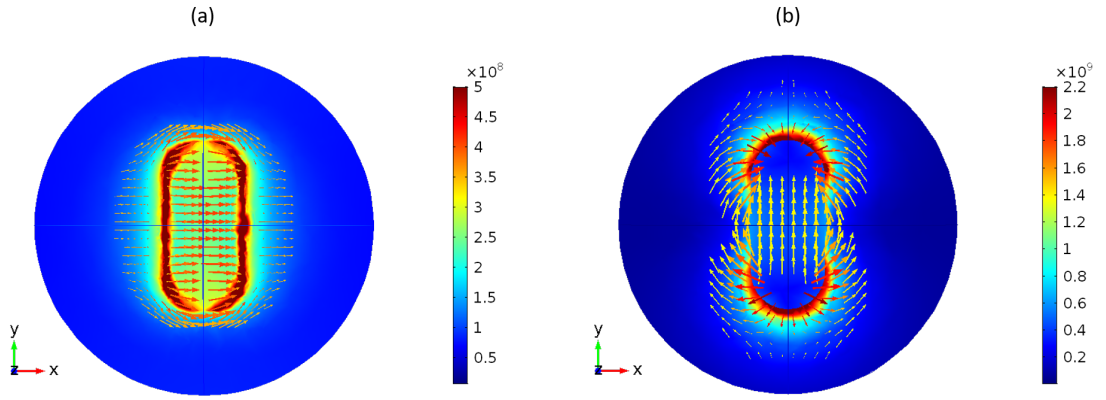

Figure 3–16: The electric field distribution (V/m) associated with gold nanorod structure, supporting LSPR in the case of (a) transverse mode, and (b) longitudinal mode.

The amplitude of the extinction also depends on the volume of the nanorods that is determined by the effective radius (the radius of a sphere of equivalent volume to the nanorods) [126]. Based on the quasistatic approximation, the calculated values for the LSPR wavelength supported by gold nanorods can be obtained as follows

$$\lambda_r = \lambda_p \sqrt{\varepsilon_\infty + n_B^2 (\frac{1}{\rho} - 1)} \tag{3.9}$$

where $\lambda_p = 2\,\pi\, c_0/\omega_p$, is the plasma wavelength for gold $\sim$ 136 nm, and c_0 is the speed of light. The shape factor for a nanorod can be determined with respect to its aspect ratio

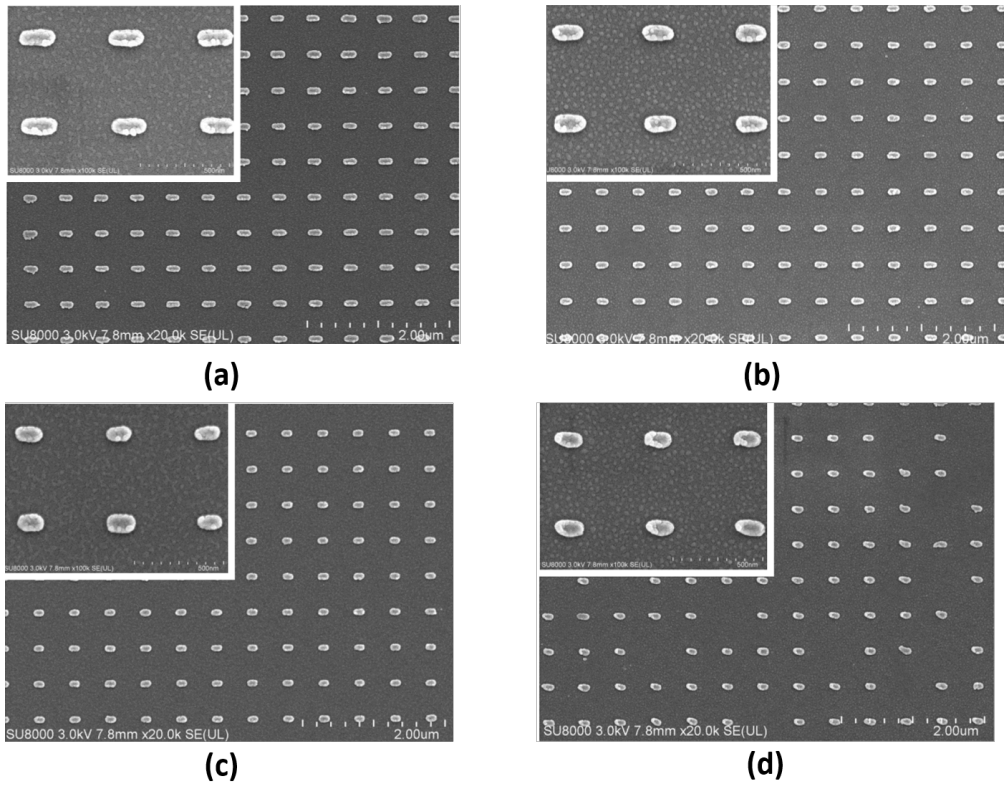

Figure 3–17: SEM images of nanorod structures fabricated by side–wall lithography method on a glass substrate. The rods have the same width, 70 nm, and the length varies as follows: (a) 200 nm, (b) 170 nm, (c) 150 nm, and (d) 120 nm

(AR) as follows [Eq. (2.10)]

$$\rho = \frac{1}{AR^2 - 1}\left[\frac{AR}{2\sqrt{AR^2-1}} ln\Big(\frac{AR + \sqrt{AR^2-1}}{AR - \sqrt{AR^2-1}}\Big) - 1\right] \tag{3.10}$$

The sensitivity of the nanorod structures was measured as the ratio of the shift in resonance wavelength to the RI change. The RI change corresponds to various concentrations of the ethanol solutions that were introduced to the nanorods. The sensitivity values were compared to the calculated counterparts. The results are compared to the sensitivity of small nanorods (compared to the wavelength), which can be calculated using Eq. (2.40) based on the quasi-static approximation. For a fair comparison between the two regimes, the aspect ratio of the small nanorods is kept the same as that for the fabricated nanorods. The results are given in Table 3.1.

Table 3.1: Calculated versus measured resonance wavelength and sensitivity for nanorods of various aspect ratios.

AR	ρ		Quasi-static[a]	FEM	Measured values
2	0.3144	$\lambda_1\,(nm)$	470.7	625	626
		$S_{B_1}\,(nm/RIU)$	93	212.92	268.15
2.5	0.2217	$\lambda_2\,(nm)$	496.2	700	684.3
		$S_{B_2}\,(nm/RIU)$	138	303.36	331.06
3	0.1674	$\lambda_3\,(nm)$	523	860	905
		$S_{B_3}\,(nm/RIU$	182.7	316.28	382.37

[a] Calculations for nanorods with equivalent AR's, but their sizes satisfy the quasi-static approximation (major axis$< 100\,nm$).

The stability of each resonance wavelength was investigated based on the measured extinction curves for five fabricated samples. For clarity, only two measured curves are shown in Fig. 3–18 (a), (b) and (c). The mean and standard deviation of the measured resonance wavelengths were determined and used to produce a PDF distribution for each resonance wavelength, as shown in Fig. 3–18 (d), (e) and (f). The resonance wavelengths were determined by the peak-tracking method and dynamic-baseline centroid method. The latter provided more stable results, as the averaged error was 4.33 nm and 5.9 nm based on the dynamic-baseline centroid and peak-tracking method, respectively. The nanorods provided more stable and repeatable measured resonance wavelengths, when compared to the nanocrescent structures. Their multiple-resonance characteristic will be employed for a quantitative study for binding events and self-referenced LSPR sensing in Chapter 5.

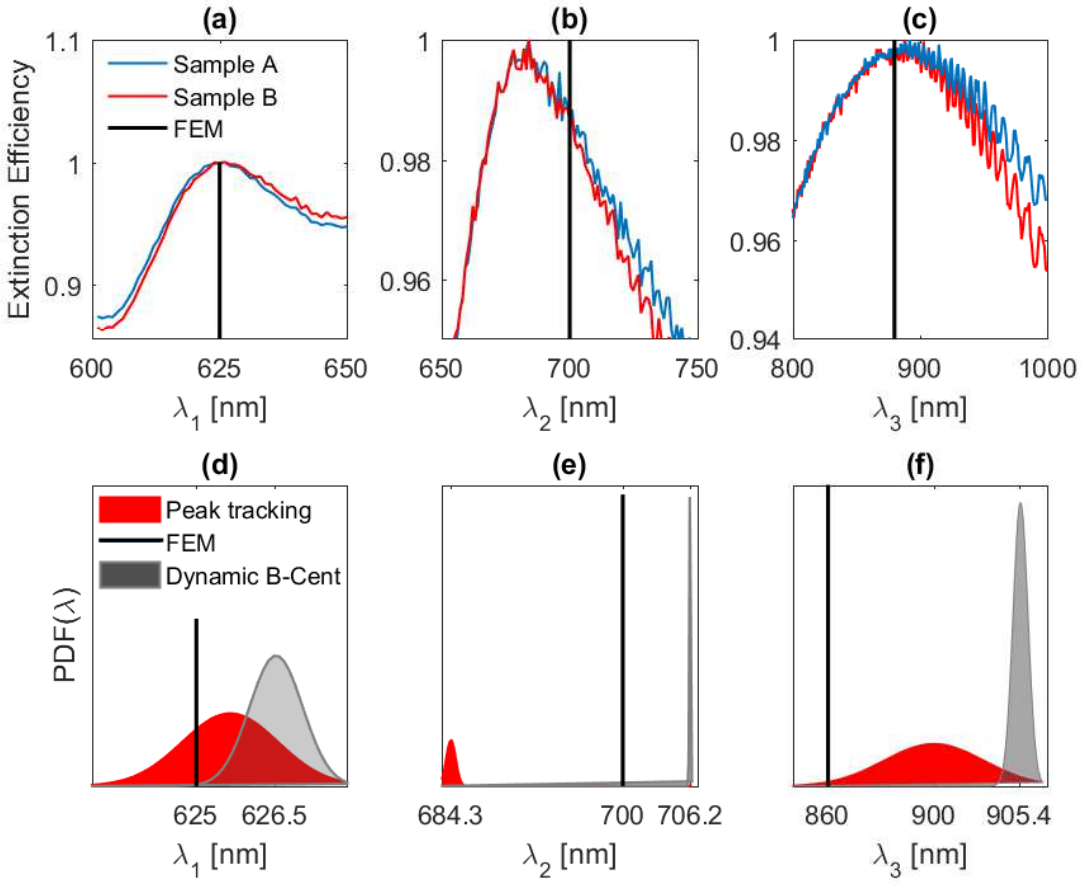

Figure 3–18: Measured extinction efficiency curves for the fabricated nanorod structures at (a) 625 nm, (b) 700 nm, and (c) 890 nm. The PDF distributions, based on five randomly selected samples from the fabricated structures, showing the mean and the standard deviation of (d) λ_1, (e) λ_2 and (f) λ_3 determined by the peak tracking and dynamic baseline centroid methods. The results based on these methods are compared to the simulated counterparts.

3.4 Summary

This chapter compared among various analytical and numerical methods used in light scattering by nanoparticles. The results, obtained from the FDTD and FEM models were validated based on the exact solution for optical cross sections of metal nanoparticles. Both the FDTD and FEM methods provided accurate results in determining the resonance wavelength. The FDTD yielded a wider curves due to the use of the cubic mesh in discretizing the simulation domain and the Drude-Lorentz model in calculating the dielectric permittivity for gold. The FEM is considered to be computationally faster than the FDTD for calculating the EM field at single or few wavelength steps. As the calculation is repeated for a wider wavelength range, the processing time increases dramatically in the case of the FEM (the simulation is repeated for each step). The FDTD provides the solution for a pulse in time domain, and uses Fourier transform to obtain the full spectrum solution in frequency domain.

The chapter also investigated the fabricated nanostructures based on the surface characterization (SEM and NSOM imaging) and measured extinction curves. The chapter provided simulated results for each nanostructure including the optical cross sections and near field distributions. Lastly, the fabricated structures were investigated for resonance wavelength reproducibility based on the extinction measurement for many fabricated samples.

4

Projection Method for Improving Signal to Noise Ratio of Localized Surface Plasmon Resonance Biosensing

This chapter presents a simple and accurate method (the projection method) to improve the signal to noise ratio of localized surface plasmon resonance (LSPR). The finite difference time domain method is used to simulate the structures and generate a reference matrix for the method. The results are validated against experimental data and the proposed method is compared against several other methods [section 2.7]. The projection method is also applied to biotin-streptavidin binding experimental data and determine the limit of detection (LoD). The method improves the signal to noise ratio (SNR) by one order of magnitude, and hence decreases the limit of detection when compared to the direct measurement of the

transmission-dip. The projection method outperforms the established methods in terms of accuracy and achieves the best combination of signal to noise ratio and limit of detection.

4.1 Projection method

The double projection method, on which the proposed method is based, was introduced to improve the signal to noise ratio of a spectro-angular SPR sensor [106]. Its principle of operation is briefly explained here; Spectro-angular reflectance maps for a set of different refractive indices were numerically calculated in advance. Singular value decomposition was then used to extract a basis set from these 2-D images. Two projections were performed against the basis set: i) the normalized simulated images were projected against the basis matrix yielding a weight matrix; ii) the measured spectro-angular images (arising from samples with unknown refractive indices) were projected against the basis set to form a set of weight vectors (the name of the method was given based on the second projection process). The weight vectors were then projected against the simulated weight matrix yielding a solution vector. The solution vector was then interpolated to improve precision of refractive index estimate. The method achieved a 3-order of magnitude improvement in signal to noise ratio (in numerical simulation) [106]. However, the experimental complexity of the spectro-angular interrogation SPR system may be an issue if a simple platform is desired.

The single projection method, proposed here, simplifies the double projection method by projecting the normalized measured data (normalized vectors) onto a simulated reference set and interpolating the solution vector to estimate unknown refractive indices of the measurands. The remainder of this section provides more details about the new approach.

The finite difference time domain was used to calculate the transmission spectra of the nanotube structures: we used OptiFDTD commercial software [61] to model the nanostructures and optimize their dimensions to match the performance of the fabricated structures. The simulation was then repeated to obtain a set of transmission spectra spanning the refractive index (RI) range ($n_{min} - n_{max}$) with 1×10^{-3} resolution. The simulation vectors representing the simulated spectra were normalized by dividing each transmission vector ($\mathbf{T}$)

by its Euclidean norm, and concatenating them to build the reference matrix ($\mathbf{M}$) as follows

$$\mathbf{T_n} = \frac{\mathbf{T}}{||\mathbf{T}||} \tag{4.1}$$

$$\mathbf{M} = \begin{bmatrix} T_{n11} & T_{n12} & & T_{n1j} \\ T_{n21} & \ddots & \ddots & T_{n2j} \\ & \ddots & \ddots & \\ T_{ni1} & T_{ni2} & & T_{nij} \end{bmatrix} \tag{4.2}$$

where the rows (i) span the RI range of interest, and the columns (j) correspond to the wavelength data points (We used 750 data points, and 0.2 nm wavelength resolution) as illustrated in Fig. 4–1.

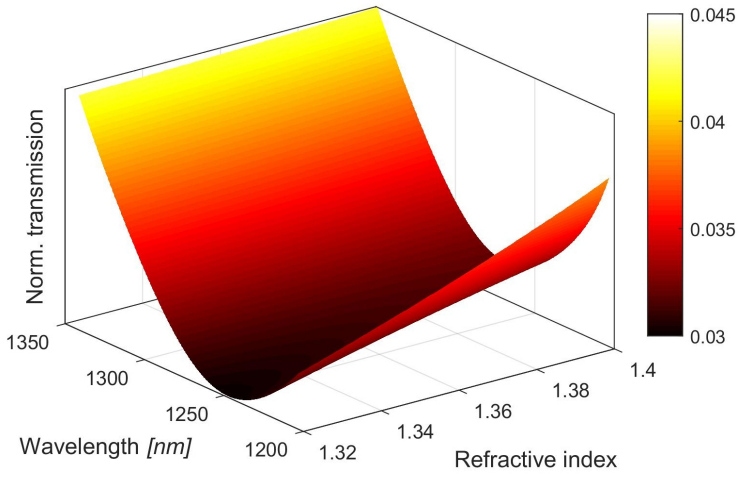

Figure 4–1: A 3-D representation of the projection reference matrix (obtained from the FDTD simulation) for a set of refractive indices spanning the RI range (1.318–1.4), Simulation used 750 wavelength data points (0.2 nm resolution).

To estimate the refractive index of an unknown sample, the measured transmission spectrum from the sample is represented by a vector ($\mathbf{v}$) that is divided by its norm to reduce the effect of intensity fluctuations.

$$\mathbf{v_n} = \frac{\mathbf{v}}{||\mathbf{v}||} \tag{4.3}$$

Now the normalized vector ($\mathbf{v_n}$) for the unknown RI is projected onto the reference matrix ($\mathbf{M}$) vector by vector to obtain the solution row vector ($\mathbf{s}$) whose elements provide the degree of similarity between the measured and the simulated spectra.

$$\mathbf{s} = \mathbf{M}.\mathbf{v_n} \tag{4.4}$$

The solution row vector, $\mathbf{s}$, can be interpolated over the RI range. This approach is illustrated in Fig. 4–2: Fig. 4–2 (a) shows two measured transmission curves (affected by high frequency interference) corresponding to two different bulk refractive indices. Fig. 4–2 (b) shows the solution row vectors calculated for each. Interpolating the curve improves the precision of the method, and the abscissa of the maximum provides the RI estimate. Therefore, each measured transmission curve (providing the resonance wavelength shift) was transformed into a smooth curve, extracting the refractive index of unknown solutions directly.

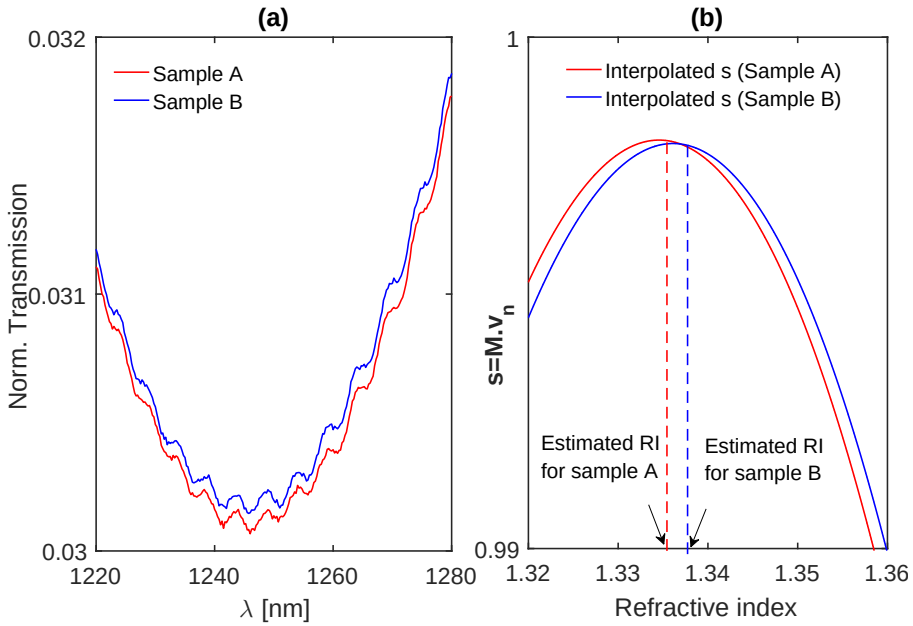

Figure 4–2: (a) Normalized transmission vectors for unknown samples (A and B): the curves are affected high frequency interferences (ripples) that complicate tracking the transmission dip and reduce the sensor accuracy. (b): Interpolated curves for the solution row vectors for unknown samples (A and B) revealing estimated refractive indices of 1.3346 and 1.3361, respectively: the entire measured curve in (a) was used here instead of using a single resonance wavelength as in the dip-finding method.

4.2 Methods

Commercial OptiFDTD design tool [61] was used to simulate the nanotube structures and optimize them to have their transmission curve match the measured counterpart. A single structure unit is used in the simulation, and periodic boundary conditions were forced to simulate the infinite number of nanotubes. The Drude Lorentz model was used for the gold material properties, and a value of 1.53 refractive index was used for the COP substrate. A Gaussian-modulated continuous wave was used to excite the nanostructures with a normal incidence. Numerical optimization has been performed to the simulated structure to match the simulated spectra with the measured counterparts. The simulation was repeated for the entire refractive index range. The sensitivity of the sensor can be calculated as the ratio of the resonance wavelength shift with respect to the refractive index change, the calculated

sensitivity was 582.9 nm/RIU.

Side-wall lithography technique [121] was used to fabricate the nanotube structures. The fabrication procedure is described in Appendix B. The fluidic channel was fabricated by using Polydimethylsiloxane (PDMS) replica molding method, described in Appendix C.

The functionalization process included the preparation (cleaning) of the sensing chip, incubation, and post-cleaning of the chip before any sensing experiments: the sensing surface was cleaned by isopropyl alcohol and deionized (DI) water, then plasma treated to remove any organic objects. The sensing chip was then incubated, for biotin labeling, in 10 mM phosphate buffer solution (pH 7.2) of 200 μM of Formula-(6-[biotinamido]hexyl)-3′(2′ -pyridyldithio)propionamide. The streptavidin solutions were prepared by dissolving streptavidin powder in a 50 mM Tris buffer (pH 8) [117].

4.3 Results and discussion

This section presents comparative results based on simulated results and bulk and surface binding sensing results.

4.3.1 Comparison to established methods

This section compares the projection method to the published signal processing methods, described in chapter 2, based on simulated results. The FDTD simulation was used to obtain transmission curves, corresponding to known changes in bulk RI. In order to determine the accuracy of the methods, I applied each method to the simulated data to estimate the RI change used in the simulation. To investigate the effect of noise on the accuracy of each method, I introduced a Gaussian noise to the simulated transmission curves, and used each signal processing method in estimating the RI change.

First, the accuracy of the projection method is determined with respect to the RI interval in the reference matrix as shown in Fig. 4–3 (a), the medium RI is changed by 1 $\times 10^{-5}$ and 5×10^{-5} in the simulation, and the corresponding transmission curves were projected against reference matrices of different RI step size. An accuracy of 10^{-7} RIU can be obtained using

a reference matrix with a 1×10^{-4} RI step size. A Gaussian noise was also introduced to the simulated transmission curves to investigate the stability of the method with respect to noise levels, as shown in Fig. 4–3 (b), the error in the estimated RI change based on a noisy transmission curve can be as low as 0.2%.

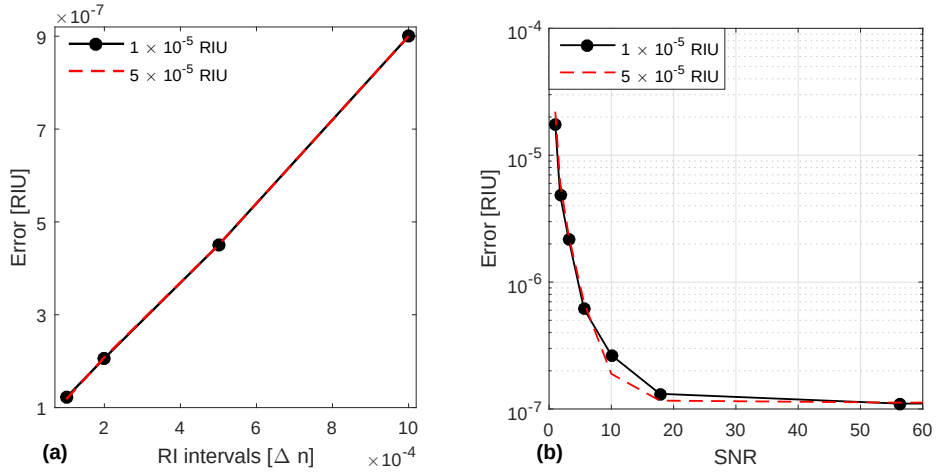

Figure 4–3: (a) Calculated error in the estimated RI change with respect to the RI interval in the reference set, (b) error in estimated RI change, calculated as the difference between the estimated RI changes and the ideal values (1×10^{-5} and 5×10^{-5}).

Now all the methods are applied — as described in section 2.7— to the same simulated noisy datain order to estimate the RI change. The reference set is used to obtain a calibration curve for each method, and the slope of each curve provides the sensitivity factor used in determining the RI change (known in this case to test the accuracy of each method).

After applying these methods on the simulated data to determine a RI shift of 5×10^{-5}, a Gaussian noise was added to the extinction curves and the effect was also investigated. As shown in Fig. 4–4, the projection method outperforms the established methods as the error is in the range of 1×10^{-7} that is one order of magnitude improvement to the dynamic-baseline centroid and NDIR methods, and two orders of magnitude improvement to the integrated response and fixed-boundary centroid methods, and three orders of magnitude improvement to the conventional dip-finding method.

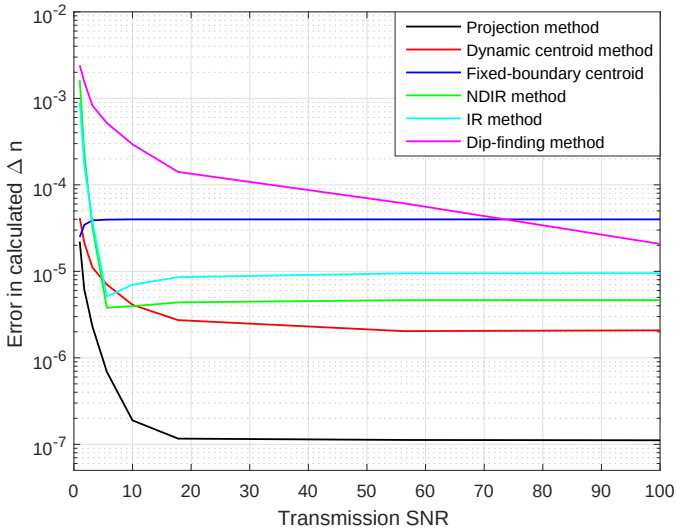

Figure 4–4: Calculated error with respect to the noise level added to the simulated transmission curves, the projection method is superior to the other methods in terms of accuracy ($1 \times 10^{-7} RIU$ error) and stability against noise as the error is as low as 5×10^{-6} (10% error) even with noisy transmission curves (SNR$\approx$ 3).

4.3.2 Bulk RI and surface binding sensing results

This section presents sensing results based on the projection method and provides a comparison to the published methods in terms of SNR improvement and computational complexity. Fig. 4–5 (a) shows the experimental set-up, and the inset illustrates the PDMS channel integration with the fabricated nanostructures, as the grooved part of the PDMS can be bonded to the sensing substrate, flushing the fluids through the in/outlets. Fig. 4–5 (b) shows SEM image of the fabricated nanotube structures, which are uniformly distributed on the COP substrate.

Multiple transmission spectra were obtained for ethanol solutions of different concentrations. The measured sensitivity, S, and the figure of merit, FoM, for the nanostructures are $\sim$ 582.9 nm/RIU, and 1.2 /RIU, respectively. The FoM was calculated as FoM=S/FWHM, where FWHM is the full width at half maximum of the measured transmission curve. The low figure of merit resulted in a significant uncertainty in determining the location of the resonance minimum when the dip finding method was used, as shown in Fig. 4–6 (left Y-axis). The projection method improved the results as the entire measured spectra were

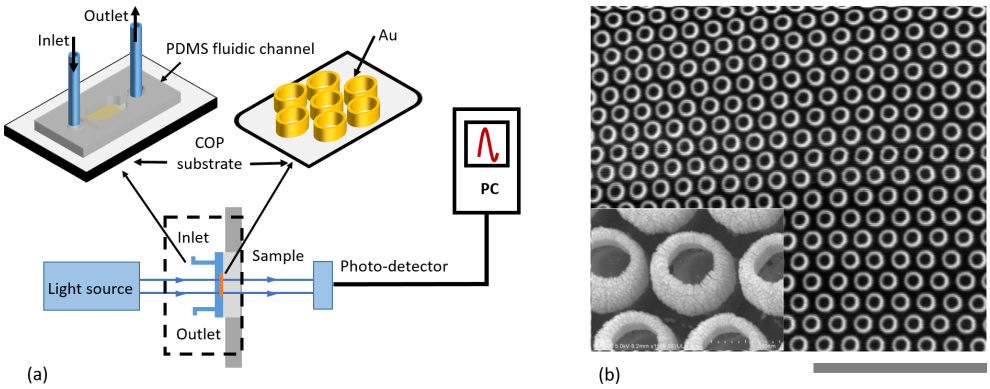

Figure 4–5: (a): Experimental sensing set-up: Cary 5000 spectrometer was used in the sensing experiment, a baseline with PDMS channel and buffer solution is taken first, then the measurements were performed on the functionalized nanotube structures, the solutions were injected using an automatic pump (Harvard Apparatus-PicoPlus) with 200 μL/min flow speed. The inset shows the PDMS fluidic channel: the grooved part is bonded to the surface of the COP (sandwiching the nanostructures between the PDMS and COP, the inlet/outlet are punched using a biopsy puncher to insert the fluidic tubes). (b): SEM image of the fabricated structures: inner diameter= 200 nm, gold layer thickness= 60 nm, and pitch= 400 nm. The gray scale measures 3 μm and 400 nm with respect to the outer image and the inset, respectively.

transformed into normalized vectors and projected on the reference matrix (shown in Fig. 4–1) by using Eq. (4.3) and Eq. (4.4). This also provided a direct measurement to the refractive index of the ethanol solutions as shown in Fig. 4–6 (right Y-axis).

To provide a fair and complete comparison, the measured resonance wavelengths obtained by the dip-finding method are translated into refractive indices by using the FDTD calculated sensitivity (S_B=582.9 nm/RIU) as follows

$$n = n_0 + \frac{\Delta\lambda_r}{S_B}, \quad \Delta\lambda_r = \lambda_r - \lambda_0 \tag{4.5}$$

where n is the calculated refractive index based on the measured resonance wavelength, λ_r; n_0 is the buffer refractive index; and λ_0 is the resonance wavelength when buffer solution is injected.

To validate the results of the FDTD sensitivity calculations and the projection method, we had to compare the experimentally determined refractive indices with reported values in the literature. However, the reported values for ethanol-water mixture are at 589.29

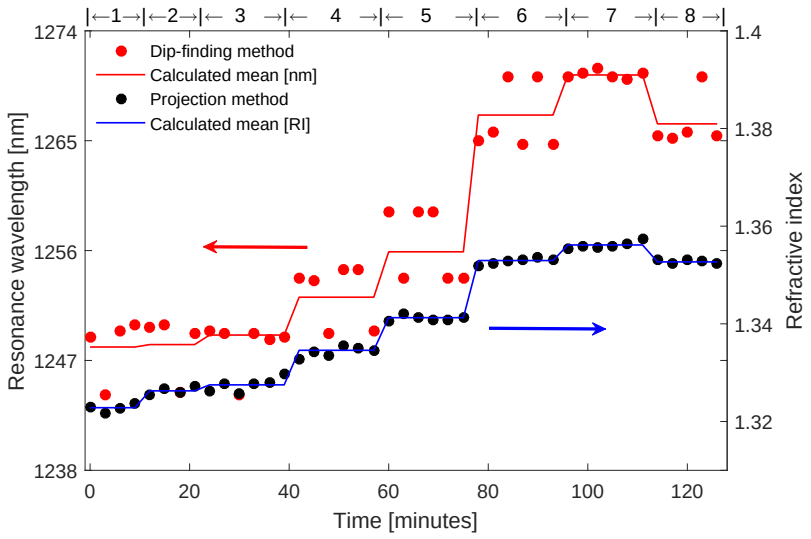

Figure 4–6: Real time sensing measurements for ethanol solutions with different concentrations ([1]: 0%, [2]: 2%, [3]: 4%, [4]: 16%, [5]: 30%, [6]: 50%, [7]: 80%, [8]: 100%) in the case of: dip-finding method (left Y-axis); and projection method (right Y-axis) where the refractive index is directly extracted.

nm [128], whereas the values determined here are at 1247 nm. We used the improved Cauchy formula [129] to estimate the correct index values at the sensor's resonance wavelength (1247 nm)

$$n^2(\lambda) = C_0 + \frac{C_1}{\lambda^2} + \frac{C_2}{\lambda^4} + C_3\lambda^2 \tag{4.6}$$

The Cauchy parameters for Deionized (DI) water and ethanol are known. However, this is not the case for the ethanol-DI water mixture. This motivated us to estimate the Cauchy parameters for all the tested ethanol solutions $(0\% - 100\%)$. Since the refractive indices for the 50% and 100% ethanol solutions are approximately equal, we can use the known Cauchy parameters for pure DI water and ethanol $(0\%, 50\%, and\, 100\%)$ in curve fitting each Cauchy parameter for the mixtures and write these parameters in terms of fitting coefficients of the form

$$C_{\mathscr{K}} = \mathscr{F}_0 + \mathscr{F}_1 w + \mathscr{F}_3 w^2 \tag{4.7}$$

where the subscript $(\mathscr{K} = 0, 1, 2, 3)$ denotes the order of the Cauchy parameters, (w) is the concentration of ethanol in percent weight, and $(\mathscr{F}_0, \mathscr{F}_1, \mathscr{F}_3)$ are the fitting coefficients.

Table 4.1: Fitted Cauchy parameters for all the tested ethanol solutions at 20 °C

$\%w$	C_0 $\times 10^{-3}$	C_1 $\times 10^{-3}$	C_2 $\times 10^{-3}$	C_3 $\times 10^{-3}$
0	1768.80±1.34	2.37±0.93	0.87±0.17	-16.51±0.48
2	1772.63±1.38	2.619±0.96	0.84±0.175	-15.74±0.49
4	1776.35±1.42	2.85±0.98	0.80±0.179	-14.99±0.51
16	1796.53±1.62	4.13±1.12	0.63±0.204	-10.94±0.58
30	1815.36±1.80	5.33±1.25	0.47±0.227	-7.16±0.65
50	1833.47±1.99	6.48±1.38	0.31±0.25	-3.52±0.71
80	1841.23±2.07	6.97±1.43	0.24±0.26	-1.96±0.74
100	1833.47±1.99	6.48±1.38	0.31±0.25	-3.52±0.71

Therefore, we obtained four equations to calculate the four Cauchy parameters for all ethanol solutions (of different concentrations) as shown in table 4.1.

To validate the fitted Cauchy parameters, we used them along with the Cauchy formula [Eq. (4.6)] to calculate refractive index of ethanol solutions at 589.29 nm, and the results agree well with those reported in [128], as shown in Fig. 4–7 (a).

For ethanol-DI-water mixture, the peak refractive index occurs at $80 - 82\%$; the peak location is insensitive to wavelength as it occurred at 77% ethanol solution measured at different wavelengths ∼589 nm, 1310 nm and 1550 nm, at 25 °C [130]. The drop in refractive index (for concentrations higher than the peak location) is attributed to the ethanol water dissociation and molecular repulsive forces: a close packing of water ethanol increases with concentration and reaches its maximum at 82% where the mixture volume reaches the minimum. As the concentration of ethanol exceeds 82%, the repulsive forces between water and ethanol molecules increase the intermolecular spaces, and the RI decreases as a result [131]. The peak location is slightly influenced by the temperature: it occurs with 82.86% ethanol solution at 20 $^{\circ}C$; with 77.35% ethanol solution at 30 °C; and with 82.86% ethanol solution at 35 °C [131]. The refractive indices reach their maximum values at 20 °C; this effect has been taken into account in fitting the Cauchy parameters as we based the calculations on the Cauchy parameters for DI-water and ethanol at 20 °C.

Now, we can use the fitted Cauchy parameters and the Cauchy formula to calculate the refractive indices of the ethanol solutions at the sensor operating wavelength (1249 nm), and

compare them with the measured sensing results. Fig. 4–7 (b) suggests that the measured results and the calculated counterparts follow a similar trend, with a discrepancy at around the 30% concentration.

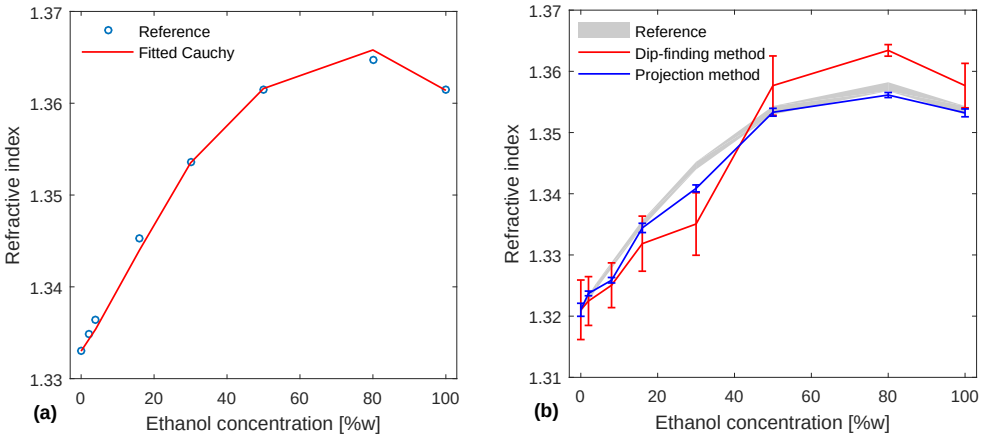

Figure 4–7: (a): Calculated refractive index based on the fitted Cauchy parameters in table 4.1, and the improved Cauchy formula [Eq. (4.6)] at 20 °C and 589.29 nm wavelength: the estimated values agree well with those of reference [128].(b): Sensor response to bulk solutions of different ethanol concentrations using the projection and dip-finding methods: the error bars correspond to repeated measurements (at 20 °C, and 1247 nm resonance wavelength), the reference curve was obtained using the Cauchy empirical formula, Eq. (4.6), and the fitted Cauchy parameters in table 4.1 — calculated using the polynomial curve fitting — at the same temperature and sensor operating wavelength (20 °C and 1247 nm).

Now we compare the projection method with the methods discussed in earlier sections, we translate the response of each method to a refractive index value using Eq. (4.5); however, each method provides a different value as a response (centroid methods estimate the resonance locations and the NDIR and integrated response methods provide normalized intensity based responses). The centroid methods reveal different resonance locations due to the asymmetrical shape of the resonance curves. Therefore, the sensitivity has to be recalculated according to the response of each method, the calculated values for the sensitivity are as follows: 525.7 nm/RIU for the fixed-boundary centroid method; 577.9 nm/RIU for the dynamic-baseline centroid method; 0.4/RIU for the integrated response method; and 5478.4 /RIU for the NDIR method. The RI change can be estimated as the ratio of the response of each method to its sensitivity S_B

$$\Delta n = \frac{\Delta R}{S_B} \tag{4.8}$$

where Δ R denotes the response change with respect to the ethanol concentrations ($\Delta\lambda$ in the case of the centroid methods, and Δ I_{int}, or Δ NDIR in the case of integrated response and NDIR methods). Fig. 4–8 compares the projection method with the reference methods. Signal to noise ratio is calculated based on the mean (signal) and standard deviation (noise) of the measured data at each step (representing the change in ethanol concentration in the bulk solution) as follows

$$SNR(dB) = 10 \times \log(\frac{\overline{\Delta n}}{\sigma_{RI}}) \tag{4.9}$$

where $\overline{\Delta n}$ and (σ_{RI}) are is the steady state mean and standard deviation (due to noise) of the refractive index shift. The sensor refractive index resolution can be estimated as Δ n$\sim$ σ_{RI}, corresponding to SNR$\sim$ 1.

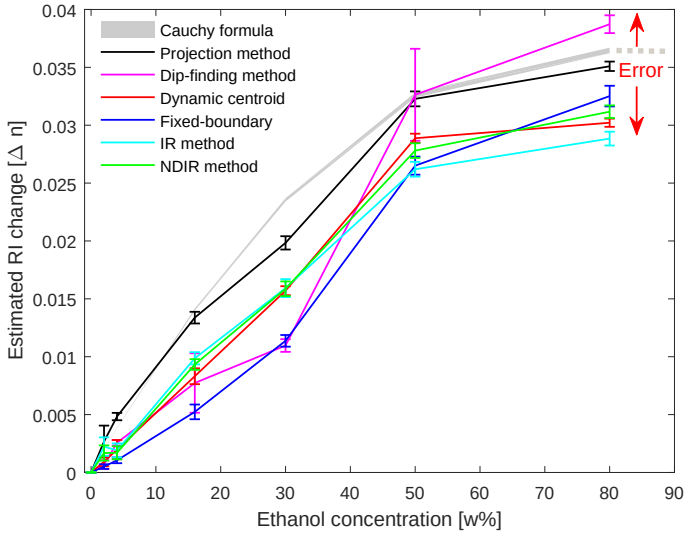

Figure 4–8: RI change measured by the projection method for ethanol solutions of different concentrations. The RI change estimated by the reference methods are also shown: the measured response of each method in Fig. 4–6 was used to calculate the RI change using Eq. (4.5) for a better comparison with the projection method. The standard deviation of the measured refractive indices are represented by error bars for each method, and by the line width for those based on the Cauchy formula.

The error was calculated as the average of the percentage error in the measured RI

changes over the entire range of ethanol concentrations

$$\varepsilon = \frac{1}{m}\sum_{i=1}^{m}\frac{|\Delta n_i - \Delta n_{true,\,i}|}{\Delta n_{true,\,i}}$$

where Δn_i are the measured RI changes, and $\Delta n_{true,\,i}$ are the true values for the RI changes corresponding to the ethanol concentrations. Table 4.2 provides a complete list of the calculated values of SNR, RI resolution and error in RI change. The projection method outperforms the dip-finding method, the fixed-boundary centroid method, the integrated response method and the NDIR method in terms of SNR improvement, and it provides essentially the same SNR performance as the dynamic-baseline centroid method. The projection method provides a more accurate estimation of the refractive index changes based on simulated and measured results. Based on the FDTD results [Fig. 4–4], the error was about 0.2% and 10% for the projection and dynamic-baseline centroid methods respectively; and based on the measured data, the error was $\sim 14\%$ and $\sim 33.97\%$ for the projection and the dynamic-baseline centroid method, respectively. The projection method also provides the lowest RI resolution along with the NDIR method. The high error values revealed by the fast centroid method are attributed to the wide boundaries (wavelength range) that were used in the calculations. A narrower boundary would decrease the sensor RI dynamic range as an upper limit of refractive index has been previously reported to be 1.35 RIU [108]. Providing a direct measurement for the refractive index is considered as another advantage of the projection method.

Temperature fluctuations and spectral resolution also have significant effects on the sensor performance; the spectral resolution of the spectrometer used in our experiments was (0.2 nm); this limited the refractive index resolution to $\sim 2.5 \times 10^{-4}$ RIU. However, this is close to the value that was reported for a high resolution LSPR sensor $\sim 3 \times 10^{-4}$ RIU [132]. In a recent work, a LSPR sensor, based on metallic nanostructures, achieved a FOM $\sim$108 (narrow FWHM $\sim$ 9.5 nm, and high RI sensitivity $\sim$1,015 nm/RIU) [133]. Although this FOM is much higher than that of the nanotube structures, the resolution was only $\sim 2\times10^{-4}$ RIU due to the limited spectral resolution of the spectrometer $\sim$0.1 nm, and the measured

Table 4.2: Comparison between the projection method and the published counterparts.

Method	SNR [dB]	RI resolution [RIU]	Error in estimated Δn
Proposed Projection method	32.07	7.5×10^{-4}	14.62%
Dip-finding method [99]	8.95	1×10^{-2}	33.94%
Dynamic-baseline centroid [101]	32.97	1.95×10^{-3}	33.97%
Fixed-boundary centroid [108]	24.34	1.35×10^{-3}	48.46%
Integrated response [88]	21.47	7.5×10^{-4}	27.92%
NDIR method [107]	24.22	4×10^{-4}	27.58%

signal was constrained to a specific angle to excite the mode of the nanostructures [133]. The proposed projection method achieved the same RI resolution although the measured curves were extremely broad and noisy. Moreover, the spectra were generated by a direct transmission measurement set-up.

We also conducted surface binding experiments to determine the performance of the projection method in estimating the effective refractive index change due to surface binding. We adopted the functionalization protocol used in [117] for biotin functionalization and prepared the streptavidin solution (as explained in section 4.2). The measured RI change, based on each method, was obtained using the sensitivity factor for each method ($\Delta n = R/S_B$) [Eq. 4.8], as shown in Fig. 4–9 (a). The sensograms are based on the averaged response for repeated experiments (6 experiments). Repeating the experiments plays a key role in determining the stability of the results based on each method. The published results for the surface binding experiments are based on only one sensing experiment [134] and thus deviate from the results shown in Fig. 4–9 (a). The LoD can be determined as the minimum detectable change in streptavidin concentration, corresponding to $3\,\sigma_R/S_B$ of the sensor response based on each method. These values ($3\,\sigma_R/S_B$) are plotted as horizontal lines, intersecting the measured Δn graphs at the minimum detectable streptavidin concentration (LoD), as shown in Fig. 4–9 (b). The least LoD was achieved by the NDIR method and integrated response methods, followed by the proposed projection method and then by the fixed-boundary centroid method and the dynamic-baseline centroid method, as shown in Fig 4–9 (b). The dip-finding method revealed the highest LoD (233 μg/mL), explaining why a change of 200 μg/mL in streptavidin concentration was undetectable by this method [steps: 2 and 3, Fig. 4–9 (a)]. These results confirm the findings of our published work [134].

The sensor LoD depends on the analyte to be detected, its molecular weight, and the binding conditions during the experiment. Thus, the bulk RI resolution is used here to compare the projection method with the previously published approaches. The results suggest that the NDIR and integrated response methods can be adopted if a qualitative study of binding events is of importance, whereas the proposed projection method can be employed for mapping the effective refractive index during sensing experiments. Although the NDIR method provided an improved response here, it has previously incurred a response instability and yielded a distorted real time sensogram based on surface binding experiments [88].

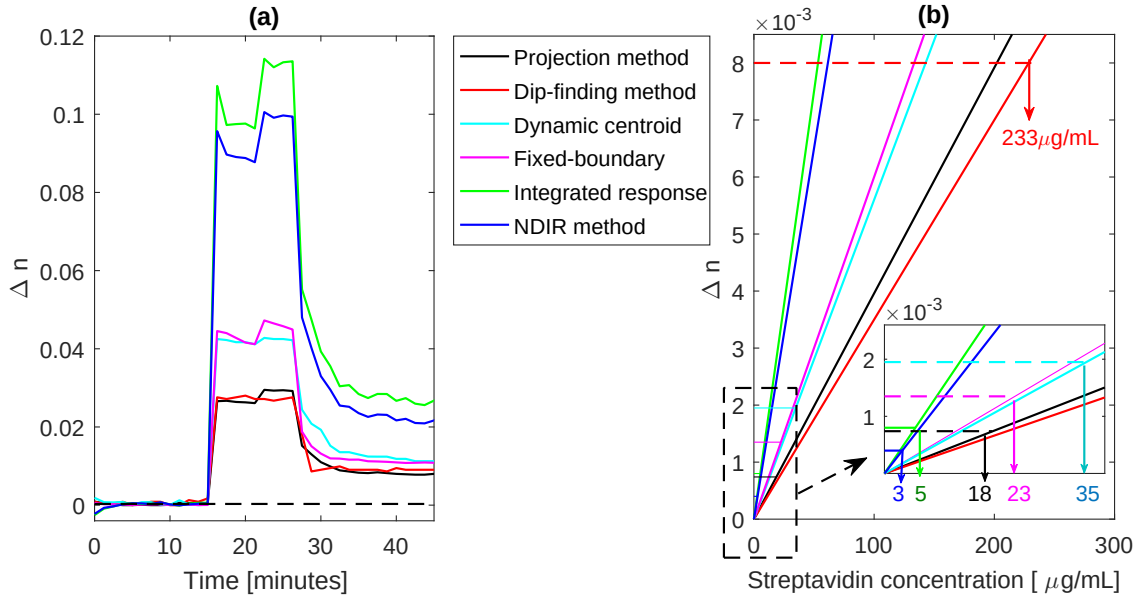

Figure 4–9: (a) Measured RI change based on sensor response to bioten-streptavidin surface binding events. The projection method provides the RI change directly, and the other methods use the sensitivity to translate their response into RI changes (dividing each response to its sensitivity factor). The scale, over the figure, denotes the sequence of flushing the solutions as [1]: Tris buffer solution was injected for the first 15 minutes to create a baseline, then streptavidin solutions – with [2]: 0.6 mg/mL and [3]: 0.8 mg/mL concentrations – were injected sequentially. Tris buffer silane was injected as a final step to flush unbound streptavidin. (b) Measured RI change for various streptavidin concentrations based on all the methods. The standard deviation of the measured RI change by each method σ_{RI} is used to plot $3\sigma_{RI}$ (the horizontal lines) on the measured Δn graph. Each $3\,\sigma_{RI}$ horizontal line intersects with the measured Δn graph at the minimum detectable streptavidin concentration (LoD). The vertical arrows point out the LoD based on each method.

It is also important to consider computational complexity; the reference methods described above have a computational complexity that grows as $\sim O(j)$ where j is the number of wavelength samples. During operation, the proposed projection method projects the measured spectrum against a set of pre-calculated spectra, indicating a computational complexity of $\sim O(i\,j)$ where i is the number of reference spectra, which were used to produce the reference matrix $\mathbf{M}$ (typically 40). As a result, it does require more computation than the other methods, but given the power of even modest current microprocessors, this does not impact the ability to use it for real-time measurement (as shown in our measurement of binding kinetics).

4.4 Summary

This chapter introduced a new signal processing technique to improve signal to noise ratio of localized surface plasmon resonance biosensors. The method provided the refractive index directly from extremely broad and noisy transmission spectra. The measured refractive indices agree well with those calculated using the fitted Cauchy parameters with a slight discrepancy at 30% ethanol concentration. The projection method improved the SNR by one order of magnitude ($\sim$ ten-fold increase compared to the absolute SNR with the dip-finding method), and hence improved the RI resolution from $1 \times 10^{-2}\,RIU$ in the case of dip-finding method to $7.5 \times 10^{-4}\,RIU$. The projection method provided a comparable SNR relative to the dynamic-baseline centroid method; however, it outperforms the dynamic-baseline centroid method in terms of accuracy, based on both simulated and measured results. The projection method provides a higher SNR compared to the integration technique and normalized difference integrated response methods, although the latter provided the same RI resolution. The projection method avoids some of the previously reported limitations of the reference methods, such as the introduction of distortions to the sensogram (reported for the NDIR method [88]) or reductions in dynamic range (reported for the fixed-boundary centroid method [108]). The projection method does however require a modest increase in computation. Although the measured RI resolution achieved by the proposed projection method is $7.5 \times 10^{-4}\,RIU$, the simulated results reveal that the method can resolve a RI change of $\sim 1 \times 10^{-5}\,RIU$. This limit is due to the spectral resolution of the spectrometer ($0.2\,nm$). The results can be improved by using a temperature controller and a photodiode array detector with improved resolution.

5

Linear Maximum Likelihood Estimation Method for Improving Self–referenced Biosensing

5.1 Introduction

Chapter 4 proposed the projection method to improve signal to noise ratio (SNR) based on the measured refractive index (RI). The method was limited by external sources of noise, such as temperature and analyte transport into the fluidic channel. This chapter introduces a method based on the maximum likelihood estimation (MLE) that reduces the effect of noise on the measured results. The method also improves self-referencing for localized surface plasmon resonance (LSPR) biosensors.

In propagating SPR sensors, a reference channel is required to compensate for artifacts due to temperature drift and bulk RI changes [109]. However, the reference sensing channels are not coincident (for example: different metal thickness) due to fabrication imperfections, the difference in analyte transport in both channels [110], and the uncorrelated effects in each channel during the binding events (presence of air bubbles and changes in speed of fluid flow in either channel [111]). These artifacts have motivated many researchers to seek alternative methods where the reference channel can be abandoned to avoid any external or intrinsic effects in the two-channel sensing platforms. A self–referenced SPR sensor has previously employed the excitation of a dual mode SPR (with different penetration depths) using two laser sources [112], which increases the instrumental complexity. Alternative approaches included the excitation of dual-mode SPR and use it as reference/sensing channels based on a linear response model. This was achieved by either exciting dual modes at different locations on the metal surface [113], or exciting the long range and short range SPR modes on the same location of the SPR surface [114, 115]. The linear response model assumes that each resonance wavelength shift ($\Delta\lambda$) is a linear function of both adlayer thickness (d) and bulk RI change (Δn):

$$\Delta\lambda_i = \frac{\partial\lambda_i}{\partial n}\,\Delta n + \frac{\partial\lambda_i}{\partial d}\,d \tag{5.1}$$

The same approach (i.e. a linear response model) has been applied to gold nanorod structures, U-shaped structures and propagating plasmon waveguide resonance biosensor [116–118]. Although various approaches have been introduced for self-referencing SPR platforms, less effort has been previously paid to self–referenced LSPR sensors and improving the linear response model. The maximum likelihood estimation (MLE) approach presented in this thesis improves the precision of the results based on the linear response model. The thesis also provides a method to overcome the repetitive simulation to determine the sensitivity to adlayer thickness for various analytes and correct it based on the measured bulk RI sensitivity. In the next chapter I will show that further improvement can be obtained by moving beyond the linear response model.

5.2 Concept of self referencing based on multiple resonances

As described above, estimating the unknown quantities (adlayer thickness and bulk RI change) requires at least two-resonances. The multiple resonance characteristic of nanorod structures can be employed to generate multiple resonances each of which provides solutions for the estimates. Herein, a three-resonance nanorod structures is considered as the first resonance is used with the second and third resonances to generate three systems of linear equations based on the linear response model [Eq. (5.1)], and the adlayer and bulk RI change can be estimated accordingly as follows

$$\underbrace{\begin{bmatrix}\Delta n_{12}\\ d_{12}\end{bmatrix} = \begin{bmatrix}\frac{\partial\lambda_1}{\partial n} & \frac{\partial\lambda_1}{\partial d}\\ \frac{\partial\lambda_2}{\partial n} & \frac{\partial\lambda_2}{\partial d}\end{bmatrix}^{-1}\begin{bmatrix}\Delta\lambda_1\\ \Delta\lambda_2\end{bmatrix}}_{LM1{:}\,from\,\lambda_1,\lambda_2},\quad \underbrace{\begin{bmatrix}\Delta n_{13}\\ d_{13}\end{bmatrix} = \begin{bmatrix}\frac{\partial\lambda_1}{\partial n} & \frac{\partial\lambda_1}{\partial d}\\ \frac{\partial\lambda_3}{\partial n} & \frac{\partial\lambda_3}{\partial d}\end{bmatrix}^{-1}\begin{bmatrix}\Delta\lambda_1\\ \Delta\lambda_3\end{bmatrix}}_{LM2{:}\,from\,\lambda_1,\lambda_3}$$

$$\underbrace{\begin{bmatrix}\Delta n_{23}\\ d_{23}\end{bmatrix} = \begin{bmatrix}\frac{\partial\lambda_2}{\partial n} & \frac{\partial\lambda_2}{\partial d}\\ \frac{\partial\lambda_3}{\partial n} & \frac{\partial\lambda_3}{\partial d}\end{bmatrix}^{-1}\begin{bmatrix}\Delta\lambda_2\\ \Delta\lambda_3\end{bmatrix}}_{LM3{:}\,from\,\lambda_2,\lambda_3}$$

For a system based on more resonances, we can obtain i number of estimates (d_i and Δn_i) from the linear response models (LM_i), which are related to the true values ($\hat{d}$ and $\widehat{\Delta n}$) by

$$d_i = \hat{d} \pm \varepsilon_{d_i} \tag{5.2}$$

$$\Delta n_i = \widehat{\Delta n} \pm \varepsilon_{n_i} \tag{5.3}$$

where ε_{d_i} and ε_{n_i} represent the errors (due to the noise) in the adlayer thickness and bulk RI change estimated by the multiple resonance linear response model.

5.3 Concept of the Maximum likelihood estimation method

The maximum likelihood estimation method is employed to improve both the accuracy and precision of the estimated adlayer thickness and bulk RI change determined by a linear

response model here and a nonlinear response model in the forthcoming chapter. Herein, the general concept of the MLE method is explained. Suppose that $\hat{x}$ represents the estimates ($\hat{d}$ or $\widehat{\Delta n}$), and y_i, indicating the measured quantities by the LSPR sensor, is related to the estimates as follows

$$y_i = C_i\,\hat{x} \pm \varepsilon_{y_i} \tag{5.4}$$

where C is a weighting coefficient that relates the measured results to the estimates, and ε_y represents the error in the measured quantities (y). Considering that the noise in the system follows a normal distribution, each error term can be represented by a Gaussian distribution with zero mean and a variance, $\varepsilon_{y_i} \sim \mathcal{N}(0, R_{y_i})$. It is evident that the calculations consider the noise associated with the measured resonance wavelength shifts in real time, and the errors include covariances that account for a system of correlated noise sources. In matrix notation, this can be represented by the following symmetric matrix

$$\mathbf{R_y} = \begin{bmatrix} R_{y_{11}} & \dots & R_{y_{1i}} \\ \vdots & \ddots & \vdots \\ R_{y_{i1}} & \dots & R_{y_{ii}} \end{bmatrix} \tag{5.5}$$

where the main diagonal of this matrix represents the variance of each measured quantity, and the covariances among them are symmetrically distributed above and below the main diagonal, i.e. $R_{y_{ij}} = R_{y_{ji}}$. This matrix is directly based on the real time experiments (the variance of the measured quantity, such as wavelength shift).

Now, we apply the MLE method employing y_i and the errors associated with them as presented in Eq. (5.2) and Eq. (5.3). Since we have considered a normal distribution for the noise, the likelihood of obtaining the true values represented by $\hat{x}$ given those determined by the measured quantities (represented by y_i) can be obtained by multiplying the normal distributions for these estimates. In matrix notation this can be expressed as follows

$$P(y_1, ...y_i|\hat{x}\,C_1, ...\hat{x}\,C_i, R_y) = \prod_i \frac{1}{(2\pi)^{i/2}|R_y|^{1/2}} \exp\big(-\frac{1}{2R_y}(y_i - \hat{x}\,C_i)^2\big) \tag{5.6}$$

$$= \frac{1}{(2\pi)^{i/2}|R_y|^{1/2}} \exp\big(-\frac{1}{2R_y}\sum_i (y_i - \hat{x}\,C_i)^2\big) \tag{5.7}$$

The above multivariate likelihood can be expressed in matrix notation as follows

$$P(\mathbf{y}|\hat{x}\,\mathbf{C}) = \frac{1}{(2\pi)^{i/2}|\mathbf{R_y}|^{1/2}} \exp\big(-\frac{1}{2}(\mathbf{y}-\hat{x}\,\mathbf{C})^T\mathbf{R_y^{-1}}(\mathbf{y}-\hat{x}\,\mathbf{C}) \tag{5.8}$$

According to the MLE, the estimate that maximizes the likelihood of obtaining the true value is obtained when the derivative of the above likelihood with respect to the true value approaches zero [135]. For simplicity, we obtain the log of the above likelihoods as follows

$$ln\,P(\mathbf{y}|\hat{x}\mathbf{C}) = -\frac{i}{2}ln(2\pi) - \frac{1}{2}ln|\mathbf{R_y}| - \frac{1}{2}(\mathbf{y}-\mathbf{C}\,\hat{x})^T{\mathbf{R_y}}^{-1}(\mathbf{y}-\mathbf{C}\,\hat{x}) \tag{5.9}$$

Now, the true value can be estimated such that the derivative of the log likelihood with respect to this true value is equal to zero [135].

$$\frac{\partial}{\partial\hat{x}}\,ln\,P(\mathbf{y}|\hat{x}\mathbf{C}) \equiv \frac{\partial}{\partial\hat{x}}(\mathbf{y^T}\,\mathbf{R_y^{-1}}\,\mathbf{y} - \mathbf{y^T}\,\mathbf{R_y^{-1}}\mathbf{C}\,\hat{x} - \mathbf{C^T}\,\hat{x}\,\mathbf{R_y^{-1}}\,\mathbf{y} + \mathbf{C^T}\,\hat{x}\,\mathbf{R_y^{-1}}\,\mathbf{C}\,\hat{x}) = 0 \tag{5.10}$$

$$\Rightarrow -\mathbf{y^T}\,\mathbf{R_y^{-1}}\,\mathbf{C} - \mathbf{C^T}\,\mathbf{R_y^{-1}}\,\mathbf{y} + 2\,\mathbf{C^T}\,\mathbf{R_y^{-1}}\,\mathbf{C}\,\hat{x} = 0 \tag{5.11}$$

Since $\mathbf{y^T}\,\mathbf{R_y^{-1}}\,\mathbf{C} = \mathbf{C^T}\,\mathbf{R_y^{-1}}\,\mathbf{y}$, Eq. (5.11) can be solved for the estimate $\hat{x}$

$$\hat{x} = \frac{\mathbf{C^T}\,\mathbf{R_y^{-1}}\,\mathbf{y}}{\mathbf{C^T}\,\mathbf{Ry^{-1}}\,\mathbf{C}} \tag{5.12}$$

$$\mathbf{C} = \begin{bmatrix} C_1 \\ \vdots \\ C_i \end{bmatrix}\ \mathbf{y} = \begin{bmatrix} y_1 \\ \vdots \\ y_i \end{bmatrix}\ \mathbf{R_y^{-1}} = \begin{bmatrix} R_{y_{11}}^{-1} & \dots & R_{y_{1i}}^{-1} \\ \vdots & \ddots & \vdots \\ R_{y_{i1}}^{-1} & \dots & R_{y_{ii}}^{-1} \end{bmatrix} \tag{5.13}$$

In the case of the three-resonance nanorod structures, proposed here, the system is unbiased, $\mathbf{C^T} = [1\ 1\ 1]$, substituting for i=3 and $\hat{x} \to \hat{d}$ or $\widehat{\Delta n}$, $y \to d$ or Δn and using Eq. (5.12), the adlayer thickness and bulk RI change can be estimated as follows

$$\hat{d} = \frac{(R_{d11}^{-1} + R_{d12}^{-1} + R_{d13}^{-1})\, d_1 + (R_{d12}^{-1} + R_{d22}^{-1} + R_{d23}^{-1})\, d_2 + (R_{d13}^{-1} + R_{d23}^{-1} + R_{d33}^{-1})\, d_3}{R_{d11}^{-1} + R_{d22}^{-1} + R_{d33}^{-1} + 2\,(R_{d12}^{-1} + R_{d13}^{-1} + R_{d23}^{-1})} \tag{5.14}$$

$$\widehat{\Delta n} = \frac{(R_{n11}^{-1} + R_{n12}^{-1} + R_{n13}^{-1})\Delta n_1 + (R_{n12}^{-1} + R_{n22}^{-1} + R_{n23}^{-1})\Delta n_2 + (R_{n13}^{-1} + R_{n23}^{-1} + R_{n33}^{-1})\Delta n_3}{R_{n11}^{-1} + R_{n22}^{-1} + R_{n33}^{-1} + 2\,(R_{d12}^{-1} + R_{d13}^{-1} + R_{d23}^{-1})} \tag{5.15}$$

5.4 Corrected sensitivity matrices for the linear response model

The sensitivity to adlayer thickness depends on the refractive index of the adlayer (n_a) and the bulk RI sensitivity of the nanorods. Therefore, it needs to be recalculated if other biological samples are considered. Established methods based on the linear response model have previously considered specific analytes, and employed sensitivity factors based on simulating that specific analyte (using reported values for size and RI). [117, 118]. However, this requires tedious numerical modeling to obtain new values. Here, we present a method to avoid the repeated numerical calculations, by calculating the adlayer sensitivity based on the measured data.

The maximum sensor response, $\Delta\lambda_{max}$, at each resonance is achieved when the adlayer thickness reaches the saturation, $d \gg l_d$, where l_d is the electromagnetic (EM) decay length associated with these resonances. The sensor response is related to the adlayer thickness by the following equation [136, 137]

$$\Delta\lambda(d) = \Delta\lambda_{max}[1 - exp(-2\,d/l_d)] \tag{5.16}$$

Therefore, the linear response model is valid for thin adlayer thickness, $d \leq l_d/10$, and the sensor response can be related to the adlayer thickness based on the sensitivity to adlayer thickness $\sim S_d$ as follows

$$\Delta\lambda(d) = S_d\, d \tag{5.17}$$

Substituting $d = l_d/10$ in Eq. (5.16) and Eq. (5.17), the wavelength shift can be determined

as follows

$$\begin{aligned}\Delta\lambda(l_d/10) &= S_d\, ld/10 \\ &= 0.18\,\Delta\lambda_{max}\end{aligned}$$

from which the sensitivity to the adlayer thickness can be evaluated as follows

$$S_d = 1.8\,\Delta\lambda_{max}/l_d \tag{5.18}$$

This can be related to the bulk RI sensitivity and the refractive indices for the buffer and analyte as follows

$$S_d = 1.8\,(n_a - n_B)\frac{S_B}{l_d} \tag{5.19}$$

where n_a and n_B are the refractive indices for the adlayer and the buffer solution. It is evident that the adlayer sensitivity is proportional to the ratio of the bulk sensitivity to the EM decay length, interpreting the similar adlayer sensitivity for propagating and localized SPR sensors, as $S_B/l_d|_{SPR} \approx S_B/l_d|_{LSPR}$.

5.5 Methods

The FEM method was used to model the gold nanorods and obtain the bulk RI and adlayer sensitivities, as well as the EM decay length for each resonance. The dielectric properties for gold were obtained from Johnson and Christy experimental data [48]. The longitudinal mode was excited by an incident plane wave polarized along the major axis of the gold nanorods. The rods were modeled based on both perfectly matched layer and periodic boundary conditions. An adlayer of thickness (d) was introduced to calculate the EM decay length as the resonance wavelength shift was tracked with changing the thickness until the shift is saturated. The simulation domain was discretized using triangular mesh and the nanorods and the adlayer were discretized using hexagonal mesh of 1 nm element size.

The gold nanorods were fabricated using the side–wall lithography method: a glass substrate was coated by 50 nm thick cyclic olefin copolymer (COC) by spin coating, and the

coated substrate was imprinted by Si mould under 8 MPa pressure and 150 $^{\circ}C$ for 300 seconds. The imprinted substrate was then coated with 5 nm and 30 nm thick Cr and gold, respectively. The nanorods were formed after lift-off process. Fig. 5–1 shows a micrograph for the fabricated noanords. Replica moulding method was used to fabricate the fluidic channels based on polydimethylsiloxane (PDMS), described in chapter 4 and Appendix C.

The fabricated substrate was then cleaned by DI water and ethanol solution, blown dry with nitrogen, and plasma treated to remove any biological contaminant. The substrate was then incubated in 10 mM phosphate buffer solution (pH 7.2) of 200 μM biotin-hpdp for biotin immobalization as instructed in [117, 139]. A 0.2 mg/mL streptavidin solution was prepared in a 50 mM Tris-buffer solution (pH 8.0) according to [117, 139]. The Tris buffer was also used as a baseline for the sensing experiment. Both streptavidin and hpdp reagents were obtained from [140]. Cary 5000 spectrometer was used to measure the extinction curves while injecting different samples by an automatic pump (Harvard Apparatus −PicoPlus) with $200\mu L/min$ flow speed.

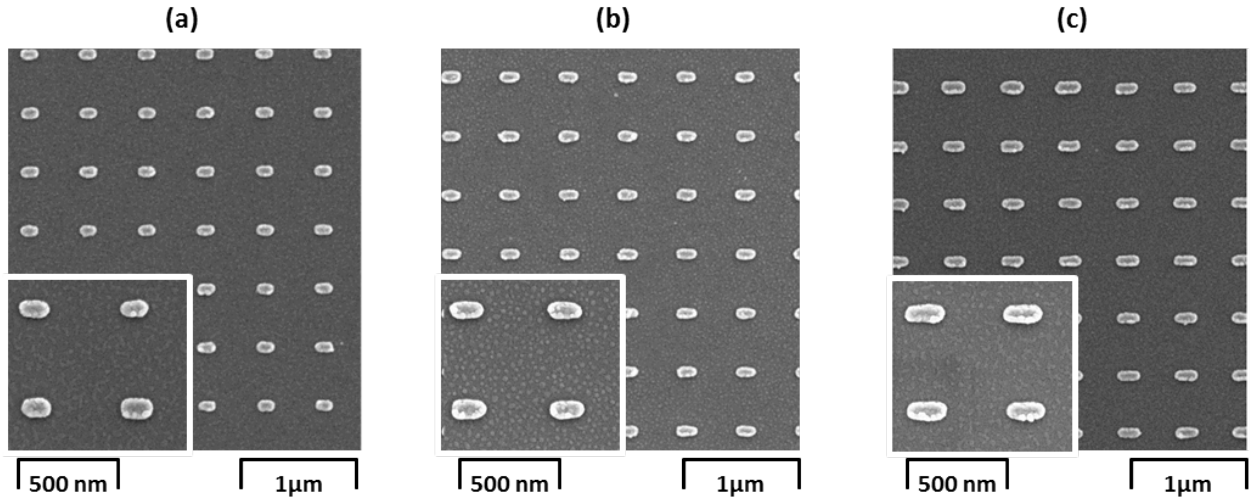

Figure 5–1: SEM images for the fabricated nanorod structures with 70 nm in width and various lengths as (a) 120 nm, (b) 150 nm, and (d) 210 nm.

5.6 Numerical validation

COMSOL Multi-physics was used to calculate the shifts in resonance wavelengths with various bulk refractive indices to calculate the sensitivity at each resonance. Fig. 5–2 (a) shows the simulation layout based on the periodic boundary condition and ports to calculate the scattering parameter S_{21}, which can be translated into transmission efficiency as $10^{S_{21}/20}$. The simulation was validated by simulating only the glass substrate using a refractive index of 1.5, and calculating the transmission efficiency. Another verification was performed by comparing the results based on nanorods without a substrate to those obtained based on nanorods in a sphere with perfectly matched layer shown in Fig. (b).

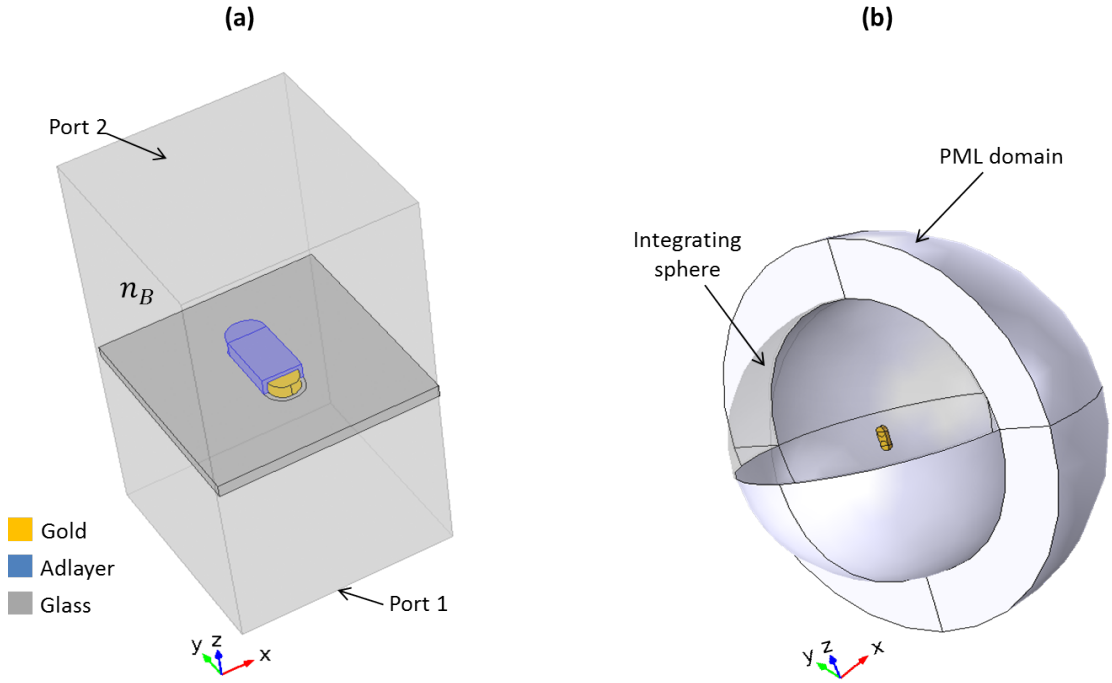

Figure 5–2: (a) Schematic for a COMSOL Multiphysics model to simulate periodic array of nanorods after introducing adlayer thickness and bulk RI n_B. Periodic boundary conditions were enforced such that the nanorods are periodic in the x-y plane. The structure is excited using port 1 (lower x-y plane), and the transmitted light wave is collected using port 2 (upper x-y plane). (b) Simulating a single nanorod using PML boundary condition and integrating sphere to calculate the extinction efficiency. The nanorod is excited by a plane wave polarized along the z axis, propagating in the negative x direction.

After validating the simulation set-up, the sensitivity to bulk RI change (S_B) was calcu-

lated based on the corresponding transmission dip locations for all the resonances as shown in Fig. 5–3. As expected, the third resonance wavelength (1000 nm) exhibited the highest sensitivity to bulk RI changes which is attributed to the long EM decay length. To estimate the EM decay length, the adlayer thickness was varied from 6–25 nm, and the corresponding shift in each resonance wavelength was tracked to plot the resonance shift against adlayer thickness. The EM decay lengths are then estimated by fitting the simulated data using Eq. (5.16), as shown in Fig. 5–4. As well, the simulated adlayer sensitivity can be determined as the slope of the curves in the linear regime ($0 < d < l_d/10$).

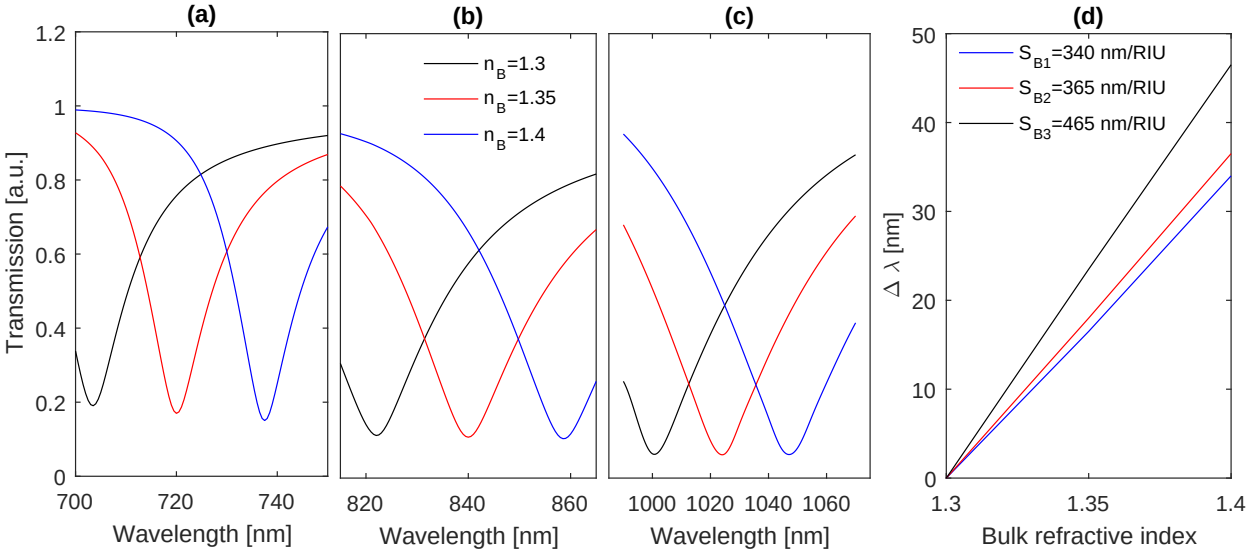

Figure 5–3: Simulated transmission curves, demonstrating the dependence of the resonance wavelengths on the bulk RI (a) $\lambda_1 = 705\,nm$, (b) $\lambda_1 = 821\,nm$, and (c) $\lambda_1 = 1000\,nm$. The sensitivity curves for these resonance wavelengths are presented in (d) S_{B1}, S_{B2} and S_{B3} correspond to λ_1, λ_2 and λ_3, respectively.

To investigate the effect of the noise on the results, an adlayer of 5 nm thickness and 1.4 refractive index was introduced to the nanorods in the periodic simulation layout, and the corresponding shifts in the resonance wavelengths were determined. Last, noise (with different levels) was simulated by adding uncertainties (various σ_λ) to the simulated wavelength shifts. The linear response models and the proposed linear MLE method were then employed to estimate the input parameters used in the FEM model. The SNR of the estimates were calculated as the ratio of the mean to the standard deviation of the estimates. The SNR

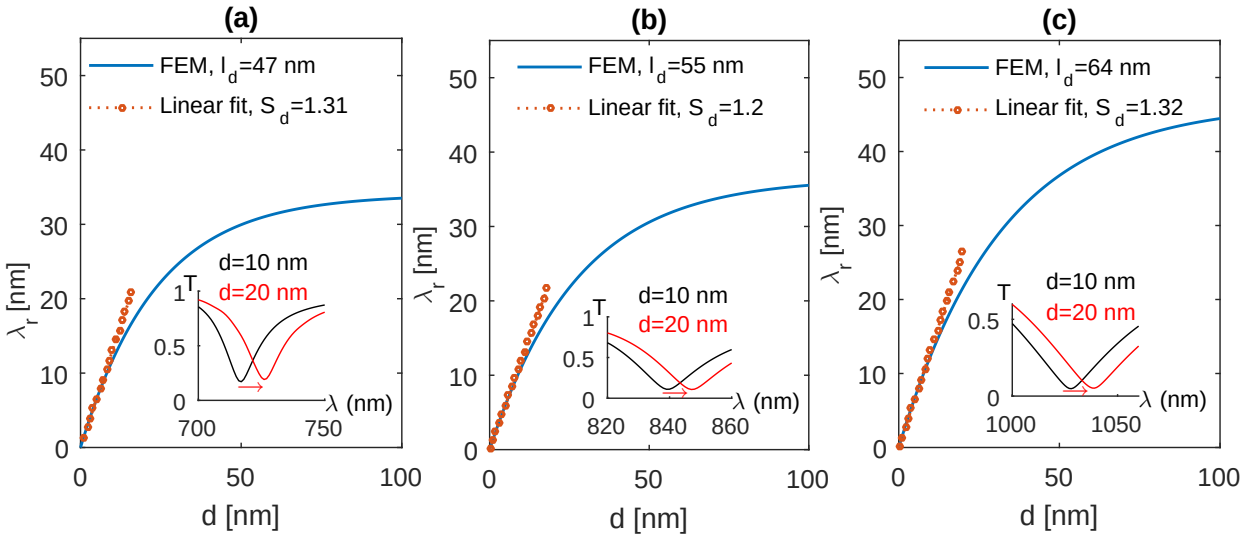

Figure 5–4: Resonance shift against adlayer thickness change, based on the simulated results shown in the insets, for (a) the first resonance, (b) the second resonance, and (c) the third resonance. The EM decay length (l_d) for each resonance is extracted such as Eq. (5.16) provides the best fit to the resonance wavelength shift vs adlayer curves, and the sensitivity to adlayer thickness change (S_d)is calculated as the slope of each curve at the linear regime ($d \sim l_d/10$).

based on the estimated adlayer thickness and bulk RI change are shown in Fig. 5–5 (a) and (b), respectively, revealing that the MLE can improve the precision of the linear response model results; the MLE method is less affected by the fluctuations in the resonance wavelengths as the overall variance becomes lower than any variance associated with the linear response models. The accuracy of the methods can be determined based on the percentage error in the estimates compared with the true values used in the simulation as follows

$$\epsilon_{\hat{x}}\,\% = \frac{\hat{x} - x}{x} \times 100 \tag{5.20}$$

where $\epsilon_{\hat{x}}\,\%$ is the percentage error in the estimates $\hat{x}$ ($\hat{d}$ or $\widehat{\Delta n}$) with respect to the true values x, representing d or Δn. The averaged errors in the adlayer thickness and bulk RI change are shown in Fig. 5–5 (c) and (d). These averaged errors were estimated based on different $SNR(\Delta\lambda)$ [Figs. 5–5 (a,b)], and suggest that the linear–MLE achieves the best accuracy among the linear response models, based on the simulated data.

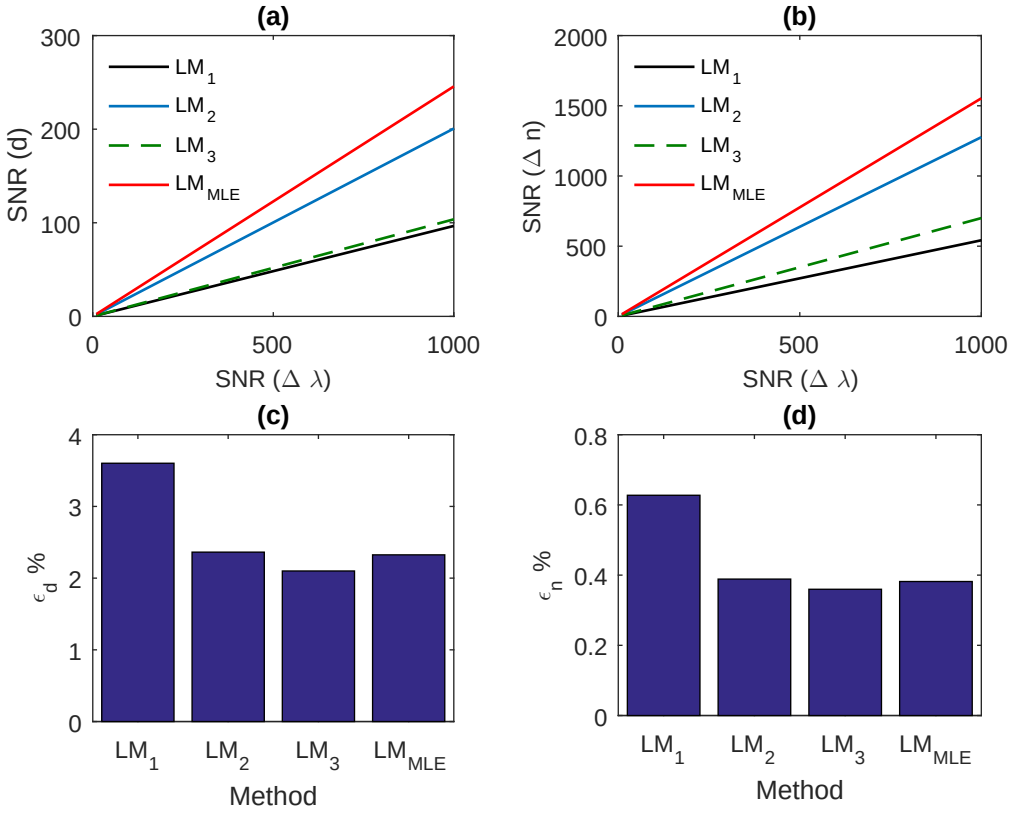

Figure 5–5: Top panel: calculated SNR based on (a) the estimated adlayer thickness to its standard deviation, and (b) the estimated bulk RI change to its standard deviation. The linear response model and the linear–MLE method were applied to the simulated shifts in resonance wavelengths $\Delta\lambda_i$ with added uncertainties $\sigma_{\lambda i}$ such that $SNR(\Delta\lambda_i) = \Delta\lambda_i/\sigma_{\lambda i}$. Bottom panel: the percentage error associated with each method in (c) the estimated adlayer thickness and (d) the bulk RI change using Eq. (5.20) based on the true values used in the simulation.

5.7 Measured results

This section presents the measured results based on bulk RI change and surface binding experiments. Fig. 5–6 shows the experimental set–up used for the sensing experiments. Transmission curves were obtained while introducing the solutions into the nanorod structures via the PDMS fluidic channel. The resonance locations (centroids) were determined based on the dynamic-baseline centroid method [101].

Fig. 5–7 shows the measured results for the three–resonance nanorod structures based on ethanol solution and biotin-streptavidin binding. The shift of each resonance is tracked

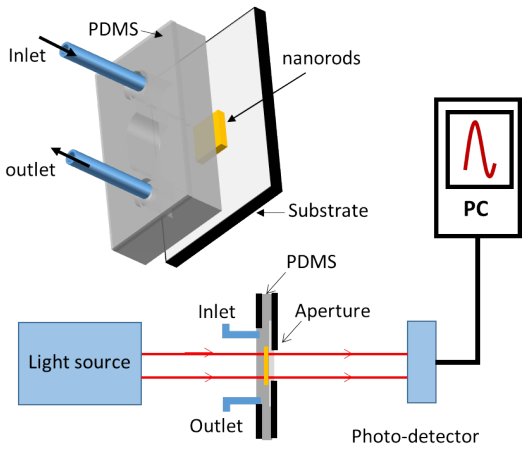

Figure 5–6: Experimental set-up for measuring the transmission spectra of the nanorod structures. The inset shows an exploded view for the PDMS fluidic channel integrated with the gold nanorod substrate (for injecting the biological samples).

in real time to investigate the self-referencing with bulk and surface binding experiments.

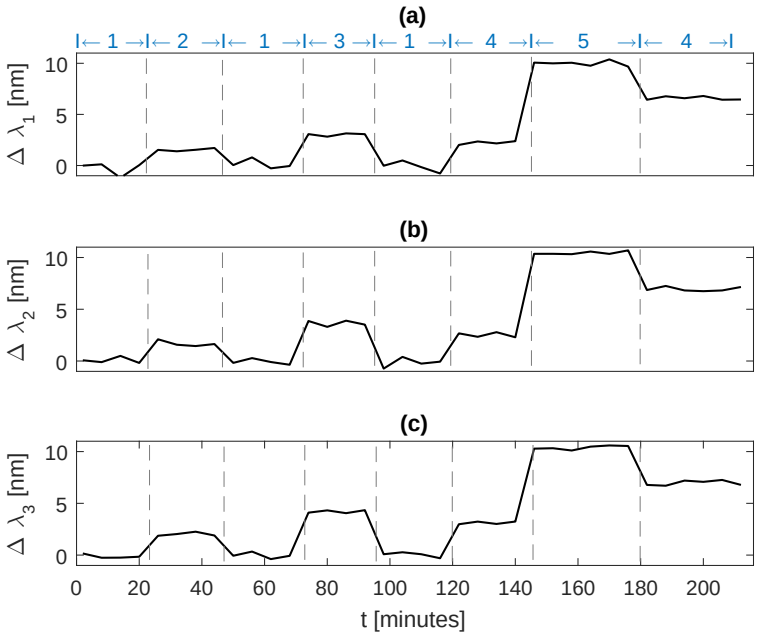

Figure 5–7: Real time response to bulk RI changes and biotin-streptavidin binding events based on three-resonance nanorod structures. The cycles on the graph represent the following: [1] DI water, [2] 8% ethanol solution, [3]16% ethanol solution, [4] Buffer, and [5] Streptavidin solution. The time step is 6 minutes, which was required by the Cary 5000 spectrometer for a single scan of the entire wavelength range.

The sensor was calibrated for the bulk RI and adlayer sensitivities, as the bulk RI sensi-

tivity was calculated based on the ethanol solutions of known concentrations and refractive indices. The measured sensitivities are lower than the calculated counterparts due to the biotin layer as the distance between the nanorods and the ethanol solutions is increased after functionalizing the nanorods. A similar behaviour was previously observed for the nanorods [141]. We propose a method to correct for this discrepancy as the sensitivity to adlayer thickness is directly related to the bulk RI sensitivity. This can be achieved by using Eq. (5.19). The simulated and measured sensitivities are shown in Fig. 5–8 (a), (b) and (c), whereas the corresponding calibration curves for the simulated and corrected adlayer sensitivities are shown in Fig. 5–8 (d), (e) and (f).

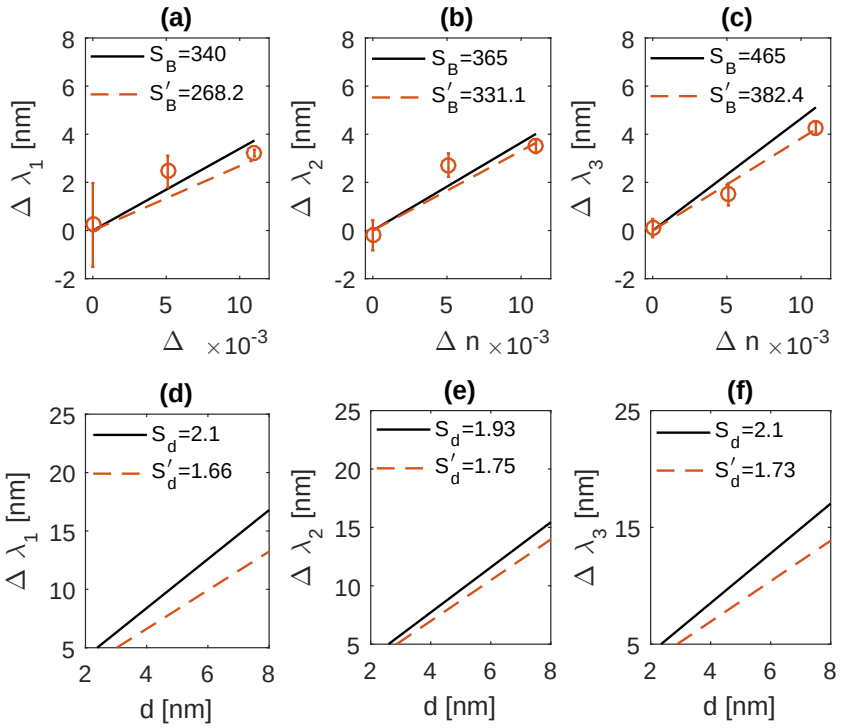

Figure 5–8: Top panel: simulated versus measured shift in resonance wavelengths against bulk RI changes. The bulk RI sensitivities, S_B and S'_B (nm/RIU), were determined as the slope of each graph. Bottom panel: simulated and measured resonance shifts versus the adlayer thickness based on the simulated (S_d) and corrected (S'_d) adlayer sensitivities. Each corrected sensitivity (S'_d) was obtained using Eq. (5.19) based on the measured bulk RI sensitivity S'_B for each resonance.

Now, we obtain sensitivity matrices based on the true values, accounting for the changes

due to fabrication and experimental conditions, in the form

$$S = \begin{bmatrix} S'_{B1} & S'_{d1} \\ S'_{B2} & S'_{d2} \end{bmatrix}$$

These matrices must be non–singular and well conditioned to be valid for the LM calculations [142]. The determinant of each sensitivity matrix is nonzero, hence non-singular. We also calculated the condition number $\kappa(S_{LM})$ by first normalizing the columns of each sensitivity matrix, obtaining a normalized matrix s_{LM}, and then multiplying the norm of the normalized matrix and the norm of its inverse as follows

$$\kappa(S_{LM}) = \|s_{LM}\| \, \|s_{LM}^{-1}\|$$

The calculated condition numbers of the sensitivity matrices are 25.6, 13 and 25.8 for $LM_1(\lambda_1, \lambda_2)$, $LM_2(\lambda_1, \lambda_2)$ and $LM_3(\lambda_2, \lambda_3)$, respectively. These values mean that the matrices are well conditioned ($\kappa(S_{LM}) < 100$). Since the adlayer sensitivities have been corrected based on the measured bulk RI sensitivities using Eq. (5.19), the condition number based on the measured and simulated sensitivity matrices are in close agreement with each other. The calculated condition numbers of the simulated sensitivity matrices are ∼25.6, 13, 25.7, implying that correcting for the adlayer sensitivity results in stable condition numbers, and hence improved numerical accuracy. This can be useful in optimizing the nanorod structures.

It is also important to investigate the sensor figure of merit based on the full width at half maximum (FWHM) given by $\sim FoM = S_B/FWHM$. The calculated FoMs for the first, second and third resonances are 3.1, 2.7 and 2.6, respectively. These values exceed those associated with gold nanorods fabricated by the electron beam lithography $\sim$ 1.9 [116]. However, these values are comparable to the FoM reported for chemically synthesized nanorods, $\sim 1.7 - 2.6$ [143]. This is attributed to the increased sensitivity of the nanorods presented in this thesis $289 - 382.37\, nm\, RIU^{-1}$ due to the increased width of the nanorods, as increasing the rods minor axes was previously linked to increasing the EM decay length and improving the bulk RI sensitivity [141].

Another interesting parameter to consider is the figure of merit based on adlayer–bulk RI differentiation that can be determined as $\chi = |S_{B_1}/S_{d_1} - S_{B_2}/S_{d_2}|$ [114, 116]. The proposed multiple resonance nanorod structures revealed the following based on the measured sensitivities: 0.18 with LM(λ_1,λ_2), 0.38 with LM(λ1,λ_3) and 0.17 with LM(λ_2,λ_3) compared to 0.18, 0.38 and 0.17 based on the simulated sensitivities, exhibiting an improved stablity system when compared to established dual–resonance nanorod structures whose measured figure of merit differed from the simulated counterpart ~ 0.25 vs 1, respectively [116].

The estimated adlayer thickness and the bulk RI change using the linear response model based on the corrected sensitivity matrices are shown in Fig. 5–9 (a–c). The estimates based on the linear–MLE were obtained by applying Eq.(5.14) and Eq. (5.15) to the results obtained from the linear response models; in particular, the mean and variance of the adlayer thickness and bulk RI change determined by the linear response models. The results based on the linear–MLE method are shown in Fig. 5–9 (d), as it can be observed that the linear–MLE method improves the accuracy and precision based on both bulk RI and surface binding experiments.

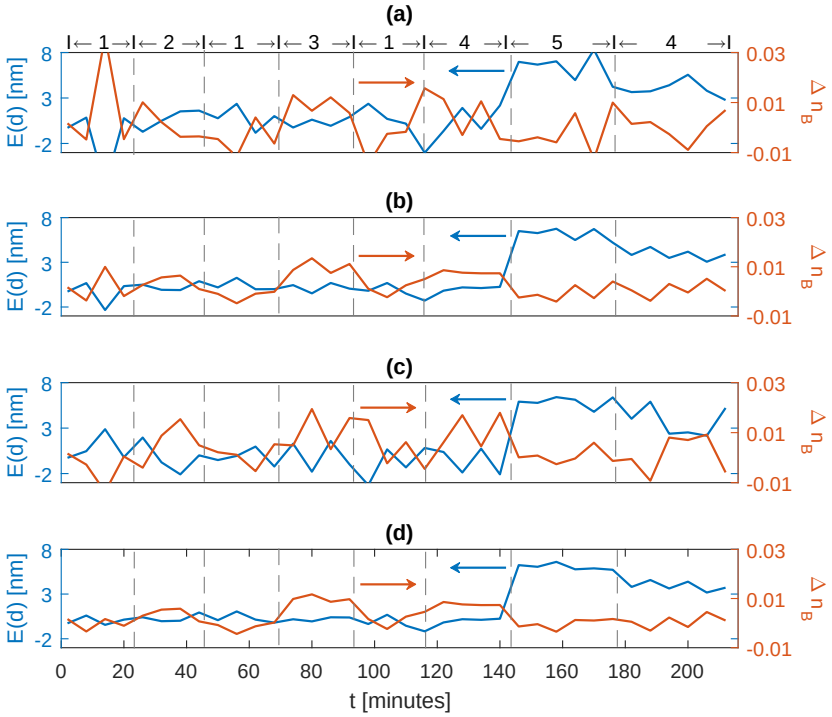

Figure 5–9: Estimated adlayer thickness (left y-axis) and bulk RI change (right y-axis) based on the measured results after applying (a) $LM_1(\lambda_1, \lambda_2)$, (b) $LM_2(\lambda_1, \lambda_3)$, (c) $LM_3(\lambda_2, \lambda_3)$, and (d) the linear–MLE method. The cycles on the graph represent the following: [1] DI water, [2] 8% ethanol solution, [3]16% ethanol solution, [4] Buffer, and [5] Streptavidin solution.

Since ethanol solutions with known refractive indices were used in the first part of the experiment, as shown in Fig. 5–9, their reported refractive indices [128] can be used as a reference to calculate the errors in the estimated RI change based on each method. Fig. 5–10 (a) shows both the error and standard deviation of the bulk RI change estimated by the linear response model and the linear–MLE. The linear–MLE improved the accuracy in estimating RI changes of 0, 5.1×10^{-3} and 1.1×10^{-2} with improved precision (improved RI resolution); the averaged error is 6.1×10^{-3}, 1.7×10^{-3}, 2.2×10^{-3} and 9.1×10^{-4} for LM_1, LM_2, LM_3 and the linear–MLE, respectively. This indicates that the accuracy can be increased by one order of magnitude employing the linear–MLE method. The averaged standard deviation of the estimated RI change by the LM_1, LM_2, LM_3 and the linear–MLE method was 3.6×10^{-3}, 1.9×10^{-3}, 5.4×10^{-3} and 1.2×10^{-3}, respectively.

Based on the adlayer thickness and bulk RI change estimated by each method for the biotin-streptavidin binding experiment, steps 4 and 5 in Fig. 5–9, the mean and standard deviation of the estimated d and Δn_B were calculated at each step to investigate the precision of each method, as shown in Fig. 5–10 (b) and (c). The linear–MLE method exhibits a decreased standard deviation based on the estimated adlayer thickness and bulk RI change during the baseline phase, as well as during the association and dissociation phases. The estimated adlayer thickness was 6 nm and 4 nm during the association and dissociation phases, respectively. This suggests that the gold nanorods were not completely functionalized, and there were empty locations that have not been occupied by biotin. The linear response models with higher condition number and lower cross sensitivity figure of merit, χ, revealed the worst results in terms of accuracy and precision. This, however, did not impact the results based on the linear MLE method. The averaged standard deviation was 1.3 nm, 0.54, 1.22 nm and 0.37 nm for LM_1, LM_2, LM_3 and the linear MLE method, respectively. Therefore, the linear MLE method improves the precision and accuracy by factors of 3 and 3.7, respectively.

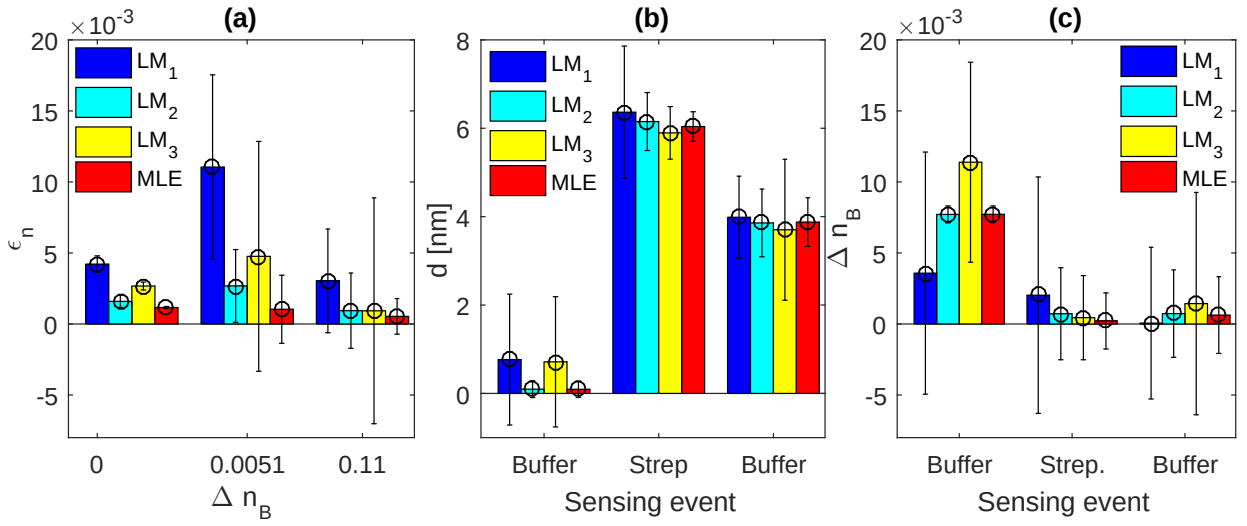

Figure 5–10: (a) Error in the estimated RI change after applying the linear response model (LM_1, LM_2, LM_3), and the linear–MLE method to the measured results. The error was calculated as the difference between the estimated RI changes and the reported counterparts based on refractometer results for ethanol solutions of different concentrations (0%, 8%, and 16 %). The data is obtained from the first five steps in Fig. 5–9 (steps: 1, 2, 1, 3, 1). (b) Estimated adlayer thickness and (c) bulk RI change after applying the linear response model (LM_1, LM_2, LM_3)and the linear–MLE method to the surface binding experimental results. The error bars denote the standard deviation of the estimated values obtained from the last three steps in Fig. 5–9 (steps: 4, 5, 4).

5.8 Summary

This chapter presented a method to improve the accuracy of estimating the adlayer thickness and bulk RI change. The method is based on multiple resonance sensors to generate more than a single system of linear equations, and applies the linear–MLE method to the solutions obtained by these systems (multiple values for adlayer thickness and bulk RI change) to maximize the likelihood of the estimates with lower variance. The chapter also introduced a method to generate sensitivity matrices based on the experimental conditions, reducing errors due to the mismatch between the calculated and measured sensitivities. This can also reduce the numerical calculations if different biological samples are measured, or if the number of resonances is increased. The linear response model is limited to biological adlayers of a maximum thickness of ($\sim l_d/10$). However, LSPR biosensors are aimed to detect such small biological samples. Although the sensing experiments yielded noisy results (based on resonance shift) when compared to some reported measurements, the linear–MLE method improved the results based on the estimated adlayer thickness and bulk RI change. The precision and accuracy were improved by factors of 3 and 3.7 when compared to the averaged results obtained by the linear response model, proving that the method can leverage self-referencing LSPR sensors. Increasing the number of resonances would improve both accuracy and precision of the estimates. The averaged FoM associated with the fabricated nanorods was 2.8 RIU^{-1} and the averaged figure of merit based on the adlayer/bulk RI cross sensitivity, was 0.24; increasing the FoM would further improve the precision, and increasing the bulk RI cross sensitivity figure of merit can achieve improved accuracy. Additional improvement in the precision and accuracy can be achieved by optimizing the nanorods based on these parameters.

6

Nonlinear–MLE method for estimating adlayer thickness and change in bulk refractive index

Chapter five employed the maximum likelihood estimation (MLE) based on a linear response model, assuming that the sensor response is a linear function of the adlayer thickness and change in bulk refractive index (RI). Nevertheless, the linear response model is valid only for extremely low adlayer thickness ($\sim l_d/10$). This chapter improves the accuracy of the results by applying the MLE to a nonlinear response model. The results presented here estimate the changes in adlayer thickness and bulk refractive index based on nanostructures supporting multiple resonances (particularly nanocrescent structures).

U-shaped nanostructures have been used in differentiating between specific and nonspecific bindings based on the multiple-resonance characteristic and streptavidin-bioten binding events [117]. The study assumed that specific binding mostly occurs at the metal surface,

and the nonspecific binding occurs at a distant location (on the substrate), and ignored any non-specific binding that may occur at the metal surface. However, the method requires repetitive simulation in order to determine the sensitivity matrix based on other biological samples, which is a practical limitation of the method. Alternatively, a model that distinguishes bulk RI and adlayer thickness changes is a more practical solution, as it can decouple the effects associated with them. The sensor response — at each resonance — is related to the adlayer thickness and bulk RI changes, as discussed in chapter 2, and the effects can be determined by solving the two equations (corresponding to the number of resonances). Surface plasmon resonance and plasmon waveguide resonance were used as a self-referenced spectroscopy sensor, employing the linear response model, as the effects due to adlayer thickness and bulk RI change were determined [118]. However, the sensitivity matrix (including the adlayer and bulk RI sensitivities for both resonances) must have a low condition number to avoid any numerical errors, which may not be the case for many sensing platforms. This chapter presents a method based on the maximum likelihood estimation to improve the accuracy of the estimated quantities. This implies that the bulk RI resolution and the limit of detection are improved accordingly.

6.1 Nonlinear model for sensor response

The EM field decays exponentially from the surface of the nanostructures with a factor of $exp(-z/l_d)$. Since the intensity is the square of the electric field strength, it decays with a factor of $exp(-2z/l_d)$ away from the nanostructure surface ($z = 0$). Accordingly, the effective refractive index along the z direction can be weighed by using the same decay factor $exp(-2d/l_d)$. Fig.6–1 (a) shows a schematic of the nanocrescent structure and Fig.6–1 (b) ilustrates the RI distribution around the structure. The effective refractive index can be obtained by integrating the refractive indices along z direction as follows [136]

$$n_e = (2/l_d) \int_0^\infty n(z) exp(-2z/l_d) dz$$

where $n(z)$ changes along the z axis as

$$n(z) = \begin{cases} n_a, & \text{if } 0 < z < d, \\ n_B, & \text{if } d < z < \infty. \end{cases} \tag{6.1}$$

where n_a and n_B are the adlayer and bulk refractive indices, respectively.

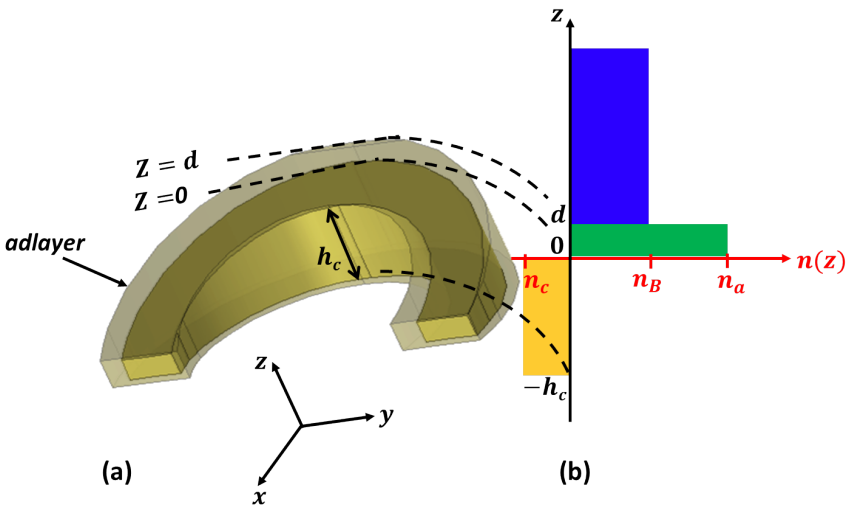

Figure 6–1: (a) Schematic representation of a nanocrescent, surrounded by an adlayer with thickness d. (b) Refractive index distribution showing the negative refractive index of the nanocrescent n_c from $-h_c < z < 0$, the adlayer refractive index n_a from $0 < z < d$, and the bulk RI n_B for $z > d$

This gives

$$n_e = n_a[1 - exp(-2d/l_d)] + n_B exp(-2d/l_d) \tag{6.2}$$

$$= n_B + (n_a - n_B)[1 - exp(-2d/l_d)] \tag{6.3}$$

The resonance shift can be determined by $\Delta\lambda = S\,\Delta n$, where $\Delta n = n_e - n_B$ is the refractive index change. From Eq. (6.3), the following is obtained for the resonance shift

$$\Delta\lambda = S(n_e - n_B) = S(n_a - n_B)[1 - exp(-2d/l_d)] \tag{6.4}$$

Equation (6.4) can be used to estimate the changes in the adlayer refractive index Δn

and thickness d. First, the sensitivity factor S is measured. The buffer solution is injected to obtain the sensing baselines for the three resonances. Hence the resonance wavelength shift $\Delta\lambda$ can be obtained directly from the measured data.

The maximum response occurs when a thick adsorbate layer is reached $d \longrightarrow \infty$, and equation (6.4) becomes

$$\Delta\lambda_{max} = S(n_a - n_B) \tag{6.5}$$

Dividing equation (6.4)by equation (6.5), the following is obtained

$$\frac{\Delta_\lambda}{\Delta\lambda_{max}} = [1 - exp((-2d/l_d)] \tag{6.6}$$

Equation (6.6) can be rearranged as follows

$$ln(1 - \frac{\Delta\lambda}{\Delta\lambda_{max}}) = \frac{-2}{l_d}\, d \tag{6.7}$$

Intuitively, the EM decay length is dependent on the resonance wavelength, and thus the sensor response for a multiple–resonance sensor can be obtained based on equation (6.7) as follows

$$\mathbf{y} = \mathbf{C_d}\, d \pm \mathbf{R_y} \tag{6.8}$$

where the elements of $\mathbf{y}$ can be obtained from the shifts in the measured resonance wavelengths $\Delta\lambda_i$ as $y_i = ln(1 - \Delta\lambda_i/\Delta\lambda_{i,max})$. $\mathbf{C_d}$ contains the coefficients related to the EM decay length as $-2/l_{di}$, whereas $\mathbf{R_y}$ represents the variance and covariance associated with the resonance wavelengths. For a two-resonance sensor $\sim i = 2$, we obtain

$$\mathbf{y} = \begin{bmatrix} y_1 \\ y_2 \end{bmatrix}; \mathbf{C_d} = \begin{bmatrix} C_{d1} \\ C_{d2} \end{bmatrix}; and\ \mathbf{R_y} = \begin{bmatrix} R_{y11} & R_{y12} \\ R_{y12} & R_{y22} \end{bmatrix} \tag{6.9}$$

Applying the MLE [Eq. 5.12]

$$\hat{x} = \frac{\mathbf{C^T\, R_y^{-1}\, y}}{\mathbf{C}^T\, \mathbf{Ry^{-1}\, C}}\,, \quad \mathbf{R_y^{-1}} = \begin{bmatrix} R_{y11}^{-1} & R_{y12}^{-1} \\ R_{y12}^{-1} & R_{y22}^{-1} \end{bmatrix}$$

the adlayer thickness can be estimated as follows

$$\widehat{d} = \frac{(C_{d1}R_{y11}^{-1} + C_{d2}R_{y12}^{-1})y_1 + (C_{d2}R_{y22}^{-1} + C_{d1}R_{y12}^{-1})y_2}{C_{d1}^2 R_{y11}^{-1} + C_{d2}^2 R_{y22}^{-1} + 2\, C_{d1}\, C_{d2} R_{y12}^{-1}} \tag{6.10}$$

If the noise is uncorrelated, the variance $R_{y12} = 0$, and the estimate becomes

$$\widehat{d} = \frac{(C_{d1}R_{y11}^{-1})y_1 + (C_{d2}R_{y22}^{-1})y_2}{C_{d1}^2 R_{y11}^{-1} + C_{d2}^2 R_{y22}^{-1}} \tag{6.11}$$

Likewise, the refractive index change can be estimated with an improved accuracy using the nonlinear–MLE. The shifts in resonance wavelengths can be obtained from Equation (6.4) as follows

$$\Delta\lambda_1 = C_{n1}\, \Delta n \pm R_{\lambda_1}$$
$$\Delta\lambda_2 = C_{n2}\, \Delta n \pm R_{\lambda_2}$$

where $C_{n1} = S_1(1 - e^{-2\hat{d}/l_{d1}})$, and $C_{n2} = S_2(1 - e^{-2\hat{d}/l_{d2}})$, are the sensitivity coefficients, and $\hat{d}$ is the value estimated by equation (6.10) or (6.11). R_{λ_i} is the variance associated with the measured wavelength shift $\Delta\lambda_i$.

The estimated $\widehat{\Delta n}$ that maximizes the likelihood of the above probability assuming correlated noise can be obtained using the MLE equation [Eq. 5.12]

$$\widehat{\Delta n} = \frac{(C_{n1}R_{\lambda_{11}}^{-1} + C_{n2}R_{\lambda_{12}}^{-1})\Delta_{\lambda_1} + (C_{n2}R_{\lambda_{22}}^{-1} + C_{n1}R_{\lambda_{12}}^{-1})\Delta\lambda_2}{C_{n1}^2 R_{\lambda_1 1}^{-1} + C_{n2}^2 R_{\lambda_2 2}^{-1} + 2\, C_{n1}\, C_{n2} R_{\lambda_{12}}^{-1}} \tag{6.12}$$

For the uncorrelated system ($R_{\lambda_{12}} = 0$), this simplifies the above equation to

$$\widehat{\Delta n} = \frac{C_{n1}R_{\lambda_{11}}^{-1}\Delta\lambda_1 + C_{n2}R_{\lambda_{22}}^{-1}\Delta\lambda_2}{C_{n1}^2 R_{\lambda_{11}}^{-1} + m_2^2 R_{\lambda_{22}}^{-1}} \tag{6.13}$$

6.1.1 Methods

The FEM method was used to calculate the sensor response to changes in bulk RI and adlayer thickness, and to validate nonlinear–MLE method. Periodic boundary conditions were enforced along the sides of a hexagonal simulation domain created with commercial COMSOL Multiphysics simulation package, as shown in Fig. 6–2 (a). The refractive index for gold was obtained from Johnson and Christy [48]. The nanocrescents and the adlayer were discretized using a tetrahedral mesh, and the rest of the domain was discretized using triangular mesh. The transmission efficiency was obtained from the scattering parameter S_{21}, as input and output ports were assigned to the bottom and top boundaries of the simulation domain, shown in Fig. 6–2 (a). The results were compared to those based on the linear response model. The non–linear response model along with the MLE method were applied to pre–calculated FEM results to estimate the known adlayer thickness and RI change (used in the simulation). To investigate the performance of the method in the presence of noise, each shift in a resonance wavelength $\Delta\lambda_i$ was perturbed by adding random variations with zero mean and σ_{λ_i} standard deviation such that $SNR = \Delta\lambda_i/\sigma_{\lambda_i}$. Different SNR levels can be obtained by using various σ_{λ_i}.

The experimental sensing method is based on measuring the extinction efficiency in real time by using Cary 5000 spectrometer, illustrated in Fig. 6–2 (b). The nanocrescents were fabricated by the side–wall lithography method, described in Appendix C, and functionalized by biotin-hpdp according to the established surface chemsitry protocol [117, 139] and as explained in the previous chapter. Streptavidin solutions were prepared as discussed in the previous chapters.

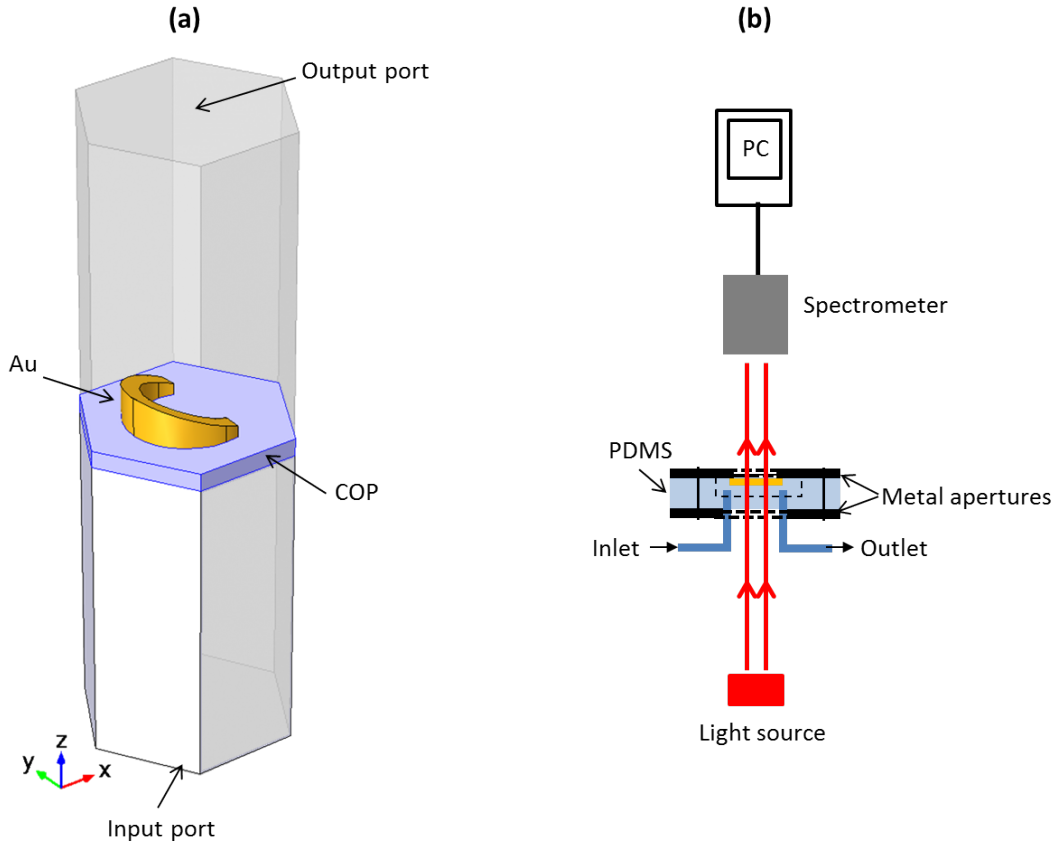

Figure 6–2: (a) Simulation layout used in COMSOL multiphysics to model periodic nanocrescent structure of a hexagonal lattice, by enforcing periodic boundary conditions. (b) Experimental set-up to measure transmission spectra for the fabricated nanocrescent structures.

6.1.2 Simulated results and validation of the estimation method

This section compares the nonlinear–MLE method with the established linear response model based on FEM simulated results, and presents a FEM based evaluation of the accuracy of the measured results based on each method with respect to deviated resonance wavelengths (representing the effect of noise on each resonance wavelength).

The simulated results show distinct values for the sensitivity to bulk RI and adlayer thickness changes. Inspecting both modes based on the adlayer and bulk RI sensitivities can provide an insight into the sensing efficiency for each mode [Eq. (2.42)]

$$\frac{\partial n_{eff}}{\partial d} = \frac{S_d}{S_B} \tag{6.14}$$

Referring to Fig. 6–3 and Fig. 6–4, the first mode (1100 nm) exhibits a lower bulk RI sensitivity, comparing to that associated with the second mode ∼1450 nm (325.25 nm/RIU versus 787.35 nm/RIU). These modes yield adlayer sensitivities of 1.47 and 2.2, respectively. Therefore, the calculated adlayer sensing efficiency is 4.5×10^{-3} RIU/nm and 2.8×10^{-3} RIU/nm. In other words, changing the adlayer thickness by 1 nm would alter the effective RI by 4.5×10^{-3} RIU based on the first mode and 2.8×10^{-3} RIU in the case of the second mode, although the second mode features a higher bulk RI sensitivity than that of the first mode. Here, a combination of linear systems (based on the linear response model) is used with the MLE technique to improve the accuracy and precision of the sensing results.

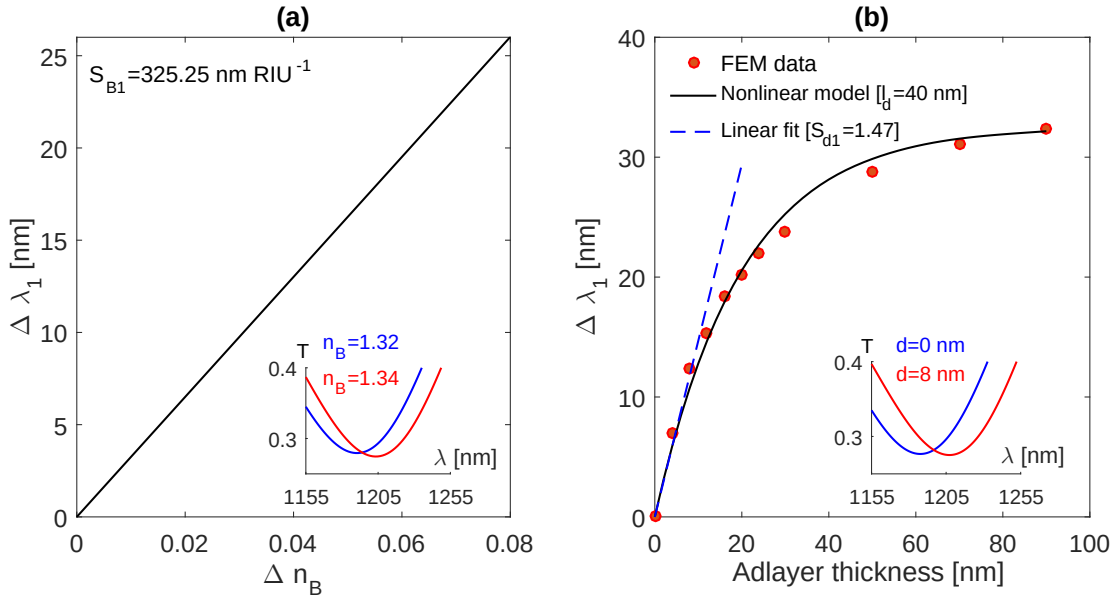

Figure 6–3: Dependence of the first mode (1100 nm) on (a) the bulk RI change, and (b) variations of the adlayer thickness. The results obtained from the nonlinear response model and the FEM calculation follow a similar trend. The following parameters were used in the FEM model:$n_B = 1.3$, $n_a = 1.4$.

The linear response model relates the resonance wavelength shift to the biological adlayer thickness and the bulk RI change by the following relationship

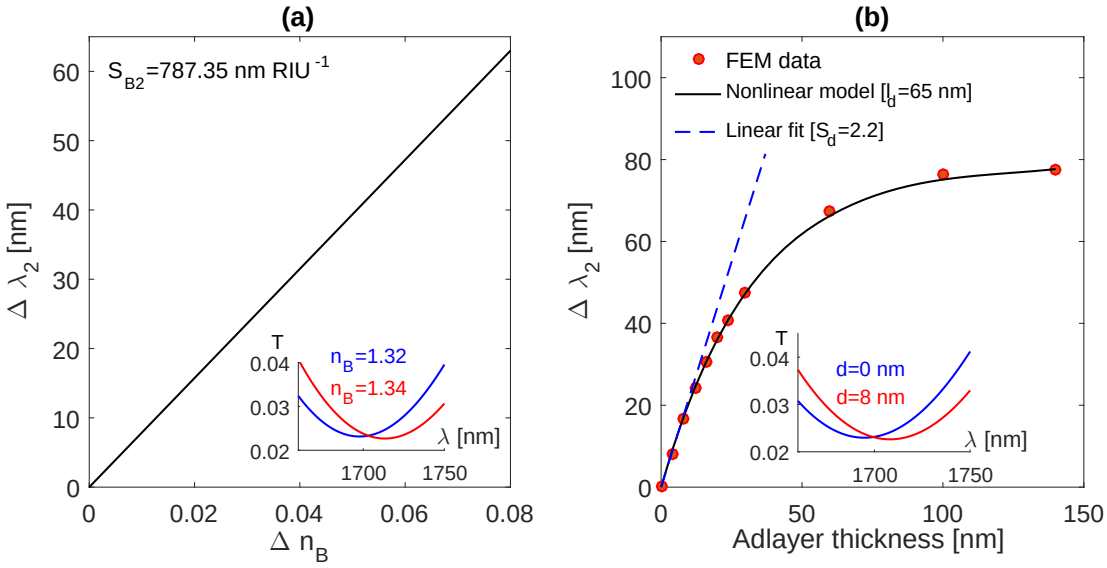

Figure 6–4: (a) Resonance wavelength shift versus bulk RI change associated with the second mode (1450 nm) based on the FEM model. (b) Resonance wavelength shift against adlayer thickness with $n_B = 1.3$, and $n_a = 1.4$, showing a close agreement with the non-linear response model results.

$$\begin{bmatrix} \Delta\lambda_1 \\ \Delta\lambda_2 \end{bmatrix} = \underbrace{\begin{bmatrix} S_{B_1} & S_{d_1} \\ S_{B_2} & S_{d_2} \end{bmatrix}}_{S} \begin{bmatrix} \Delta n \\ d \end{bmatrix} \tag{6.15}$$

The elements of the sensitivity matrix are given in table 6.1. The method used in determining the resonance affects these parameters as the LSPR curves are not symmetric.

The application of the linear response model is valid only if: (i) the sensitivity matrix (S) is not singular, and (ii) the normalized sensitivity matrix (S') is well conditioned. The normalized sensitivity matrix is calculated as follows

$$S' = \begin{bmatrix} \frac{S_{B_1}}{\sqrt{S_{B_1}^2+S_{B_2}^2}} & \frac{S_{d_1}}{\sqrt{S_{d_1}^2+S_{d_2}^2}} \\ \frac{S_{B_2}}{\sqrt{S_{B_1}^2+S_{B_2}^2}} & \frac{S_{d_2}}{\sqrt{S_{d_1}^2+S_{d_2}^2}} \end{bmatrix} \tag{6.16}$$

This matrix meets the above conditions if it has a non–zero determinant and low condition number.

$$S = \underbrace{\begin{bmatrix} 325.25 & 1.02 \\ 787.38 & 1.51 \end{bmatrix}}_{|S|=-366.25\neq 0} \Rightarrow S' \underbrace{\begin{bmatrix} 0.38 & 0.55 \\ 0.92 & 0.84 \end{bmatrix}}_{\kappa(S')=10.49<100}$$

From Eq.(6.15), the adlayer thickness and bulk RI change can be calculated as

$$\begin{bmatrix} \Delta n \\ d \end{bmatrix} = S^{-1} \begin{bmatrix} \Delta\lambda_1 \\ \Delta\lambda_2 \end{bmatrix} \tag{6.17}$$

Now the nonlinear–MLE method is compared to the linear response model based on simulated data with additive white Gaussian noise. The results are based on two methods for determining the dip location, the dip-finding method and dynamic-baseline centroid methods. The elements of the sensitivity matrix depend on each method as shown in Table 6.1.

Table 6.1: Modes supported by the nanocrescent structure and their sensing characteristics, calculated by the dip-finding method and the dynamic baseline centroid methods

	Dip-finding		Dynamic-baseline centroid	
	$\lambda_1 = 1100$	$\lambda_2 = 1450$	$\lambda_1 = 1100$	$\lambda_2 = 1450nm$
S_B $[nm\,RIU^{-1}]$	325.25	787.35	374.25	828.95
l_d	40	65	40	65
S_d	1.02	1.51	1.15	1.58

The nonlinear–MLE method is now employed to estimate the bulk RI change and adlayer thickness—that were used in the simulation— based on the noisy simulated spectra as shown in Fig. 6–5 (a). The resonance wavelength shifts are used to determine the corresponding values for $ln(1 - \Delta\lambda/\Delta\lambda_{max})$, which are then used in Eq. (6.11) to determine the adlayer thickness, as shown in Fig. 6–5 (b). The adlayer thickness is then used to determine the sensitivity coefficient, $C_n = S\,[1 - exp(-2/l_d)]$, to estimate the bulk RI change using Eq. (6.13). The estimated adlayer thickness and bulk RI change are shown in Fig. 6–5 (c). The

results obtained based on the LM are also shown in Fig. 6–5 (b,c). The nonlinear–MLE method revealed the following for the estimates: d=5.95 nm, $\Delta n_B \approx 0$, with 0.47 nm and 1.4×10^{-3} RIU uncertainties, respectively. Under the same conditions, the linear response model revealed 5.5 nm and 1.3×10^{-3} for the estimated adlayer thickness and refractive index change with uncertainties of 1.8 nm and 6×10^{-3}, respectively. This suggests that the nonlinear–MLE can improve the accuracy of the estimated adlayer thickness by one order of magnitude, and the precision by a factor of 4, as shown in Fig. 6–5.

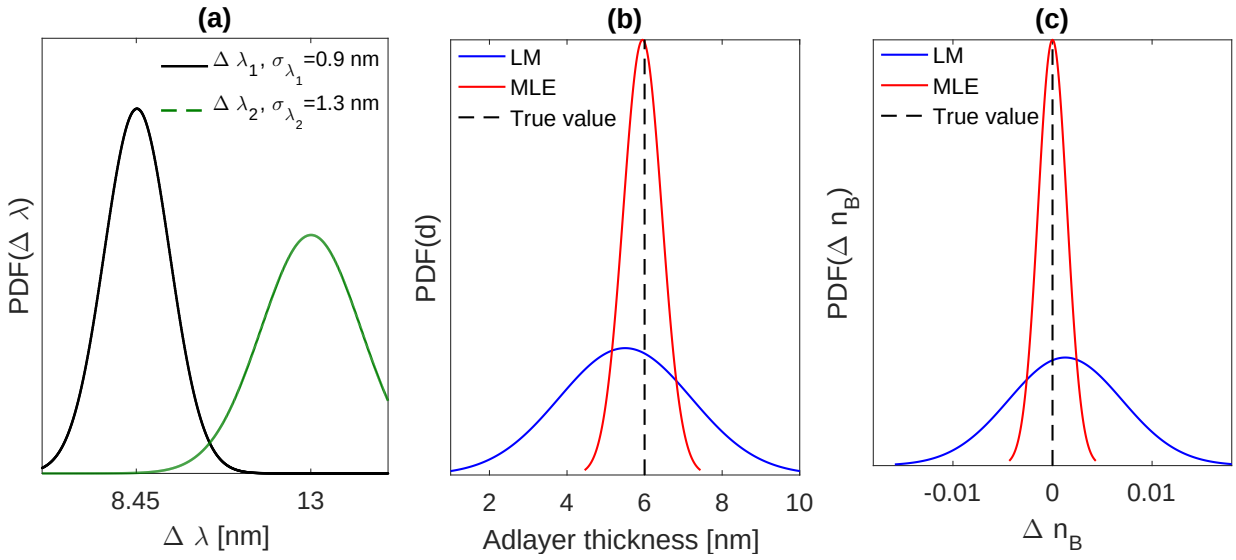

Figure 6–5: (a) Probability density function representation of the calculated shift in the first and second resonance wavelengths, with added errors $\sigma_{\lambda_1} = 0.9, \sigma_{\lambda_2} = 1.3$. The FEM used the following parameters: $n_B = 1.33, n_a = 1.43, d = 6\,nm$. (b) Adlayer thickness and (c)change in bulk RI change, estimated by the nonlinear–MLE (red) and linear response model (blue) methods. The precision for the nonlinear–MLE results: $\sigma_d = 0.09nm, \sigma_n = 1.6 \times 10^{-4} RIU$, The precision of the LM:$\sigma_d = 0.25\,nm, \sigma_n = 6.14 \times 10^{-4}\,RIU$.

Fig. 6–6 compares both methods in terms of accuracy and precision based on adlayer thickness ranging from 6 nm to 25 nm. The percentage error in the estimated adlayer thickness ranges from 0.83–1.96% based on the nonlinear–MLE method, and 8.3–71.6%, based on the linear response model. This indicates that the nonlinear–MLE method can improve the results by a factor of 36 as compared to those based on the linear response model, when the adlayer thickness approaches $\sim l_d/2$. The error in the estimated refractive index tends to be negligible based on the nonlinear–MLE-nonlinear method and increases

drastically based on the linear response model, as shown in Fig. 6–6 (b). The nonlinear–MLE method and the linear response model reveal 5×10^{-3} and 1.5×10^{-2} RIU uncertainties when the adlayer thickness approaches 25 nm, as shown Fig. 6–6 (b).

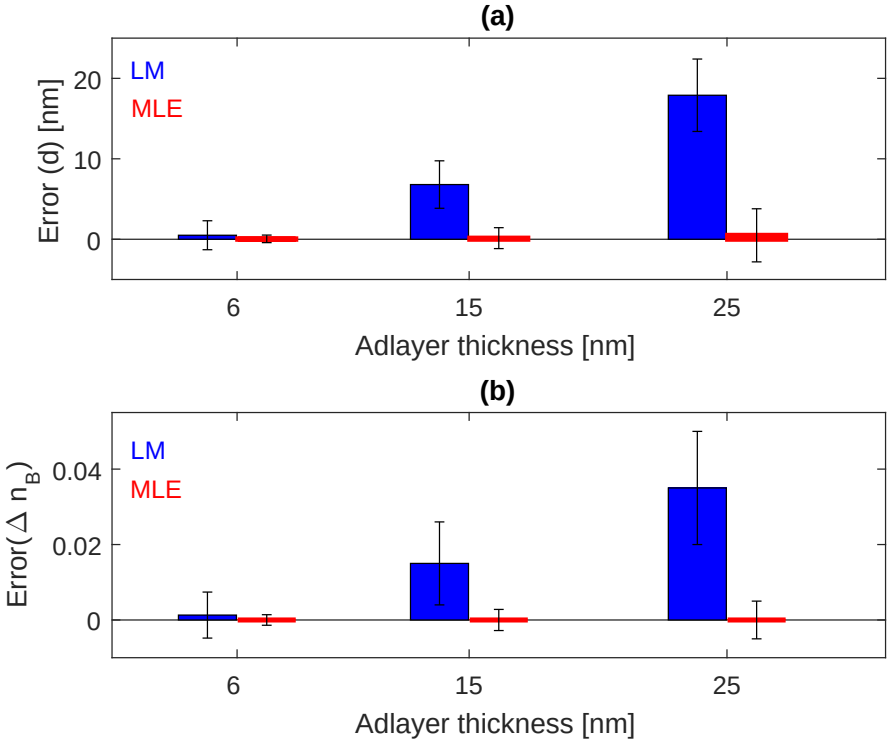

Figure 6–6: (a) Error in the estimated adlayer thickness based on the nonlinear–MLE method (red bars) and the linear response model (blue bars). The following parameters were used in the FEM model: $n_a = 1.43$, $n_B = 1.33$, and $d = \{6\,nm,\ 15\,nm,\ 25\,nm\}$. The shifts in the resonance wavelengths were determined, and each resonance was added uncertainty σ_i, such that each $\Delta\lambda_i/\sigma_i = 10$ (SNR=10). The error was then determined as the difference between the true and estimated values. (b) The error associated with estimated Δn based on the same simulated results used in (a).

6.1.3 Experimental results

This section provides the experimental results based on Bioten-Streptavidin binding events. Before being used in sensing experiments, the fabricated nanocrescent structures were cleaned by DI water and ethanol solution, blown dry with nitrogen, and plasma treated to remove any biological contaminant. Ethanol solutions of different concentrations were used in the bulk RI sensing experiment. The bulk RI sensitivity at each resonance was determined based on

resonance shift against RI change due to changing the concentration in ethanol solution. The measured adlayer sensitivities were determined by using the measured bulk RI sensitivities in correcting the simulated adlayer sensitivities using Eq.(5.18) [Chapter five]. Table 6.2 provides the sensing parameters based on the measured results. The bulk RI sensitivity is used along the EM decay length in Eq. (6.11) and Eq. (6.13) to estimate the adlayer thickness and bulk RI change, respectively, based on the nonlinear–MLE method. This section also compares these results to those obtained based on the linear response model. The linear response model uses the bulk and adlayer sensitivity factors, presented in Table 6.2, in Eq. (6.15) to estimate the adlayer thickness and bulk RI change.

Table 6.2: Modes supported by the nanocrescent structure and their sensing characteristics based on measured results. The dip–finding method and the dynamic baseline centroid method were used to extract the resonance wavelengths.

	Dip-finding		Dynamic-baseline centroid	
	$\lambda_1 = 1100nm$	$\lambda_2 = 1450nm$	$\lambda_1 = 1100nm$	$\lambda_2 = 1450nm$
Sensitivity	330	780	365	800
l_d	40	65	40	65
$\partial\lambda/\partial d$	1.57	2.28	1.73	2.34

Fig. 6–7 (a) shows the shifts in resonance wavelengths based of the measured extinction curves for streptavidin biotin sensing experiments. These shifts were translated into the logarithmic normalized quantity, $ln(1 - \Delta\lambda/\Delta\lambda_{max})$, and used in Eq. (6.11) and Eq. (6.13) to estimate the adlayer thickness and bulk RI change, as shown in Fig. 6–7 (b and (c). Now the linear response model is used based on the same measured data, shown in Fig. 6–7 (a) in estimating the adlayer thickness and bulk RI change using the sensitivity factors, given in Table 6.2, in Eq. (6.15). Fig. 6–7 (c) shows the results based on the linear response model. The limit of detection and bulk RI resolution can be determined based on the standard deviation of the estimated adlayer thickness and bulk RI change, respectively. When compared with the linear response model based on these results, the nonlinear–MLE

method reduces the limit of detection based on the adlayer thickness by a factor of 4, and improves the bulk RI resolution by a factor of 22 based on the bulk RI change.

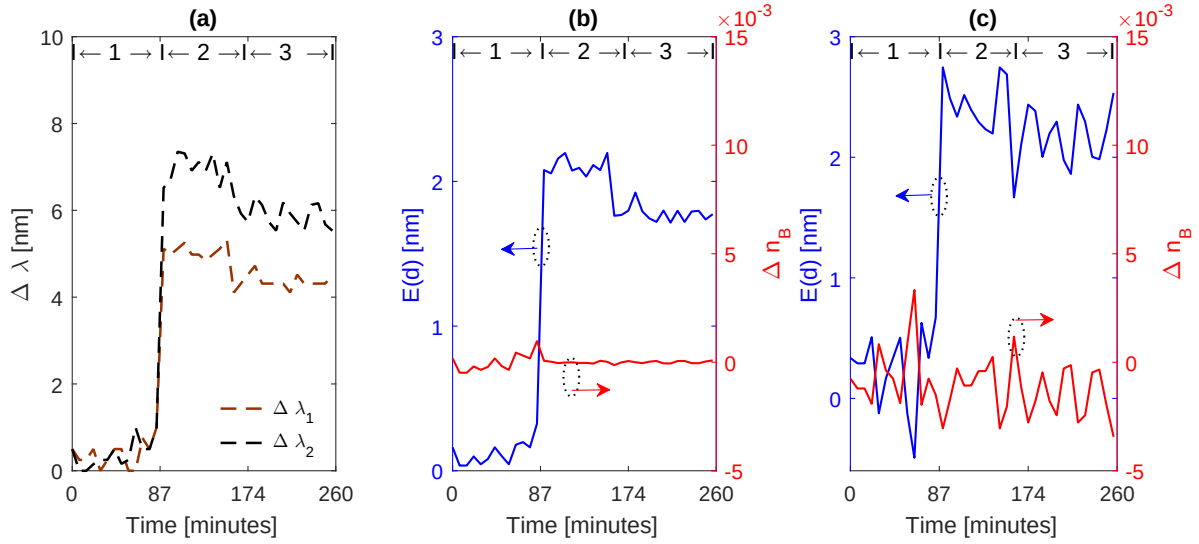

Figure 6–7: (a) shifts in the measured resonance wavelength employing the dip-finding method during streptavidin-bioten sensing experiments. (b) Estimated Adlayer thickness (left y-axis) and bulk RI change (right axis) based on the nonlinear–MLE method, (c) estimated adlayer thickness and bulk RI change based on the linear response model. The cycles on the graph represent the following: [1] Buffer, [2] Streptavidin solution, and [3] Buffer.

Now, the dynamic baseline centroid method is used to determine the resonance and generate the sensogram shown in Fig. 6–8 (a). This decreases the noise of the measured data and further improves the estimated results. The sensitivity factors are changed in accordance to the method used in determining the resonance location. The new sensor characteristics are also given in Table (6.2). In a similar manner, the resonance shifts are translated into a logarithmic scale, $ln(1-\Delta\lambda/\Delta\lambda_{max})$, which is used to estimate the adlayer and bulk RI change as shown in Fig. 6–8 (b)and Fig. 6–8 (c), respectively. As can be observed in the figure, the nonlinear–MLE method improved the limit of detection by a factor of ~ 5 and the bulk RI resolution by a factor of ~ 36 when compared to the linear response model results. Therefore, the nonlinear–MLE method can be used not only to improve the accuracy of the results, but also to improve the limit of detection and bulk RI resolution. Employing the dynamic baseline centroid method provided improved results for determining the resonance wavelengths, and applying the nonlinear–MLE method to these

results shows that the nonlinear–MLE method provided more accurate results compared to those based on the linear response model. The estimated values for the adlayer thickness and RI change based on the linear response model and the nonlinear–MLE method, considering both the dip-finding method and dynamic-baseline centroid method, are given in Table(6.3)

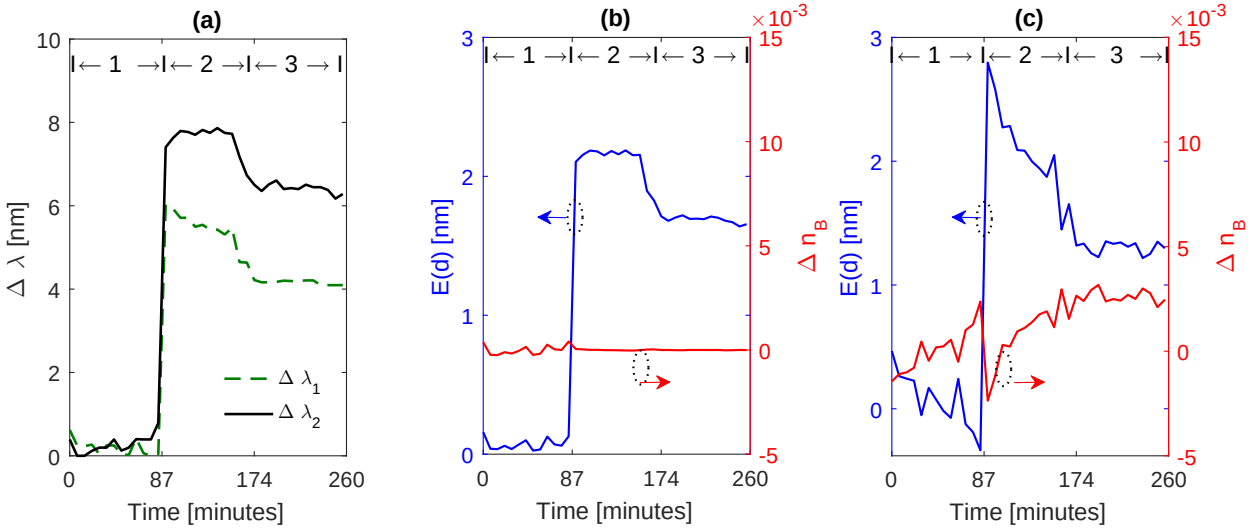

Figure 6–8: (a) Shifts in the resonance wavelengths ($\lambda_1 = 1100\,nm$, $\lambda_2 = 1450nm$), determined by the dynamic baseline centroid method. (b) Adlayer thickness (left y-axis) and bulk RI change (right y-axis) estimated by the nonlinear–MLE method. (c) Estimated adlayer thickness (left y-axis) and bulk RI change (right y-axis) based on the linear response model. The solutions were introduced to the nanocrescents in the following order: [1] Buffer, [2] Streptavidin solution, and [3] Buffer.

Table 6.3: Estimated adlayer thickness and bulk RI change based on the nonlinear–MLE method and the linear response model. The resonance wavelength shifts were determined by the dip-finding and dynamic baseline centroid methods.

		Adlayer thickness [nm]	Adlayer SD [nm]	Δn_B resolution [RIU]
Dip-finding	LM	2.16	0.24	1.3×10^{-3}
	Nonlinear–MLE	1.78	0.06	6×10^{-5}
Dynamic-baseline	LM	1.34	0.11	4.0×10^{-4}
	Nonlinear–MLE	1.69	0.023	1.1×10^{-5}

6.2 Summary

This chapter presented the nonlinear–MLE method. It is a statistical method, combining the MLE method with a nonlinear response model, to extract the adlayer thickness and bulk refractive index change with improved accuracy. The method not only provided a quantitative information about the binding events, but also improved the precision of LSPR sensors. The nonlinear response model is adopted because it represents the real scenario for the sensor response to adlayer thickness in typical sensing experiments, following a similar trend to that based on the association/dissociation constants [section 2.9]. The nonlinear response model used the EM decay length and sensitivity for each resonance to estimate the adlayer and bulk RI change, whilst the linear model used bulk and adlayer sensitivities that need to be recalculated or corrected for other target analytes. The latter represents a substantial disadvantage of the linear response model. In contrast to the linear response model, the nonlinear response model avoids the redundant calculation of the sensitivity to adlayer thickness for different analytes. Based on the simulated and measured results, the nonlinear–MLE method improved the bulk RI resolution by a factor of ~ 36 when compared to the linear response model (1.1×10^{-5} RIU vs 4×10^{-4} RIU), and achieved an improved limit of detection (based on the adlayer thickness) by a factor of ~ 5 when compared to that achieved by the linear response model (0.023 nm vs 0.11 nm uncertainty in the estimated adlayer thickness)

7

Conclusion

7.1 Summary

Plasmonic biosensors have attracted considerable attention in many applications, including medical diagnosis, drug discovery, and gas sensing. Due to growing demand for low cost and compact biosensors, metallic nanostructures have been of great interest. Apart from their miniaturized dimension, metallic nanostructures do not require complex instrumentation to excite the localized surface plasmon resonance. However, LSPR sensors yield broad extinction curves due to the short electromagnetic decay length, decreasing the signal to noise ratio. Therefore, techniques to improve SNR are needed. This thesis presented signal processing methods to improve the signal to noise ratio for LSPR sensors. The thesis also presented statistical methods to estimate quantitative information about binding events, distinguishing between the effects due to the adlayer thickness from those due to RI change

of the buffer.

The thesis employed the FDTD and FEM to model the nanostructures and validate the signal processing methods . The FDTD and FEM models provided accurate results when compared to the exact Mie solution for optical cross sections of metal nanoparticles. The FDTD method was employed for generating the reference matrix for the projection method as the computational cost is not affected with the number of frequency steps.

The thesis also provided results based on the fabricated nanostructures ranging from surface characterization (SEM and NSOM imaging) to the measured extinction curves as the fabricated structures were investigated for LSPR reproducibility based on repeating the measurement for multiple samples. The nanostructures displayed extinction curves with $\sim$2–5 % errors in the resonance wavelengths.

The projection method, introduced in chapter 4, increased the SNR of the nanotube structures by one order of magnitude, when compared to the conventional dip–finding method. It provided more accurate results, when compared against other advanced signal processing methods. Moreover, the projection method provided the best combination of LoD and SNR, as it exhibited the least error in the measured refractive index $\sim$ 14 % with a comparable SNR as that for the dynamic–baseline centroid method $\sim$ 32 dB. The latter incurred 33% error in the estimated refractive index, whilst the maximum error was associated with the fixed boundary centroid method $\sim$ 48%. Chapter 4 also provided a fitted Cauchy formula to estimate the refractive index for mixed solutions of known Cauchy parameters.

In chapter 5, the maximum likelihood estimation method was used alongside a linear response model to improve the accuracy and precision of self–referenced LSPR sensors. The linear response model assumes that the sensor response is a linear function of the bulk RI change and adlayer thickness. The linear–MLE method was validated based on the FEM results, and then applied to measured results associated with the fabricated multiple resonance nanorod structures. This included both bulk and surface binding experiments. The thesis provided a means to overcome the disadvantages of the linear response model in self–referenced sensing, including the requirement for repetitive numerical simulations in order to determine the sensitivity to adlayer thickness. This was achieved by using the measured bulk

RI sensitivity directly to correct for the adlayer sensitivity. Employing the three–resonance nanorod structures yielded three systems of linear response models, providing multiple estimates for the adlayer thickness and bulk RI change (3 values for each estimate). The MLE method was then applied to these values to improve the accuracy and accuracy of the results, The linear–MLE method improved the accuracy and precision by a factor of 3 ad 4 respectively. This can be further improved by optimizing the nanorods based on the cross sensitivity to bulk and adlayer thickness figure of merit.

The thesis finally presented an improved LSPR sensor for estimating adlayer thickness and bulk RI change based on the nonlinear response model and the MLE method. The fabricated nanocrescent structures were employed in the experiments. Compared to the established linear response model, the nonlinear–MLE method improved both the accuracy and precision of the results. Estimated adlayer thickness was achieved with a precision of 0.023 nm and 0.11 nm, based on the nonlinear–MLE method and the linear response model, respectively, indicating an improvement factor of ~ 5. The bulk RI resolution for the estimated bulk RI change was also improved by a factor of 36 based on the nonlinear–MLE method, as a change of 1.1×10^{-5} was detectable based on the nonlinear–MLE method, whilst the linear response model exhibited 4×10^{-4} RIU uncertainty. Therefore, careful adoption of signal processing techniques can significantly improve the performance of LSPR sensors.

7.2 Future work and potential improvements

The proposed methods provided improved resolution and limit of detection at least one order of magnitude based on noisy extinction/transmission spectra. This can be further improved according to the simulated results. The following recommendations would improve the experimental results based on the proposed signal processing methods

- Using a spectrometer with improved spectral resolution and photodiode array detector. This features a shorter acquisition time as compared to the Cary 5000 spectrometer, improving the temporal resolution in the real time measurements.

- The signal to noise ratio for the measured extinction spectra can be increased by averaging more scans. However, this will increase the acquisition time, which can be estimated as the number of averaged scans by the integration time of the detector. The integration time should also be kept below a threshold (the maximum integration time) over which the percentage noise reaches 50 % of the total detected signal.

- The optical path length is an important factor in determining the SNR. In this thesis, PDMS fluidic channels with 1 mm thickness were employed in the experiments. Although PDMS is transparent, impurities due to fabrication imperfections may disturb the optical path and cause scattering of the light beam. An improved system would use an acrylic chamber with decreased volume, hence decreased losses. As well, the depth of the microfluidic channels was 80 μm, which can be further reduced to decrease the losses and improve the SNR.

- The multiple resonance structures can be optimized for the figure of merit based on the cross sensitivity to bulk RI and adlayer thickness to improve the accuracy of the estimates. The nanocrescent structures exhibited a better cross sensitivity figure of merit than the nanorods. However, the nanocrescent structures should also be optimized for the operating wavelength range while maintaining an acceptable cross sensitivity figure of merit.

- Although LSPR sensors are less sensitive to temperature changes when compared to propagating SPR sensors, the refractive index of the sample changes with temperature, and a temperature controlled environment would provide improvement in the results. This is also important if the detector does not have a thermoelectric cooler as the noise increases with increased detector temperature. These improvements would increase the overall signal to noise ratio for the LSPR sensor and achieve an improved RI resolution.

- The methods based on the maximum likelihood estimation method, namely the linear–MLE and nonlinear–MLE methods, can be applied to simpler LSPR sensing systems, employing spectrometers of a narrow spectral range. Further improvement could be

achieved based on measuring the intensity change at a few fixed wavelengths by employing the integration response or normalized difference integration response (described in chapter 2), and then applying the linear–MLE method to improve the accuracy of the results.

- The linear response model, presented in chapter 5, is only valid for estimating thin adlayer thickness ($l_d/10$). Although this was improved by the nonlinear response model, presented in chapter 6, the maximum adlayer thickness that can be estimated by LSPR sensors is limited by the short EM decay length (l_d). For larger analytes, the same methods can be applied to other sensors of longer EM decay lengths.

Appendices

Appendix A

Derivation of the integral form of the binding kinetics

The binding of streptavidin of concentration $[A]$ with biotin of concentration $[B]$ can be represented by the following association-dissociation relationship [119]

$$[A] + [B] \underset{k_{off}}{\overset{k_{on}}{\rightleftharpoons}} [AB] \tag{A.1}$$

where $[AB]$ is the concentration of the compound. The affinity dissociation constant (K_D) can be used to determine the binding strength: it is related to the association (k_{on}) and dissociation (k_{off}) constants by

$$K_D \equiv \frac{k_{off}}{k_{on}} \tag{A.2}$$

The rate of compound formation is related to affinity constants by $\frac{\partial[AB]}{\partial t} = k_{on}[A][B] - k_{off}[AB]$, where $[A]$ is the initial molar concentration of streptavidin, $[A_0]$, $[AB]$ is the compound concentration that can be represented by the sensor response, $[AB] \propto R(t)$; and $[B]$ is the biotin concentration that can be represented by $[B] \propto R_{max} - R(t)$, where $R(t)$ is the sensor response with time. Consequently, the rate of compound formation can be determined by

$$\frac{dR(t)}{dt} = k_{on}[A_0](R_{max} - R(t)) - k_{off}R(t) \tag{A.3}$$

$$= k_{on}[A_0]R_{max} - R(t)(k_{on}[A_0] + k_{off}) \tag{A.4}$$

We can solve the differential equation by parts

$$u(t) = k_{on}[A_0]R_{max} - R(t)(k_{on}[A_0] + k_{off}) \tag{A.5}$$

$$\frac{du(t)}{dt} = -(k_{on}[A_0] + k_{off})\frac{dR(t)}{dt}$$

$$\frac{dR(t)}{dt} = -\frac{1}{(k_{on}[A_0] + k_{off})}\frac{du(t)}{dt} \tag{A.6}$$

Substituting Eqs. (A.5) and (A.6) in Eq.(A.4), we obtain

$$-\frac{1}{(k_{on}[A_0] + k_{off})}\frac{du(t)}{dt} = u(t)$$

Rearranging

$$\frac{du(t)}{du} = -(k_{on}[A_0] + k_{off})dt$$

$$\ln(u(t)) = -(k_{on}[A_0] + k_{off})t + K$$

where K is a constant

Taking the exponential to both sides

$$u(t) = Ke^{-(k_{on}[A_0]+k_{off})t} \tag{A.7}$$

substituting the value of u from Eq. (A.5), and $K = k_{on}[A_0]R_{max}$ in Eq. (A.7)

$$k_{on}[A_0]R_{max} - R(t)(k_{on}[A_0] + k_{off}) = k_{on}[A_0]R_{max}e^{-(k_{on}[A_0]+k_{off})t}$$

$$(k_{on}[A_0] + k_{off})R(t) = k_{on}[A_0]R_{max} - k_{on}[A_0]R_{max}e^{-(k_{on}[A_0]+k_{off})t} \tag{A.8}$$

Rearranging, the integral form of the kinetics equation is obtained

$$R(t) = \frac{k_{on}[A_0]R_{max}(1 - e^{-(k_{on}[A_0]+k_{off})t})}{k_{on}[A_0] + k_{off}} \tag{A.9}$$

Appendix B

Side-wall lithography fabrication method

The nanostructures presented in this thesis were fabricated by the side wall lithography technique, which is based on the nanoimprint lithography method [121]. A silicon mold is used to replicate nanopillars on a cyclic olefin copolymer by applying pressure and temperature according to Table (B.1). Other steps are then followed to create the final nanostructure, including metal coating and reactive ion etching (RIE). For the double nanotube structures, Pentacene was used as a spacing material as it is introduced by tilted dry coating (evaporation), and a second layer of gold was then coated. The top gold layer was removed by RIE.

Table B.1: Nanoimprint lithography fabrication recipe for imprinting a COP substrate using silicon mold

	Step 1	Step 2	Step 3	Step 4	Step 5
Pressure (MPa)	0	2	2	2	0
Lower temperature (C°)	150	150	150	100	70
Upper temperature (C°)	150	150	150	100	70
Time (sec)	10	60	600	150	30

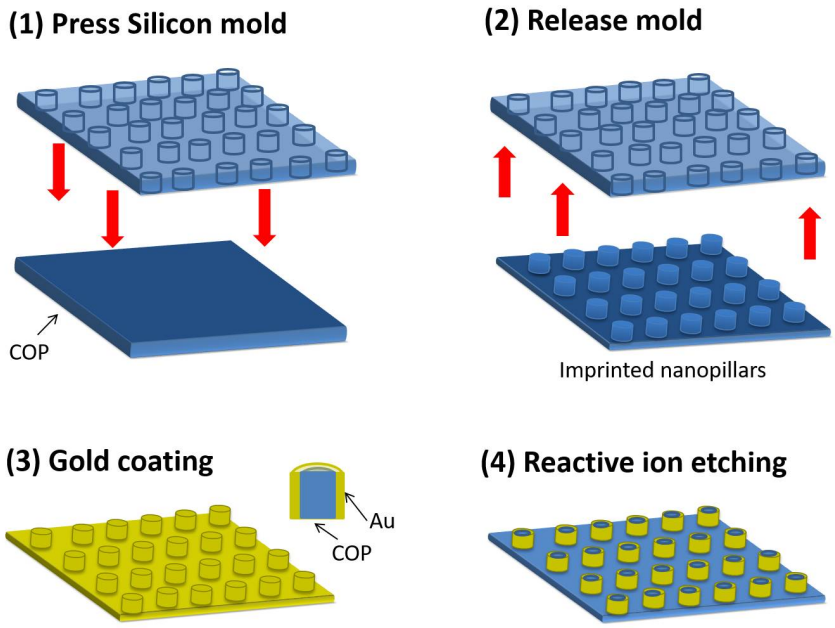

Figure B–1: Side-wall lithography fabrication method based on nanoimprinting COP polymer. An array of nanoholes (200 nm diameter, 20 nm-pitch) were already patterned on the silicon mold.

Appendix C

Fabrication of Nanocrescent structures

A silicon mold was used to imprint an array of polymer nanopillars based on the side-wall lithography, described in Appendix A. The nanopillars were then placed on a tilted stage (50 degree-tilt angle) and coated by gold evaporation in order to introduce a wedge angle to the wall thickness around the pillars. The thin part of the gold wall was removed by reactive ion etching (Argon) and the inner polymer pillars were then removed under a vertical oxygen plasma shower and nanocrescents were formed. Fig. C–1 illustrates this procedure.

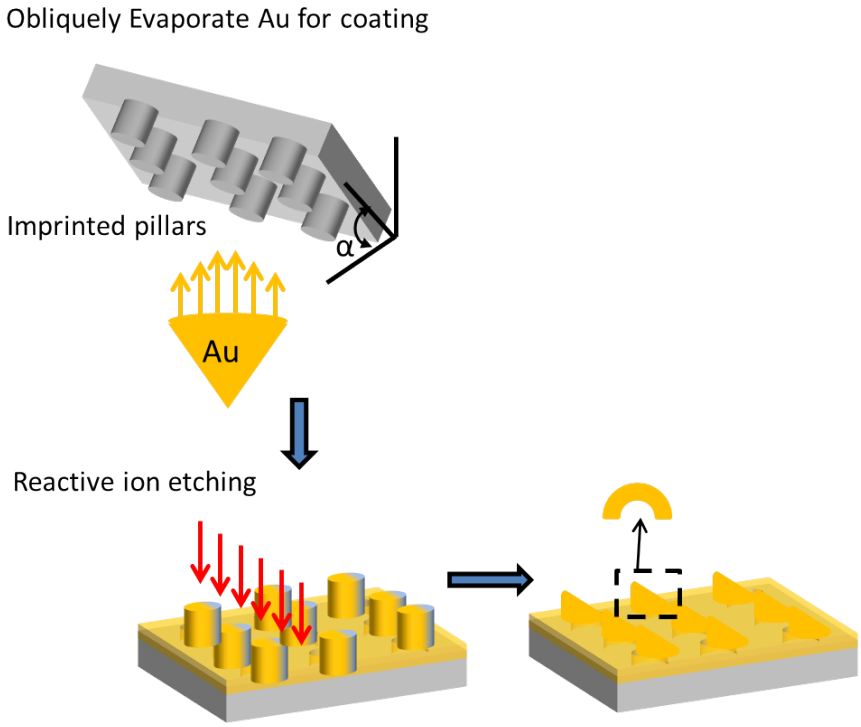

Figure C–1: Fabricating nanocrescent structures based on the side-wall lithography method.

Appendix D

Fluidic channel fabrication using PDMS-replica moulding

The hot embossing technique is a well established microfabrication method that has been widely used in fabricating polymer microfluidic channels. Here I outline the fabrication process of the fluidic channels employed in the sensing experiments: UV photolithography is used to pattern SU-8 negative resist on a silicon wafer, then immersed in the SU-8 developer, blown dry with Nitrogen gun, and postbaked to form the stamp that can be used to replicate the channels on PDMS as outlined in Fig. D–1. More details can be obtained from [127].

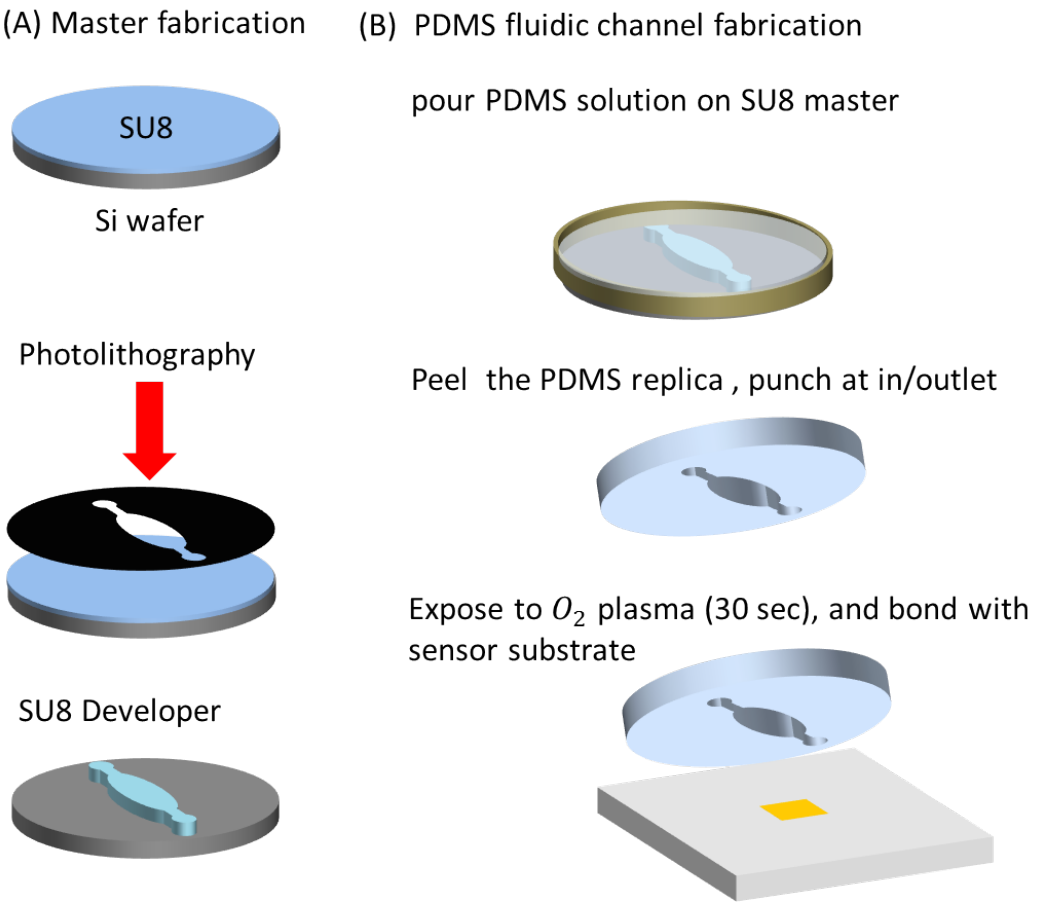

Figure D–1: Fabrication of fluidic channel based on the PDMs replica moulding method

References

[1] P. Mehrotra, "Biosensors and their applications – A review," Journal of Oral Biology and Craniofacial Research, **6**(2) 153–159 (2016).

[2] X. Fan et al., "Sensitive optical biosensors for unlabeled targets: A review," Analytica Chimica Acta, **620**(1/2) 8–26 (2008).

[3] X. Guo, "Surface plasmon resonance based biosensor technique: A review," J. Biophotonics, **5**(7), 483–501 (2012).

[4] Y. Chen and H. Ming, "Review of surface plasmon resonance and localized surface plasmon resonance sensor," Photonic Sens **2**(1) 37–49(2012).

[5] J. Caoa, T. Suna and K. T.V. Grattana, "Gold nanorod-based localized surface plasmon resonance biosensors: A review," Sensors and Actuators B: Chemical, **195**, 332-351 (2014).

[6] A. J. Haes and R. P. Van Duyne, "A unified view of propagating and localized surface plasmon resonance biosensors," Anal. Bioanal. Chem., **379**(7/8), 920–930 (2004).

[7] J. M. Brockman, B. P. Nelson, R. M. Corn, "Surface plasmon resonance imaging measurements of ultrathin organic films," Annu Rev Phys Chem **51** 41–63 (2000).

[8] J. S. Shumaker-Parry , M. H. Zareie, R Aebersold , CT Campbell, "Microspotting streptavidin and double-stranded DNA arrays on gold for high-throughput studies of

protein-DNA interactions by surface plasmon resonance microscopy," Anal Chem **76**, 918–929 (2004).

[9] A. D. McFarland, R. P. Van Duyne, "Single Silver Nanoparticles as Real-Time Optical Sensors with Zeptomole Sensitivity," Nano Lett **3**, 1057–1062 (2003).

[10] J. J. Mock, D. R. Smith, S Schultz, "Local Refractive Index Dependence of Plasmon Resonance Spectra from Individual Nanoparticles," Nano Lett **3**, 485–491 (2003).

[11] M. Couture, S. S. Zhao , J. F. Masson, "Modern surface plasmon resonance for bioanalytics and biophysics," Phys Chem Chem Phys., **15**(27), 11190–11216 (2013).

[12] A. V. Kabashin , P. Evans, S. Pastkovsky, W. Hendren, G. A. Wurtz , R. Atkinson, R. Pollard, V. A. Podolskiy and A. V. Zayats, "Plasmonic nanorod metamaterials for biosensing," Nature Materials, **8**, 867–871 (2009).

[13] J. Langer, S. M. Novikov, L. M. Liz-Marzan, "Sensing Using Plasmonic Nanostructures and Nanoparticles," Nanotechnology, **26**(32), 322001 (2015).

[14] S. S. Aćimović, M. A. Ortega, V. Sanz, J. Berthelot, J. L. Garcia-Cordero, J. Renger, S. J. Maerkl, M. P. Kreuzer, and R. Quidant, "LSPR Chip for Parallel, Rapid, and Sensitive Detection of Cancer Markers in Serum," Nano Letters, **14**(5), 2636–2641 (2014).

[15] J. L. Hammond, N. Bhalla, S. D. Rafiee, and P. Estrela, "Localized Surface Plasmon Resonance as a Biosensing Platform for Developing Countries," Biosensors **4**(2), 172–188 (2014).

[16] N. Nath and A. Chilkoti, "Label-free biosensing by surface plasmon resonance of nanoparticles on glass: optimization of nanoparticle size," Anal. Chem., **76**(18), 5370–5378 (2004).

[17] A. J. Haes, S. Zou, G. C. Schatz, and R. P. Van Duyne, "Nanoscale optical biosensor: short range distance dependence of the localized surface plasmon resonance of noble metal nanoparticles," J. Phys. Chem. B, **108**(22), 6961–6968 (2004).

[18] J. J. Mock, M. Barbic, D. R. Smith, D. A. Schultz, and S. Schultz, "Shape effects in plasmon resonance of individual colloidal silver nanoparticles," J. Chem. Phys., **116**(15), 6755–6759 (2002).

[19] A. L. Schmucker, N. Harris, M. J. Banholzer, M. G. Blaber, K. D. Osberg, G. C. Schatz, and C. A. Mirkin, "Correlating nanorod structure with experimentally measured and theoretically predicted surface plasmon resonance," ACS Nano, **4**, 5453–5463 (2010).

[20] H. Chen, X. Kou, Z. Yang, W. Ni, and J. Wang, "Shape- and size dependent refractive index sensitivity of gold nanoparticles," Langmuir, **24**, 5233–5237 (2008).

[21] E. Stefan Kooij and B. Poelsema, "Shape and size effects in the optical properties of metallic nanorods, Phys. Chem. Phys. **8**(28), 3349–3357 (2006).

[22] D. P. Lyvers, J.-M. Moon, A. V. Kildishev, V. M. Shalaev, and A. Wei, "Gold nanorod arrays as plasmonic cavity resonators," ACS Nano, **2**, 2569–2576 (2008).

[23] K. M. Mayer, S. Lee, H. Liao, B. C. Rostro, A. Fuentes, P. T. Scully, C. L. Nehl, and J. H. Hafner, "A label–free immunoassay based upon localized surface plasmon resonance of gold nanorods," ACS Nano, **2**, 687–692 (2008).

[24] S. R. Beeram and F. P. Zamborini, "Purification of gold nanoplates grown directly on surfaces for enhanced localized surface plasmon resonance biosensing," ACS Nano, **4**, 3633–3646 (2010).

[25] Y. Sonnefraud, N. Verellen, H. Sobhani, G. Vandenbosch, V. Moshchalkov, P. Van Dorpe, P. Nordlander, and S. Maier, "Experimental realization of subradiant, superradiant, and Fano resonances in ring/disk plasmonic nanocavities," ACS Nano **4**, 1664–1670 (2010).

[26] Y. Sun and Y. Xia, "Increased sensitivity of surface plasmon resonance of gold nanoshells compared to that of gold solid colloids in response to environmental changes," Anal. Chem. **74**, 5297–5305 (2002).

[27] E. Prodan, A. Lee, and P. Nordlander, "The effect of a dielectric core and embedding medium on the polarizability of metallic nanoshells," Chem. Phys. Lett. **360**, 325–332 (2002).

[28] H. Wang, D. W. Brandl, F. Le, P. Nordlander, and N. J. Halas, "Nanorice: a hybrid plasmonic nanostructure," Nano Lett. **6**, 827832 (2006).

[29] S. Lal , S. Link. and N. J. Halas, "Nano-optics from sensing to waveguiding," Nature Photonics **1**, 641–648 (2007).

[30] H. Wang, D. W. Brandl, P. Nordlander, and N. J. Halas, "Plasmonic nanostructures: artificial molecules," Acc. Chem. Res., **40**, 53-62 (2007).

[31] A. K. Sharma, R. Jha and B. D. Gupta, "Fiber-Optic Sensors Based on Surface Plasmon Resonance: A Comprehensive Review," IEEE Sensors Journal, **7** (8), 1118–1129 (2007).

[32] K. H. Yoon, M. L. Shuler, and S. J. Kim "Design optimization of nano-grating surface plasmon resonance sensors," Optics Express, **14**(11), 4842–4849 (2006)

[33] P. B Luppa, J. Metzger, H. Schneider, "surface plasmon resonance biosensors in urine proteomics," Methods Mol Biol., **641**, 193–221 (2010).

[34] E. Kretschmann and H. Raether, "Radiative Decay of Non-Radiative Surface Plasmons Excited by Light," Zeitschrift Für Naturforschung, **23**(12), 2135–2136 (1968).

[35] A. Otto, "Excitation of Surface Plasma Waves in Silver by the Method of Frustrated Total Reflection," Zeitschrift Für Physik a Hadrons and Nuclei, **216**(4), 398–410 (1968).

[36] S. Roh, T. Chung and B. Lee, "Overview of the Characteristics of Micro- and Nano-Structured Surface Plasmon Resonance Sensors," Sensors, **11**(2), 1565–1588 (2011).

[37] M. Piliarik, H. Vaisocherova, J. Homola, "Surface plasmon resonance biosensing," Methods Mol. Biol., **503**, 65–88 (2009).

[38] C. F. Bohren, D. R. Huffman, "Absorption and scattering of Light by small particles," Wiley, New York, 1983.

[39] J. A. Osborn, "Demagnetizing Factors of the General Ellipsoid," Phys. Rev., **67** (11/12), 351–357 (1945).

[40] S. Link, M. B. Mohamed, M. A. El-Sayed, "Simulation of the optical absorption spectra of gold nanorods as a function of their aspect ratio and the effect of the medium dielectric constant," J Phys Chem B, **103**(16):3073-3077 (1999).

[41] E. S. Kooij, B. Poelsema, "Shape and size effects in the optical properties of metallic nanorods," Phys Chem Chem Phys, **8**, 3349-3357 (2006).

[42] C. Sönnichsen, "Plasmons in metal nanostructures," PhD thesis, Fakultät für Physik der Ludwig-Maximilians-Universität München (2001).

[43] U. Kreibig, M. Vollmer, "Optical Properties of Metal Clusters," Springer, Berlin (1995).

[44] C. L. Nehl, N. K. Grady, G. P. G. Goodrich, F. Tam, N. J. Halas and J. H. Hafner, "Scattering spectra of single gold nanoshells," Nano Lett. **4**, 2355 (2004).

[45] S. Link and M. A. El-Sayed, "Spectral Properties and Relaxation Dynamics of Surface Plasmon Electronic Oscillations in Gold and Silver Nanodots and Nanorods," J. Phys. Chem. B, **103**(40), 8410–8426 (1999).

[46] C. Novo, A. M. Funston, A. K. Gooding, P. Mulvaney, "Electrochemical charging of single gold nanorods," J. Am. Chem. Soc. **131**(41), 14664-14666 (2009).

[47] A. M. Brown, M. T. Sheldon, and H. A. Atwater, "Electrochemical Tuning of the Dielectric Function of Au Nanoparticles," ACS Photonics, **2**(4), 459–464 (2015).

[48] P.B. Johnson and R.W. Christy, "Optical Constants of the Noble Metals," Physical Review B, **6**(12), 4370–4379 (1972).

[49] V. Giannini, A. I. Fernández-Domínguez, S. C. Heck, and S. A. Maier, "Plasmonic Nanoantennas: Fundamentals and Their Use in Controlling the Radiative Properties of Nanoemitters," Chemical Reviews, **111**(6), 3888–3912 (2011).

[50] A. Vial, A. S. Grimault, D. Barchiesi and M. L. de la Chapelle, "Improved Analytical Fit of Gold Dispersion: Application to the Modeling of Extinction Spectra with a Finite-Difference Time-Domain Method, Physical Review B, **71**(8), 85416–85423 (2005).

[51] A. Rakić, A. Djurišić, J. Elazar, and M. Majewski, "Improved Analytical Fit of Gold Dispersion: Application to the Modeling of Extinction Spectra with a Finite-Difference Time-Domain Method, Appl. Opt. **37**, 5271 (1998).

[52] G. Mie, "Beitrăge zur Optik trűber Medien, speziell kolloidaler Metall ősungen," Annalen der Physik, **330**(3):377–445 (1908).

[53] P. K. Jain and M. A. El-Sayed, "Noble Metal Nanoparticle Pairs: Effect of Medium for Enhanced Nanosensing," Nano Lett., 2008, **8**(12), 4347–4352.

[54] J. Parsons, C.P. Burrows, J. R. Sambles, and W. L. Barnes, "A comparison of techniques used to simulate the scattering of electromagnetic radiation by metallic nanostructure," Journal of modern optics, **57** (5), 356–365 (2010).

[55] E. M. Purcell, C. R. Pennypacker, "Scattering and absorption of light by nonspherical dielectric grains," Astrophys J, **186**, 705–14 (1973).

[56] M. A. Yurkin, V. P. Maltsev, A. G. Hoekstra, "The discrete dipole approximation for simulation of light scattering by particles much larger than the wavelength," J Quant Spectrosc Radiat Transfer, **106**, 546-557 (2007).

[57] M. A. Yurkin, A. G. Hoekstra, "The discrete-dipole-approximation code ADDA: Capabilities and known limitations," Journal of Quantitative Spectroscopy and Radiative Transfer," **112**(13), 2234–2247 (2011).

[58] DDSCAT 7.1, http://www.astro.princeton.edu/ draine/DDSCAT.html

[59] M. A. Morgan, K. K. Mei "Finite-element computation of scattering by inhomogeneous penetrable bodies of revolution," IEEE Trans Ant. Propag., **27**(2), 202–14 (1979).

[60] S. K. Yee, "Numerical solution of initial boundary value problems involving Maxwells equations in isotropic media," IEEE Trans Antennas Propag., **14**(3), 302–307 (1966).

[61] OptiFDTD-Designer, version 12.0.0.618, optiwave, http://www.optiwave.com

[62] C. Hafner, "The generalized multipole technique for computational electromagnetics. Boston: Artech House, (1991).

[63] P. Waterman, "Matrix formulation of electromagnetic scattering," Proc. IEEE, **53**(8), 805–812 (1965).

[64] B. Peterson and S. Ström, "T Matrix for Electromagnetic Scattering from an Arbitrary Number of Scatterers and Representations of E(3)," Phys. Rev. D, **8**, 3661 (1973).

[65] M. I. Mishchenko., "Light scattering by randomly oriented axially symmetric particles," JOSA A, **8** (6), 871–882 (1991).

[66] COMSOL Multiphysics, v5.2, http://www.comsol.com/

[67] J. Wang, S.V. Boriskina, H. Wang, and B.M. Reinhard, "Illuminating epidermal growth factor receptor densities on filopodia through plasmon coupling," ACS Nano, **5**(8), 6619–6628 (2011).

[68] M. Liu, J. Chao, S. Deng, K. Wang, K. Li, and C. Fan, "Dark-field microscopy in imaging of plasmon resonant nanoparticles," Colloids and Surfaces B: Biointerfaces, **124**(1), 111–117 (2014).

[69] P. Kvasnička, and J. Homola, "Optical sensors based on spectroscopy of localized surface plasmons on metallic nanoparticles: Sensitivity considerations," Biointerphases, **3**(3): FD4–FD11 (2008).

[70] A. Jakab, C. Rosman, Y. Khalavka, J. Becker, A. Trügler, U. Hohenester, and C. Sönnichsen, "Highly Sensitive Plasmonic Silver Nanorods," ACS Nano, **5**(9), 6880–6885 (2011).

[71] M. Piliarik and J. Homola, "Surface plasmon resonance (SPR) sensors: approaching their limits?," Opt. Express **17**, 16505 (2009).

[72] L. J. Sherry, "Localized Surface Plasmon Resonance Spectroscopy of Single Silver Nanocubes," Nano Letters, **5**(10):2034–2038 (2005).

[73] J. Homola, "Surface Plasmon Resonance Sensors for Detection of Chemical and Biological Species," Chem. Rev.,**108**(2), 462–493 (2008).

[74] M. Faraday, "The Bakerian Lecture: Experimental Relations of Gold (and Other Metals) to Light," Philosophical Transactions of the Royal Society of London, **147**, 145–181 (1857).

[75] P. Englebienne, "Use of colloidal gold surface plasmon resonance peak shift to infer affinity constants from the interactions between protein antigens and antibodies specific for single or multiple epitopes," Analyst, **123**(7):1599–1603 (1998).

[76] N. R. Jana, L. Gearheart, and C. J. Murphy, "Seed-Mediated Growth Approach for Shape Controlled Synthesis of Spheroidal and Rod-like Gold Nanoparticles Using a Surfactant Template," Adv. Mater, **13**(18),1389–1393 (2001).

[77] B. Nikoobakht and and M. A. El-Sayed, "Preparation and Growth Mechanism of Gold Nanorods (NRs) Using Seed-Mediated Growth Method," Chemistry of Materials, **15**(10), 1957–1962 (2003).

[78] X. Huang, S. Neretina, M. A. El-Sayed, "Gold Nanorods: From Synthesis and Properties to Biological and Biomedical Applications," Adv. Mater., **21**(48), 4880–4910 (2009).

[79] D. K. Smith, B. A. Korgel, "The Importance of the CTAB Surfactant on the Colloidal Seed-Mediated Synthesis of Gold Nanorods," Langmuir, **24**(3), 644-649 (2008).

[80] R. G. Rayavarapu, C. Ungureanu, P. Krystek, T. G. van Leeuwen, S. Manohar, "Iodide Impurities in Hexadecyltrimethylammonium Bromide (CTAB) Products: LotLot Variations and Influence on Gold Nanorod Synthesis," Langmuir , **26**(7), 5050-5055 (2010).

[81] W. Niu, L. Zhang, G. Xu, "Seed-Mediated Growth of Noble Metal Nanocrystals: Crystal Growth and Shape Control," Nanoscale, **5**, 3172-3181 (2013).

[82] L. Scarabelli,A. Sanchez-Iglesias, J. Perez-Juste, L. M. Liz-Marzan, "A Tips and Tricks Practical Guide to the Synthesis of Gold Nanorods," J. Phys. Chem. Lett., **6**(21), 4270-4279 (2015).

[83] T. W. Ebbesen, H. J. Lezec, H. F. Ghaemi, T. Thio and P. A. Wolff, "Extraordinary optical transmission through sub-wavelength hole arrays," Nature **391**, 667669 (1998).

[84] T. D. Visser, "Plasmonics: Surface plasmons at work?," Nature Physics **2**, 509 – 510 (2006).

[85] C. Genet and T. W. Ebbesen, "Light in tiny holes," Nature **445**, 39–46 (2007).

[86] M. Schwind,B. Kasemo, and I. Zori, "Localized and Propagating Plasmons in Metal Films with Nanoholes," Nano Letters, **13**(4), 1743–1750 (2013).

[87] S. F. Romanuik, S. M. Grist, B. L. Gray, D. Hohertz, K. L. Kavanagh, N. Gulzar, J. K. Scott, R. Nirwan, C. Hui, A., G. Brolo, and R. Gordon, "Detecting Antibodies Secreted by Trapped Cells Using Extraordinary Optical Transmission," IEEE SENSORS JOURNAL, **11**(11) (2011).

[88] M. Das, D. Hohertz, R. Nirwan, A. G. Brolo, K. L. Kavanagh, R. Gordon, "Improved Performance of Nanohole Surface Plasmon Resonance Sensors by the Integrated Response Method," Photonics Journal, IEEE **3**(3), 441–449 (2011).

[89] A. A. Yanik, M. Huang, A. Artar, T. Y. Chang and H. Altug, "Novel plasmonic biosensors molding the flow of light and fluidics at subdiffraction limit," IEEE Photonics Society Annual Meeting Proceedings, 162–163, Denver CO (2010).

[90] J. Dostlek, H. Vaisocherov, J. Homola, "Multichannel surface plasmon resonance biosensor with wavelength division multiplexing," Sensors and Actuators B: Chemical, **108**(1/2)1-2, 758–764 (2005).

[91] C. Yu and J. Irudayraj, "Multiplex biosensor using gold nanorods," Anal. Chem., **79**(2), 572–579 (2007).

[92] C Yu and J. Irudayaraj, "Quantatatve Evaluation of sensitivity and selectivity of multiplex NanoSPR biosensor assays," Biophysical journal, **93**(10), 3684–3692 (2007).

[93] Y. Wang and L. Tang, "Multiplexed gold nanorod array biochip for multi-sample analysis Biosensors and Bioelectronics,**67**, 18–24 (2015).

[94] S. K. Dondapati, T. K. Sau, C. Hrelescu, T. A. Klar, F. D. Stefani, and J. Feldmann, "Label-free Biosensing Based on Single Gold Nanostars as Plasmonic Transducers," ACS Nano **4**(11), 6318–6322 (2010).

[95] S–W. Lee, K–S. Lee, J. Ahn, J. J. Lee, M–G. Kim, and Y–B. Shin, "Highly Sensitive Biosensing Using Arrays of Plasmonic Au Nanodisks Realized by Nanoimprint Lithography," ACS Nano **5**(2), 897–904 (2011).

[96] W. J. Galush, S. A. Shelby, M. J. Mulvihill, A. Tao, P. Yang, and J. T. Groves, "A Nanocube Plasmonic Sensor for Molecular Binding on Membrane Surfaces," Nano Letters, **9**(5), 2077–2082 (2009).

[97] D. Aherne, D. E. Charles , M. E. Brennan-Fournet , JM Kelly , YK Gun /'ko, "Etching-resistant silver nanoprisms by epitaxial deposition of a protecting layer of gold at the edges," Langmuir **25**(17):10165-73 (2009).

[98] E.M. Larsson, J. Alegret, M. Kall, D.S. Sutherland, "Sensing Characteristics of NIR Localized Surface Plasmon Resonances in Gold Nanorings for Application as Ultrasensitive Biosensors," Nano Letters **7**(5), 1256–1263 (2007).

[99] K. Johansen, R. Stalberg, I. Lundstrom, and B. Liedberg, "Surface plasmon resonance: instrumental resolution using photodiode arrays," Meas. Sci. Technol. **11**(11), 1630-1638 (2000).

[100] R. E. Messersmith, G. J. Nusz, and S. M. Reed, "Using the Localized Surface Plasmon Resonance of Gold Nanoparticles to Monitor Lipid Membrane Assembly and Protein Binding," J. Phys. Chem. C Nanomater Interfaces **117**(50), 26725-26733 (2013).

[101] G. G. Nenninger, M. Piliarik and J. Homola, "Data analysis for optical sensors based on spectroscopy of surface plasmons," Meas. Sci. Technol. **13**(12),2038–2046 (2002).

[102] K. S. Johnston, K. S. Booksh, T. M. Chinowsky, and S. S. Yee, "Performance comparison between high and low resolution spectrophotometers used in a white light surface plasmon resonance sensor," Sens. Actuators B, Chem., **54**(1/2), 80–88 (1999).

[103] T. M. Chinowsky, L. S. Jung, and S. S. Yee, "Optimal linear data analysis for surface plasmon resonance biosensors," Sens. Actuators B, Chem. **54**(1/2), 89–97 (1999).

[104] E. Stenberg, B. Persson, H. Roos, and C. Urbaniczky, "Quantitative determination of surface concentration of protein with surface plasmon resonance using radiolabeled proteins," J. Colloid Interface Sci. **143**(2), 513–526 (1991).

[105] A. Barnett, and E. M. Goldys, "Modeling of the SPR resolution enhancement for conventional and nanoparticle inclusive sensors by using statistical hypothesis testing," Opt. Express **18**(9), 9384–9397 (2010).

[106] C. J. Alleyne, A. G. Kirk, W-Y. Chien, and P. G. Charette, "Numerical method for high accuracy index of refraction estimation for spectro-angular surface plasmon resonance systems," Opt. Express **16**(24), 19493–19503 (2008).

[107] M. E. Stewart , J. Tao , J. Maria , S. K. Gray and J. A. Rogers, "Multispectral thin film biosensing and quantitative imaging using 3D plasmonic crystals," Anal. Chem. **81**(15), 5980–5989 (2009).

[108] S. Zhan, X. Wang and Y. Liu, "Fast centroid algorithm for determining the surface plasmon resonance angle using the fixed-boundary method," Measurement Science and Technology **22**(2), 025201 (2011).

[109] G. G. Nenninger, J. B. Clendenning, C. E. Furlong, and S. S. Yee, "Reference-compensated biosensing using a dual-channel surface plasmon resonance sensor system based on a planar lightpipe configuration," Sens. Actuators B Chem., **51**(1/3), 38–45 (1998).

[110] P. Schuck, and H. Zhao, "The Role of Mass Transport Limitation and Surface Heterogeneity in the Biophysical Characterization of Macromolecular Binding Processes by SPR Biosensing," Methods in molecular biology, **627**,15 (2010).

[111] D. G. Drescher, N. A. Ramakrishnan, and M. J. Drescher, "Surface Plasmon Resonance (SPR) Analysis of Binding Interactions of Proteins in Inner-Ear Sensory Epithelia," Methods in Molecular Biology, **493**, 323 (2009).

[112] S. Nizamov and V. M. Mirsky, "Self-referencing SPR-biosensors based on penetration difference of evanescent waves," Biosens. Bioelectron. **28**(1), 263–269 (2011).

[113] J. Homola, H. B. Lu, and S. S. Yee, "Dual-channel surface plasmon resonance sensor with spectral discrimination of sensing channels using dielectric overlayer," Electronics Letters, **35**(13), 1105 (1999).

[114] R. Slavik, J. Homola, and H. Vaisocherová, "Advanced biosensing using simultaneous excitation of short and long range surface plasmons," Measurement Science and Technology, **17**(4):932–939 (2006).

[115] J. T. Hastings,J. Guo, P. D. Keathley, P. B. Kumaresh, Y. Wei, S. Law, and L. G. Bachas, "Optimal self-referenced sensing using long- andshort- range surface plasmons," Opt. Express,**15**(26), 17661 (2007).

[116] N. Nehru, E. U. Donev, G. M. Huda, L. Yu, Y. Wei, and J. T. Hastings, "Differentiating surface and bulk interactions using localized surface plasmon resonances of gold nanorods," Opt. Express, **20**, 6905 (2012).

[117] N. Nehru, Y. Linliang, W. Yinan, J. T. Hastings, "Using U-Shaped Localized Surface Plasmon Resonance Sensors to Compensate for Nonspecific Interactions," IEEE Trans. Nanotechnology, **13**(1), 55–61 (2014).

[118] F. Bahrami, M. Maisonneuve, M. Meunier, J. S. Aitchison, and M. Mojahedi, "Self-referenced spectroscopy using plasmon waveguide resonance biosensor," Biomed. Opt. Express **5**, 2481 (2014).

[119] R. W. Glaser, "Antigen-antibody binding and mass transport by convection and diffusion to a surface: a two-dimensional computer model of binding and dissociation kinetics," Analytical Biochemistry, **213**(1), 152–161 (1993).

[120] https: //www.biacore.com

[121] W. Kubo and S. Fujikawa, "Au Double Nanopillars with Nanogap for Plasmonic Sensor," Nano Letters **11**(1), 8–15 (2011).

[122] S. Prauzner-Bechcicki, J. Wiltowska-Zubera, A. Budkowski, M. Lekka and J. Rysz, "Implementation of NSOM to Biological Samples," J. Acta Phys. Polym., A**121**, 533539 (2012).

[123] A. Abumazwed, A. G. Kirk, W. Kubo, T. Tanaka, "Numerical and experimental investigation of plasmonic properties of silver nanocrescent structures for sensing applications," Proc. SPIE 9371, Photonic and Phononic Properties of Engineered Nanostructures, V 937127 (27 February 2015).

[124] M. Hu, C. Novo, A. Funston, H. Wang, H. Staleva, S. Zou, P. Mulvaney, Y. Xia and G. Hartland, "Dark-field microscopy studies of single metal nanoparticles: understanding the factors that influence the linewidth of the localized surface plasmon resonance," J. Mater. Chem., **18**, 1949 (2008).

[125] M. W. Knight and N. J. Halas, "Nanoshells to nanoeggs to nanocups: optical properties of reduced symmetry core–shell nanoparticles beyond the quasistatic limit," New J. Phys., **10**, 105006 (2008).

[126] P. K. Jain , K. S. Lee, I. H. El-Sayed, M. A. El-Sayed, "Calculated absorption and scattering properties of gold nanoparticles of different size, shape, and composition: applications in biological imaging and biomedicine," J Phys Chem B. **110**(14):7238–48 (2006).

[127] G. M. Whitesides, E. Ostuni, S. Takayama, X. Y. Jiang, and D. E. Ingber, "Soft lithography in biology and biochemistry," Ann. Rev.Biomed. Eng. **3**, 335–373 (2001).

[128] D. R. Lide, 86th Handbook of Chemistry and Physics, (CRC Press, Boca Raton 2006) Chap. 8.

[129] S. Kedenburg, M. Vieweg, T. Gissibl, and H. Giessen, "Linear refractive index and absorption measurements of nonlinear optical liquids in the visible and near-infrared spectral region," Opt. Mater. Express **2**(11), 1588–1611 (2012).

[130] E. Fujiwara, R. T. Takeishi, A. Hase, E. Ono, J. S. Santos and C. K. Susuki, "Real-time optical fibre sensor for hydro-alcoholic solutions," Measurement Science and Technology **21**(9), 1–5 (2010).

[131] Nowakowska, Janina, The Refractive Indices of Ethyl Alcohol and Water Mixtures, Master's Theses (Loyola University Chicago 1939), Paper 668.

[132] J. M. Bingham, J. N. Anker, L. E. Kreno, and R. P. Van Duyne, "Gas Sensing with High-Resolution Localized Surface Plasmon Resonance Spectroscopy," Journal of the American Chemical Society **132**(49), 17358–17359 (2010).

[133] Y. Shen, J. Zhou, T. Liu, Y. Tao, R. Jiang, M. Liu, G. Xiao, J. Zhu, Z-K. Zhou, X. Wang, C. Jin and J. Wang, "Plasmonic gold mushroom arrays with refractive index sensing figures of merit approaching the theoretical limit,"Nat Commun. 4, 2381-2389 (2013).

[134] A. Abumazwed, W. Kubo, C. Shen, T. Tanaka, and A. G. Kirk, "Projection method for improving signal to noise ratio of localized surface plasmon resonance biosensors," Biomed. Opt. Express 8, 446 (2016).

[135] L. L. Scharf, Statistical Signal Processing: Detection, Estimation, and Time Series Analysis (Addison-Wesley, 1991).

[136] L. S. Jung , C. T. Campbell , T. M. Chinowsky , M. N. Mar , and S. S. Yee, "Quantitative Interpretation of the Response of Surface Plasmon Resonance Sensors to Adsorbed Films," Langmuir, **14**(19), 5636 (1998).

[137] A. J. Haes, R. P. Van Duyne, "A nanoscale optical biosensor: sensitivity and selectivity of an approach based on the localized surface plasmon resonance spectroscopy of triangular silver nanoparticles," J Am Chem Soc. **124**(35), 10596-10604 (2002).

[138] CAD/Art Services, Inc, www.outputcity.com

[139] Scientific, T., EZ-Link HPDP-Biotin Instructions.

[140] ProteoChem, www.proteochem.com

[141] L. Tian, E. Chen, N. Gandra, A. Abbas, and S. Singamaneni, "Gold Nanorods as Plasmonic Nanotransducers: Distance-Dependent Refractive Index Sensitivity," Langmuir, **28**(50), 17435 (2012).

[142] D. Bindel and J. Goodman, "Principles of scientific computing," manuscript (2009).

[143] H. Chen, X. Kou, Z. Yang, W. Ni, and J. Wang, "Shape- and size-dependent refractive index sensitivity of gold nanoparticles," Langmuir **24**(10), 5233–5237 (2008).